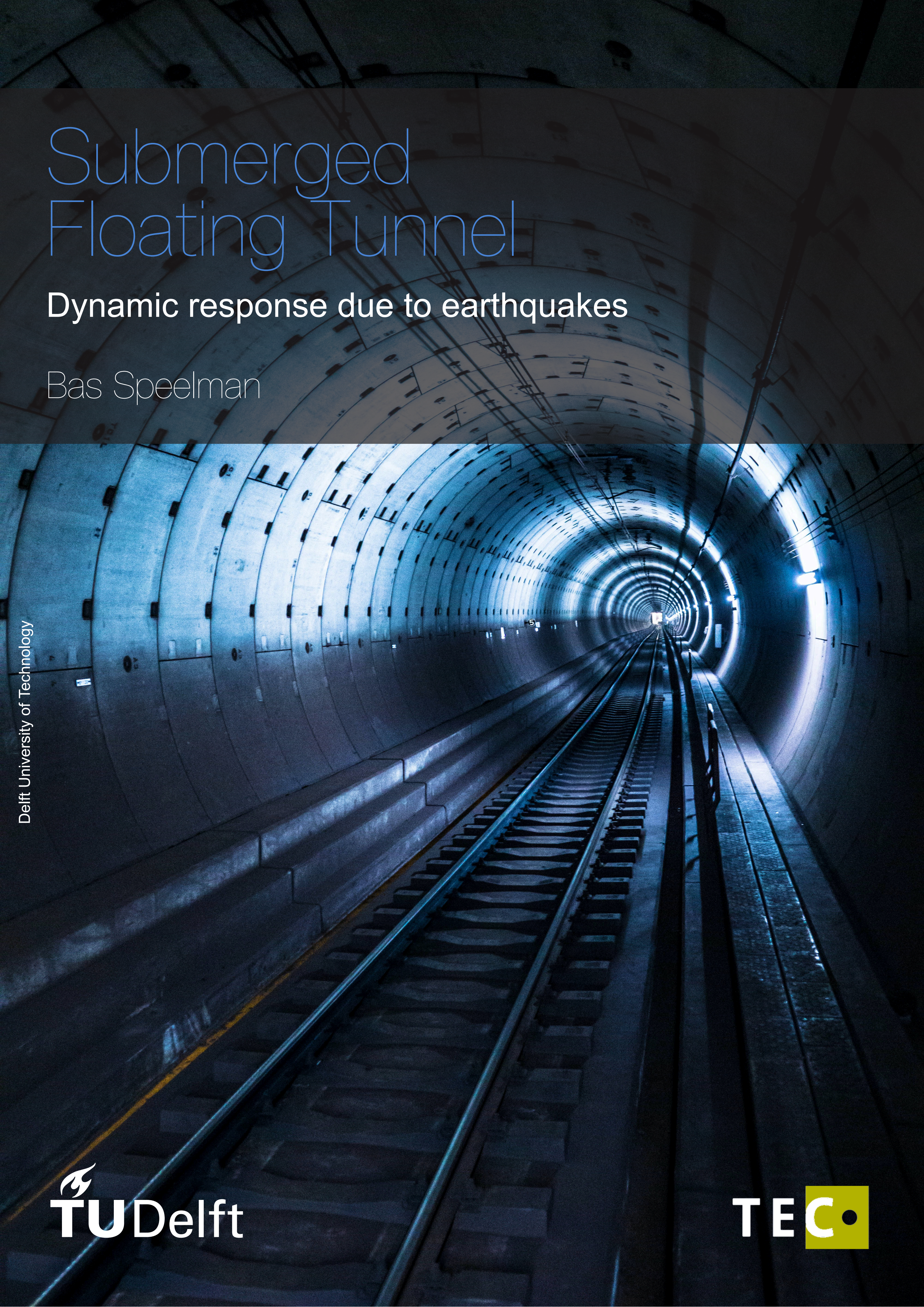

Submerged Floating Tunnel

Dynamic response due to earthquakes

Bas Speelman

Delft University of Technology

TU Delft

TEC

Submerged Floating Tunnel

Dynamic response due to earthquakes

by

Bas Speelman

to obtain the degree Master of Science
at the Delft University of Technology
to be defended publicly on Friday December 17, 2021 at 16:00

Student number:	4619250	
Thesis Committee:	Dr. ir. Dirk Jan Peters	TU Delft (supervisor)
	Prof. dr. ir. Andrei Metrikine	TU Delft
	Dr. ir. Apostolos Tsouvalas	TU Delft
	Ir. Arjan Luttikholt	Witteveen+Bos

Cover Image: https://unsplash.com/@stevenwright

TU Delft

Preface

Dear reader,

This thesis presents my study into the dynamic behaviour of submerged floating tunnels due to earthquakes. This work was conducted as the finalizing part of the Masters of Science program Hydraulic Engineering at the Faculty of Civil Engineering and Geosciences, Delft University of Technology, The Netherlands. During the period from November 2020 to December 2021, I've been engaged in researching and writing this thesis as a graduate intern at Witteveen+Bos. I would therefore like to thank Witteveen+Bos for facilitating this opportunity and for the great help I got from the people working at this company.

I want to thank my graduation committee for their supervision during my studies, their feedback, expert judgement and knowledge that made it possible for me to conduct this research. I want to especially express my gratitude to Arjan Luttikholt who I want to thank for being my daily supervisor. I am grateful for your guidance and feedback during our weekly meetings. I truly enjoyed our discussions and learn a lot from you during the last months.

Finally, I want to thank my parents who have supported me throughout my entire study for which I can't be grateful enough and my friends at the TU Delft with who I have enjoyed many good times during our studies. The last word goes to my roommate Sjors Allersma who had to endure all my complaining about my thesis but could always provided me with advice and support.

Bas Speelman
Rotterdam, December 2021

Summary

The submerged floating tunnel (SFT) is a conceptual idea that originates from the 19th century. The idea consists of a tunnel tube floating underwater where it is kept at a fixed depth by its buoyancy and by tethers that are anchored to the seabed and or by floating pontoons at the water surface. The tunnel is placed deep enough to avoid extreme weather conditions and to not hinder marine traffic but also not too deep to avoid high hydrostatic water pressures. The dynamic behaviour of this structure differs largely from classic immersed tunnels as it is not embedded in the bed and also from that of (suspension) bridges due to the hydrodynamic environment. This makes the dynamic behaviour of the SFT largely complicated and to this day still raises a lot of questions. This limited understanding contributed to the fact that worldwide not a single SFT has been constructed yet.

For this study, the dynamic response of a tether-supported SFT due to an earthquake will be analyzed. The main goal is to identify the main behaviour of an SFT due to these seismic events, to get an idea of how severe the damage could be and to know which measures in the design could be applied to reduce the impact.

To do so, a case study is introduced where the main dimensions of the tunnel are described. Next, a cross-sectional analysis is performed. This is done both analytically and by the use of the finite element model (FEM). The purpose of these analyses is to verify the input of the FEM. For the analytical model, a singular tether is described as an Euler-Bernoulli beam. By applying the Fourier transform method of analysis, the dynamic behaviour of this tether due to a simplified input signal is obtained. Subsequently, the same tether is modeled as a FEM by the use of DIANA FEA. By performing a time-history analysis for the same simplified input signal, the same results as for the analytical analysis are obtained which verifies the input. After that, the simplified model is used to model the entire tunnel which is used to study the dynamic behaviour of the SFT.

To perform the seismic analyses for the total tunnel, three different accelerograms of three different earthquakes are used. Before applying these signals to the model each of them is scaled to the spectra described by Eurocode to gain a more general input. The model is then used to perform two types of analysis. First, an eigenvalue analysis to gain the eigenperiods of the structure. Next, a time-history analysis to gain the seismic response of the structure. For the time-history analyses, the input is applied in the transverse and in the longitudinal direction, each as a separate analysis. From these analyses, the displacements and tension stresses in both the tunnel elements as in the tethers are obtained.

The last part of the study is used to analyze the effect of different design aspects of the tunnel. By using the case study as a starting point, multiple configurations are tested in where the effect of the number of mooring lines, number of tethers, tunnel alignment, tether inclination and the appliance of base isolation systems are examined.

Contents

Nomenclature

Abbreviations

Abbreviation	Definition
BC	Boundary Condition
BIS	Base Isolation System
BWR	Buoyancy Weight Ratio
DOF	Degree of Freedom
EOM	Equation of Motion
FEA	Finite Element Analysis
FEM	Finite Element Method
ODE	Ordinary Differential Equation
SFT	Submerged Floating Tunnel
SFTB	Submerged Floating Tube Bridge

Symbols

Symbol	Definition	Unit
A	Cross-sectional Area	[m^2]
A_c	Area of concrete	[m^2]
A_w	Area of displaced fluid	[m^2]
a_g	Ground acceleration	[m/s^2]
C_D	Drag coefficient Morison's equation	[-]
C_M	Inertia coefficient Morison's equation	[-]
C_t	Damping coefficient drag force tunnel	[Ns/m]
C_w	Damping coefficient drag force tether	[Ns/m]
D	Diameter	[m]
E	Young's modulus	[N/m^2]
F_d	Hydrodynamic forcing	[N]
F_{res}	Resulting force	[N]
f_t	Tension yield strength	[N/mm^2]
g	Gravitational acceleration	[m/s^2]
I	Moment of inertia	[m^4]
k_m	Spring stiffness mooring line	[N/m]
L	Tether length	[m]
l	Length non-sagged mooring lines	[m]

Symbol	Definition	Unit
l_s	Length sagged mooring lines	[m]
$M(x,t)$	Bending moment tether	[Nm]
M_t	Mass tunnel	[kg]
M_w	Added mass water	[kg]
M_x	Bending moment around x-axis	[Nm]
M_z	Bending moment around z-axis	[Nm]
N_y	Normal force	[N]
n	Number of tethers per spacing	[-]
$q(x,t)$	External load	[N/m]
R	Radius curvature	[m]
R_i	Inner radius tunnel tube	[m]
R_u	Outer radius tunnel tube	[m]
S	Soil factor	[-]
$Se(T)$	Elastic response spectrum	[m/s^2]
T	Tensile force	[N]
T_n	nth eigenperiod	[s]
th	Thickness	[m]
u_g	Ground displacement	[m]
$\ddot{u}_g$	Ground acceleration	[m/s^2]
$V(x,t)$	Shear force tether	[N]
v	Current velocity	[m/s]
$W^t(x,t)$	Total displacement tether	[m]
$\tilde{W}^t(x,t)$	Total displacement tether in frequency domain	[m]
W_0^t	Amplitude input velocity	[m]
$w(x,t)$	Transverse deflection of the neutral axis of the beam	[m]
γ_1	Importance class factor	[-]
ΔL	Spacing tethers	[m]
η	Damping correction factor	[-]
θ	Angle of attack	[deg]
ρ	Mass density	[kg/m^3]
ρ_c	Mass density concrete	[kg/m^3]
ρ_w	Mass density water	[kg/m^3]
$\sigma(x,t)$	Stress	[N/mm^2]
σ_t	Stress tether	[N/m^2]
σ_v	Standard deviation input velocity	[-]

Symbol	Definition	Unit
Φ_n	nth eigenmode	[-]
φ	Inclination angle of tethers	[deg]
ω	Frequency	[rad/s]
ω_n	nth eigenfrequency	[rad/s]

List of Figures

List of Tables

1

Introduction

The introduction of this study provides the required background information on the submerged floating tunnels. It explains the opportunities of this type of crossing and the benefits it could have compared with the traditional crossing constructions. Subsequently, the problem stated for this study is formulated from which the main research questions are formed along with the goals of this project. Next, the scope is given in which certain assumptions and constraints are provided. The last part of this chapter consists of the thesis outline in which an overview of the buildup of this report is given and how the answers to the stated problems will be obtained.

1.1. Background

Crossing waterways is something men have been doing for ages and throughout time many methods have been developed. One can think of making a bridge or a tunnel to reach the other side but in some scenarios, these traditional methods are unfavorable. Large depths and steep slopes will for example be problematic for traditional immersed and bored tunnels due to the required approach slope length and the limitations of the techniques and equipment. Even if a tunnel could be constructed in these large depths, a large tunnel length would be required which adds up to the costs of the project. Also, bridges are not always the answer. The combination of the long span and large water depth makes such a structure less feasible as the pillars will have to reach deep and/or the span of the crossing will simply be too large. Besides that, the placement of a bridge could hinder marine traffic.

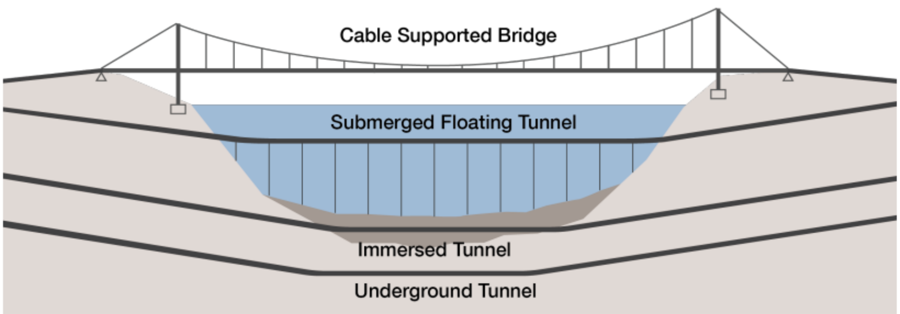

Figure 1.1: Different types of water-spanning structures ([34])

A solution for these deep crossings and large spans could be a submerged floating tunnel (SFT), also known as the Archimedes bridge, suspended tunnel or SFTB (Submerged Floating Tube Bridge). This proposed design consists of a (concrete) tunnel tube which is placed at a certain prefixed depth, deep enough to avoid extreme environmental conditions at the surface and so it would not obstruct shipping traffic, but also not too deep to avoid large hydrostatic pressures. The tunnel tube is balanced by its buoyancy and by the use of support structures. Figure 1.2 shows two support structures that are mostly considered. The first one (a) is the tether-supported SFT. As can be seen in the figure, this type of support uses cables (tethers) that anchor the tunnel tube to the bed. This system requires a tunnel tube of which the weight is smaller than the buoyancy force. This way the tunnel tends to float upwards which causes tension in the tethers which keeps the tunnel in place. One way to look at this structure is to see it as a suspension bridge that is placed upside down and underwater. Whereas the cables of the suspension bridge prevent the bridge deck from collapsing due to gravity, the tethers of the SFT prevent the tunnel from floating up due to buoyancy. The other option (b) is the pontoon-supported SFT. For this case, a tube with a weight larger than the buoyancy force is required. This way the tunnel tends to sink which is prevented by the floating pontoons which now act as the supports of the system. This system has some large disadvantages compared with the previous option as the supports of the system are now exposed to weather conditions and may obstruct shipping traffic. It does however result in a cheaper design compared with the tether-supported SFT for larger water depths.

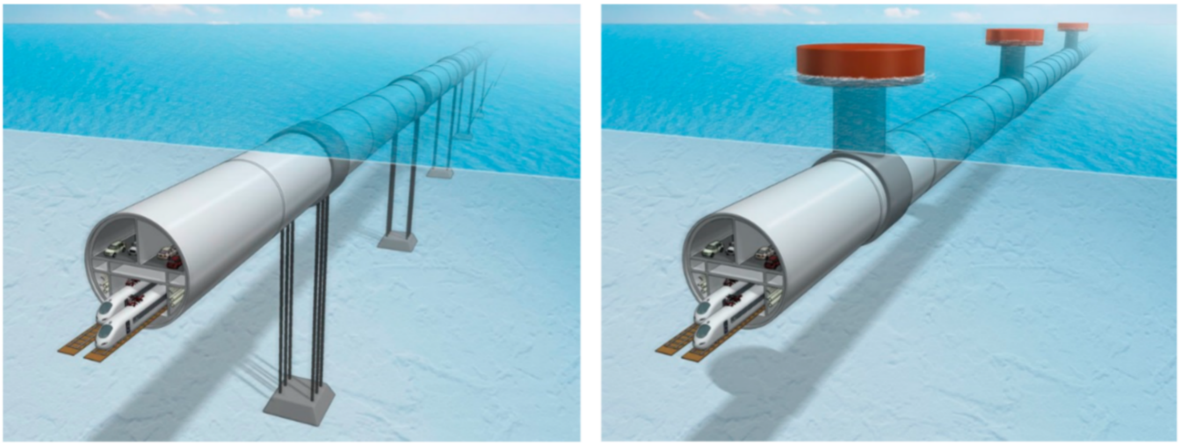

(a) (b)

Figure 1.2: Tether-supported (a) and pontoon-supported (b) [30]

1.2. Problem statement

The concept of the SFT exists for many years, yet the first one has not been built yet. This is mainly because there are still a lot of questions regarding the dynamic behavior as this is highly different from those of traditional immersed tunnels or bridges. The SFT is subjected to various dynamic loads and can (to some extent) freely move through the water. This movement through the water by these different dynamic loads requires large and complex analysis to gain some knowledge about its dynamic behavior. Much research has already been done such as wave loading/fluid-structure interaction ([16], [34]) or traffic movement inside the tunnel [33]. In this study, the dynamic behavior due to earthquakes will be analyzed. These earthquakes reach the tunnel at its connections with the beds/shores and at the anchorage points of the tethers. Understanding how these excitations affect the tunnel and how severe the damage could be is of high importance for some regions in the world. Earthquakes are one of the deadliest natural hazards and have a large annual human death toll and economical damage. Besides, whereas the regions where an earthquake could occur are mostly known, predicting one is mostly impossible. Hence, knowing what effect the earthquakes have on the SFT is of high importance.

1.3. Research objective

The main objective is to understand the dynamic response of an SFT to an earthquake and to gain knowledge of how to prevent fatal damage to the structure. Hence, the main research question can be formulated as follows;

"What is the dynamic behavior of an SFT during a seismic event and which design aspects are of importance to reduce and/or to deal with the dynamic response?"

To support this main question, some sub-questions are formulated which address the important topics of the study. These questions are;

1 How can the dynamic response of a SFT due to earthquakes be modelled?

(a) What is an appropriate method to model the tunnel and ground excitation?
(b) How can the effect of the movement through water be evaluated?

2 How does the SFT behave during an earthquake and how can the design be altered to reduce the dynamic response?

(a) Which structural elements of the SFT are the most vulnerable to earthquakes?
(b) What is the extent and potential effect of damage cause by seismic load?
(c) How could the design be manipulated or altered to affect dynamic response?

1.4. Scope

For this study, some assumptions and limitations are formulated:

1. Only the tether-supported SFT will be evaluated as this support system is the most prone to earthquakes.

2. The water body is assumed to be completely stagnant and so no currents and/or waves affect the tunnel simultaneously with the seismic activity

3. The only forcing which will be accounted for are self-weight of the tunnel, buoyancy, hydrodynamic forcing due to the movement through water, and of course the forcing due to earthquakes.

4. To demonstrate methods and findings, the study will make use of a case study in where certain design choices are made. Hence, the study only analyses one type of cross-section and one type of bathymetry which will later be described.

5. Only horizontal ground excitations are considered.

1.5. Thesis outline

The thesis report contains seven chapters of which this is the first one. The second chapter will be used to provide the necessary literature and known methodologies to tackle the problems highlighted in this study. As a starting point for certain parameters, chapter three presents a case study that will be used for the rest of the study. A bathymetry is given in which the SFT is positioned and some of the design choices of the tunnel are described. In the fourth chapter, a singular tether will be analyzed. A seismic analysis will be performed using analytical methods and with the help of Finite element analysis (FEA) software to verify in the input and results of both methods. In chapter five, the FEM made in chapter four will be used to build up the total tunnel and to perform a seismic analysis for the entire tunnel. In chapter 6, some design alternations will be analyzed to see how they affect the dynamic response of the tunnel. Chapter seven provides the conclusion, discussion and recommendations of this study. On the next page, an overview of this thesis outline is given.

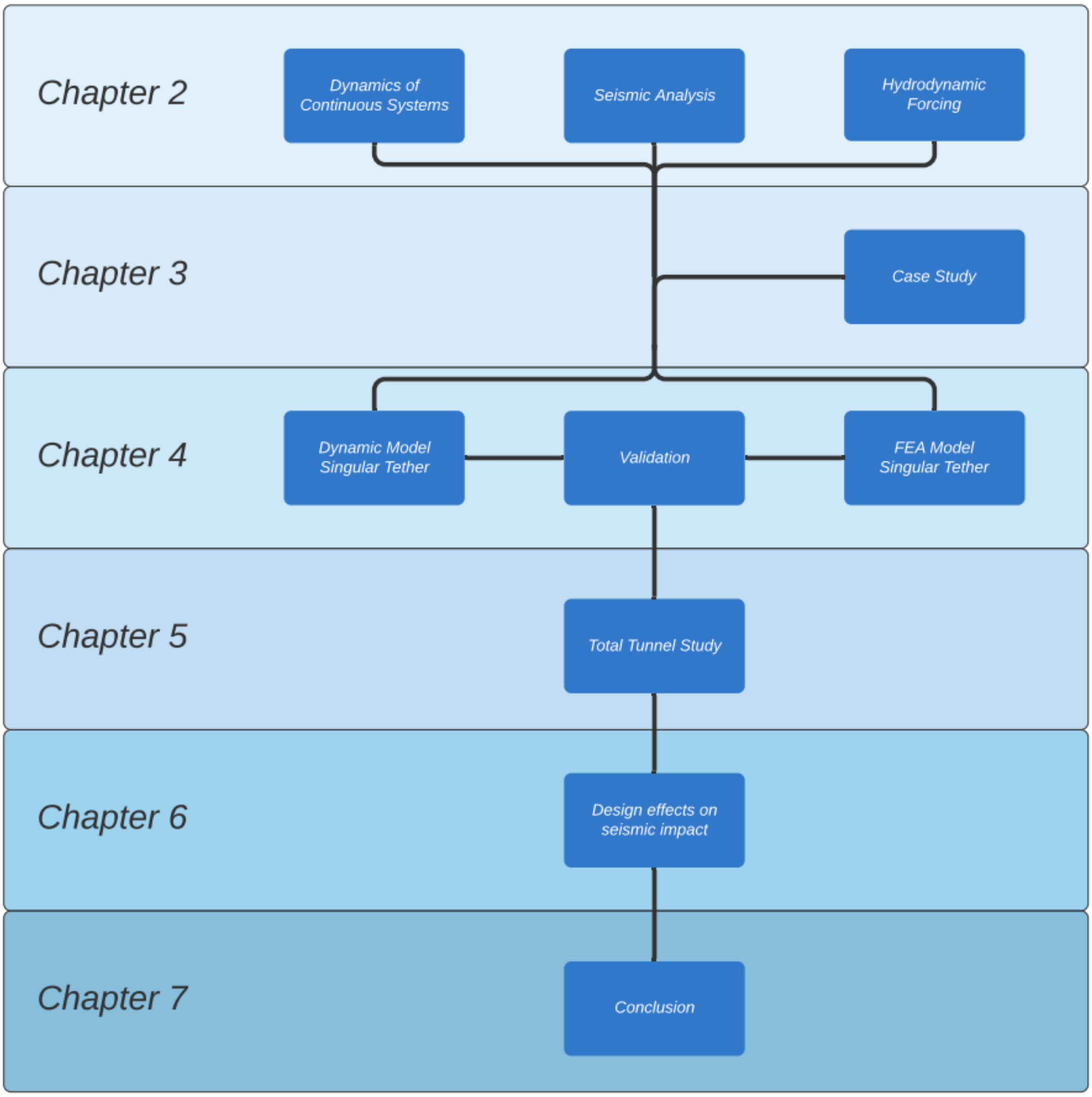

Figure 1.3: Overview of thesis outline

2

Submerged floating tunnels in a seismic environment

This chapter describes the theory applied to gain insights into the dynamic behavior of SFT's. First, the different methodologies for the seismic analyses are provided with all pros and cons. Next, the theory for describing the dynamic behavior of the tethers will be given and how the other components of the tunnel affect this behaviour. The last part consists of an explanation regarding the hydrodynamic forcing.

2.1. Methods of seismic Analyses

There are multiple methods when it comes to performing a seismic analysis. The methods which are mostly adopted will be explained here. For this section, the lecture notes for the course Structural Response to Earthquakes at the TU Delft [29] were used as a source of information.

2.1.1. Modal analysis

The first method discussed is the modal analysis. This method makes use of the modal domain in where the response is solved for each mode. From this solution, the response can be found as a superposition of the solution per mode. It is widely used as it is a simple straightforward method that still provides considerable insights into the dynamic behavior. Still, it does come with some limitations as the method is only exact for undamped systems whereas, in reality, every system has some form of damping. Damping can be expressed but only as a proportion of either the mass or the stiffness matrix. Secondly, it can only be applied to linear systems and for systems with time-independent boundary conditions.

2.1.2. Response spectrum method of analysis

Whereas most methods give the whole time history of a dynamic response, the response spectrum method only provides the peak response quantities. When designing, this is mostly sufficient since the design of a structure is mainly based on these peak values of the dynamic response and so the rest of the envelope of the response is of less interest. Besides, evaluating a single seismic event does not give a reliable design as each earthquake for even a single location can have completely different characteristics. Therefore it is of more interest to use a method that gives the results of all possible responses for multiple events. The spectra used for this method are based on the maximum response of a single-degree-of-freedom system as a function of the natural period providing peak responses for displacement, velocity or acceleration. The method requires only small computations as the response can be computed by mostly the eigenperiods of the system only and within these spectra, the stochastic nature of earthquakes is accounted for. It does give some uncertainties when it comes to non-linearity. The method can compromise for material non-linearity by scaling the spectra with a ductility factor (q-factor in Eurocode) but it cannot consider any other non-linearities. Also, the effect of damping can only be implemented by a scalar.

2.1.3. Frequency domain method of analysis

Another option is the frequency domain method of analysis. This method uses the Fourier transform integral (Eq.2.1) with allows to convert an expression from the time domain to the frequency domain. Applying this method to the given problem requires applying the Fourier transform on the equation of motion and the boundary conditions. This gives a set of ordinary differential equations. Next a solution for the equation of motion will be assumed in which the different boundary conditions will be substituted. This allows to find the unknown constants in the assumed solution and so an expression for, in this case, the displacement $W(x,\omega)$. Note that this expression is still written in the frequency domain. To gain the solution in the actual time domain the inverse Fourier transform integral is used (Eq.2.2). By using symmetry this later expression can be simplified in Eq.2.3. The computation time of this method is limited and the application is straight forward but it can only be applied to linear systems.

$$\tilde{f}(x,\omega) = \int_{-\infty}^{+\infty} f(x,t) e^{-i\omega t} dt \tag{2.1}$$

$$f(x,t) = \frac{1}{2\pi} \int_{-\infty}^{+\infty} \tilde{f}(x,\omega) e^{-i\omega t} d\omega \tag{2.2}$$

$$f(x,t) = \frac{1}{\pi} \int_{0}^{\omega^+} \text{Re}\left[\tilde{f}(x,\omega) e^{-i\omega t}\right] d\omega \tag{2.3}$$

2.1.4. Direct time integration method

The final method mentioned is the direct time integration method. This method is a more general method for any time-dependent analysis in where the dynamic response is calculated for each time step by the use of an integration method. Applying this method gives an exact solution for any system, damped or undamped and linear or nonlinear. On the downside, it does require a larger computation time and gives little insight into the dynamic behavior of the system.

2.1.5. Summary and selected method for this study

To perform the analytical analysis, one of the above-elaborated methods has to be selected. This analysis will be used for the singular tether only as a verification of the time-history analysis performed with the finite element model. First the modal analysis. The main disadvantage of this method is that it required time-independent boundary conditions. As will be explained later in chapter 4, damping is added to one of the boundary conditions which already makes this method inapplicable. Next, the Response spectrum method. This method would be a fast way for computing the dynamic response but it only provides the peak responses of the system. The finite element model, which will be evaluated later in chapter 4, makes use of a time-history analysis that provides the dynamic behavior throughout the total time domain. Hence, since the purpose of the analysis of the singular tether is only to control the input of the FEA model, it would be a logical choice to make us of a method that provides the total dynamic behavior as well which makes the response spectra method less interesting. As for the direct time integration, this method may provide the most exact solution but is by far the most demanding when it comes to computation. As the singular tether is still a relatively simple model, applying such a method would be too much as other less computational demanding methods still provides decent outcomes. This leaves the frequency domain method of analysis which will be the method applied for this problem. As it is a straightforward method that gives an exact solution for a damped system with a relatively fast computation, this method seems to be the most applicable for the given problem in chapter 4.

2.2. Dynamics of continuous systems: Euler-Bernoulli Beam

As a starting point for this study, first, the dynamic behavior of the tethers will be examined. This will be done by the use of the Euler-Bernoulli beam element. Unlike a rigid body element, the Euler-Bernoulli beam is modeled as a continuous system with an infinite number of spatial nodes for each degree of freedom. This allows a description for deformations within the element whereas, for a rigid body element, such deformations can not be described. Figure 2.1 shows a tensioned beam subjected to a spatial and time-dependent external load. By the use of Newton's second law and by employing constitutive relations, the equation of motion (EoM) for this element can be derived which is given as equation 2.4.

$$\rho A \frac{\partial^2 w}{\partial t^2} + \frac{\partial^2}{\partial x^2}\left(EI\frac{\partial^2 w}{\partial x^2}\right) - \frac{\partial}{\partial x}\left(T\frac{\partial w}{\partial x}\right) = q_1(x,t) \tag{2.4}$$

Where:

$w(x,t)$	= Transverse deflection of the neutral axis of the beam
ρ	= Mass density
A	= Cross-sectional area
E	= Young's modulus
I	= Moment of inertia
T	= Tensile force
$q_1(x,t)$	= external loading

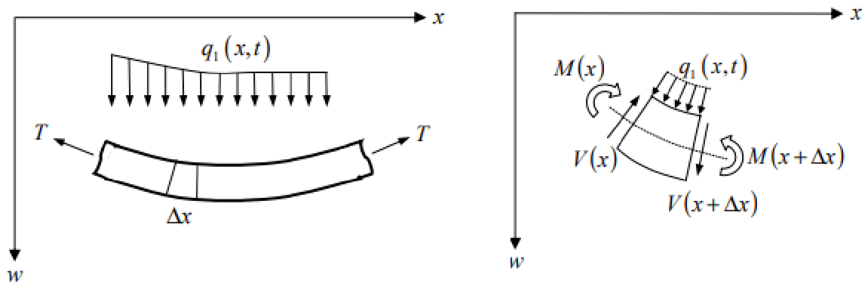

Figure 2.1: Tensioned beam (Metrikine, 2006 [18])

To solve for the eigenvalue problem of the EoM it is required to formulate the boundary conditions. Because the solution of this equation is not only space but also time-dependent, a different solution procedure is required compared to ordinary differential equations. The procedure applied for this problem is called the separation of variables which will be explained in appendix A, along with the total solution for the eigenvalue problem.

2.3. Hydrodynamic Forcing

When a body moves through the water, the surrounding water affects this movement. In this case, this effect will be evaluated as a force on the moving tethers and tunnel elements which consists of an inertia and a drag component. The method used by Wu et al 2018 [31], who also analyzed the tethers of SFT's during earthquakes, used the Morison's equation [12] to evaluate this effect. The same method will be adopted for this study. The original Morison's equation is given as Eq.2.5.

$$F_D = \underbrace{\frac{1}{2}\rho_w D C_D \left(v\right)\left|v\right|}_{\text{Drag force}} + \underbrace{\frac{\pi}{4}\rho_w D^2 \left(C_M - 1\right)\frac{\partial v}{\partial t}}_{\text{Inertia force}} \tag{2.5}$$

Where:

ρ_w	= Mass density water
D	= Outer diameter tether
C_D	= Drag coefficient
C_M	= Inertia coefficient
v	= current velocity

The equation above shows the force due to the movement of the structure and due to the current velocity. As for this study, the current velocity isn't of importance but those of the seismic excitation is, Eq.2.5 shall be rewritten in terms of $W^t(x,t)$ which is the total displacement of the system. This total displacement can be decomposed into a relative displacement and a displacement of the input motion.

$$W^t(x,t) = W(x,t) + u_g(t) \tag{2.6}$$

Substituting the total displacement in the Morison's equation gives:

$$F_D = \frac{1}{2}\rho_w D C_D \frac{\partial W^t}{\partial t}\left|\frac{\partial W^t}{\partial t}\right| + \frac{\pi}{4}\rho_w D^2 \left(C_M - 1\right)\frac{\partial^2 W^t}{\partial t^2} \tag{2.7}$$

It is noted that the drag term in the equation above is non-linear. This would be problematic when preforming the analysis and so this term will be linearised. Housseine et al. 2005 [22] described a stochastic linearization of the damping component for regular and irregular motion. For the regular motions, the Morison equation can be linearized as 2.8

$$F_D = \frac{1}{2}\rho_w D C_D \left(\frac{8}{3\pi}\omega W_0^t\right)\frac{\partial W^t}{\partial t} + \frac{\pi}{4}\rho_w D^2 \left(C_M - 1\right)\frac{\partial^2 W^t}{\partial t^2} \tag{2.8}$$

Where W_0^t is the amplitude of velocity of the input motion and ω the frequency. For irregular motions (such as earthquakes), the Morison equation is linearized as 2.9

$$F_D = \frac{1}{2}\rho_w D C_D \left(\sqrt{\frac{8}{\pi}}\sigma_v\right)\frac{\partial W^t}{\partial t} + \frac{\pi}{4}\rho_w D^2 \left(C_M - 1\right)\frac{\partial^2 W^t}{\partial t^2} \tag{2.9}$$

Where σ_v is the standard deviation of the velocity of the input motion.

3

Design Starting point

To apply the described theory and methodologies presented in chapter 2, a case study will be defined in this chapter. This case study will be used as a starting point for designing the SFT in where some design aspects will be predefined and used throughout the rest of the study. First, the environment in where the SFT is placed will be described. Next, a static design for the tunnel will be made which shall later be tested for the seismic events

---

3.1. Bathymetry and Environmental Conditions

To start with, a bathymetry is made in which the tunnel is situated. The use of SFT's is most beneficial to cross deep waters. The tunnel itself will be held at a constant water depth and so by using a varying water depth, various tether lengths can be obtained. Figure 3.1 shows the bathymetry used for this study. In this design, a constant tunnel depth of 50 meters below the water surface is used. The water depth varies between 200 up to roughly 1000 meters which results in the tether length varying from 150 to 950 meters. The tethers are only drawn for an illustrative purpose, the amount and distances between the tethers shall be determined in the static design. The total tunnel length amounts to roughly 2 km and is connected to a land tunnel at both ends. For the scope of this study, the water is assumed fully stagnant and so no currents or waves are formed. As for the ground characteristics, a rock-like formation is assumed. According to Eurocode 8 [11], this gives the ground type A which will be of importance later during the seismic analysis.

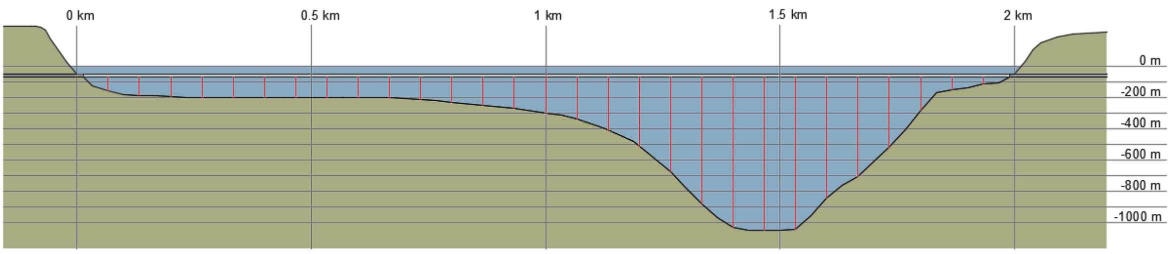

Figure 3.1: Bathymetry case study

3.2. Tunnel design

For the case study, three components of the tunnel will be evaluated. The tunnel cross-section, the tethers and the mooring lines. For each, the design parameters which are of importance will be given here.

3.2.1. Tunnel elements

First the tunnel cross-section, a design has been made which accounts for static loads only. In here, the only loads which are accounted for are 1) self-weight and 2) buoyancy force. The ratio between these two gives the buoyancy weight ratio (BWR) which is the ratio between the upwards force and the downwards force (Eq.3.1).

$$\text{BWR} = \frac{F_{\text{buoyancy}}}{F_{\text{self weight}}} \tag{3.1}$$

If the BWR would be less than 1, i.e. the downwards force is larger than the upwards force, the tunnel will simply sink. Hence, for a tether-supported SFT, one wants to always have a BWR of at least 1 so that the tunnel tends to float upwards. When the BWR increases the tension in the tethers will increase as well which has a large effect on the dynamic behavior. A study was carried out by Long et al [32] who did a feasibility study on BWR's of SFT's. They found an optimum of 1.2 for this ratio. In the design for this tunnel, the same BWR will be used.

The procedure for the tunnel design is as follows; first a cross-section for the concrete tunnel tubes is defined. When designing this cross-section the desired BWR of 1.2 is the objective. As the self-weight consists of the weight of the concrete and the buoyancy force is determined by Archimedes law (upward force equals the weight of the fluid displaced by the body), this ratio asks for the right balance between square meters of concrete and square meters of displaced fluid per cross-section. The BWR can so be expressed as;

$$\text{BWR} = \frac{A_w \rho_w}{A_c \rho_c} \tag{3.2}$$

Where:

A_w = Area of displaced fluid ($\frac{1}{4}\pi D^2$)
ρ_w = Mass density water
A_c = Area of concrete
ρ_c = Mass density concrete

On the next page, an overview of the cross-section used for this study is given. This cross-section consists of two tunnel tubes (one for each traffic direction). The weight of the water and concrete are taken as 1000 kg/m^3 and 2500 kg/m^3, respectively. This results in a cross-section with a BWR of 1.2. The next step of designing the tunnel is to determine the dimensions of the tethers for the resulting tension force caused by the buoyancy.

Dimensions and Properties Tunnel Cross-section

Properties overview

Geometrical properties

Cross-section	Area	
Buoyancy Area *(total)*	480	m^2
Concrete Area *(total)*	160	m^2

Material properties

Density	Value	
Water	10.00	kN$/m^3$
Reinforced concrete	25.00	kN$/m^3$

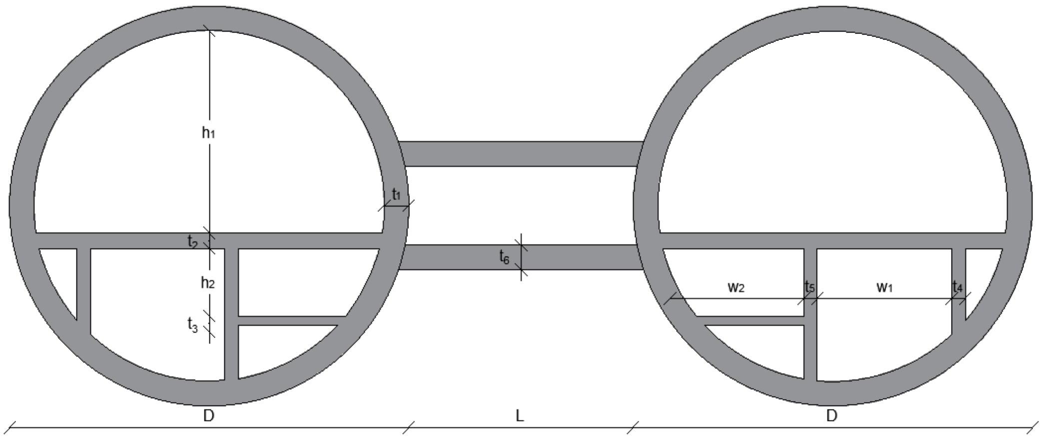

Figure 3.2: Tunnel dimensions

Cross-section

	Section	Value	
D	Outer tube diameter	17.50	m
L	Length connection bar	12.50	m
h_1	Traffic area height	9.00	m
h_2	Lower area height right part	3.00	m
w_1	Lower area width middle part	6.00	m
w_2	Lower area width right part	5.50	m

	Section	Value	
t_1	Outer wall thickness	1.60	m
t_2	Traffic area floor thickness	0.70	m
t_3	Lower floor thickness	0.40	m
t_4	Inner wall thickness left	0.60	m
t_5	Inner wall thickness right	0.60	m
t_6	Connection bar thickness	0.80	m

Uplift

Force	Value	
Buoyancy	4800	kN$/m$
Weight	4000	kN$/m$
Resulting force	800	kN$/m$

Ratio	Value	
BWR	1.20	-

3.2.2. Tethers

The tethers act as the support of the tunnels throughout the span and are under constant tension due to the resulting uplifting force. They must be kept under tension to prevent them from slack and/or loss of their function. The tension can be calculated by the resulting force in the tunnel elements (see the previous page), the spacing of the tethers and the cross-section area of these elements. The tension force (T) is expressed as Eq. 3.3 from where the tension stress in the tethers can easily be evaluated by Eq.3.4

$$T = \frac{F_{res}\Delta L}{n} \tag{3.3}$$

$$\sigma_t = \frac{T_n}{A_t} \tag{3.4}$$

Where:

F_{res} = Resulting force in the tunnel element
ΔL = spacing of tethers
n = Number of tethers

The tethers will be designed as steel tubular pipes with a constant cross-section throughout the length. The table below shows the dimensions and properties of the tethers. As a starting point, a spacing of $\Delta L = 100$ m is used and per cross-section two tethers will be attached to the tunnel ($n = 2$).

Table 3.1: Tether dimensions and properties

Parameter	**Symbol**	**Value**	**Unit**
Diameter	D	0.75	m
Cross-sectional area	A_t	0.20	m^2
Young's modulus	E	$2 \cdot 10^{11}$	N/m^2
Mass density	ρ_s	7800	kg/m^3
Spacing	ΔL	100	m
Number of tethers	n	2	-
Tension Force	T	39950	KN
Stress	σ_t	200	N/mm^2
Thickness	th	0.1	m
Tension Yield Strength	f_t	420	N/mm^2

The steel thickness is chosen such that the tension stress under permanent static loading is kept around 200 N/mm^2 which is below the tension yield strength $f_t = 420$ N/mm^2, leaving capacity for the seismic loading.

3.2.3. Mooring lines

The mooring lines are added to the system as a horizontal restraint. Without these, the tunnel could drift away due to currents or other loads causing large deformation. These mooring lines are for this study simplified as linear springs. Figure 3.3 visualises the configuration of these elements.

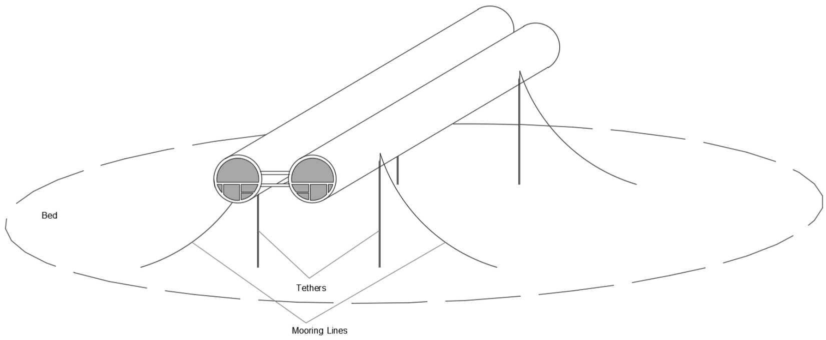

Figure 3.3: Configuration of mooring lines and tethers

Due to the self-weight of these lines, the mooring lines sag which reduces the stiffness of these lines. Normally, for non-sagging lines, a linear relation between elongation and tension force is found. For sagged lines, this relation is non-linear (Peters, 1993 [24]).

This non-linear behaviour comes from the fact that, when starting from the initial state, the line stays more or less sagged as the elongation increases. During this state, the build-up of the tension force is limited. Only after the line has been elongated such that a state is reached with little to no sag, the tension force will build as would be for non-sagged lines. This relation is shown in figure 3.4 which gives the relation between elongation Δl_s and tension force T (shown as (a)). (d) gives the axial cable stiffness. As can be seen, as the elongation increases the slope $\frac{dT}{d\Delta l_s}$ approaches the axial stiffness of the non-sagged line.

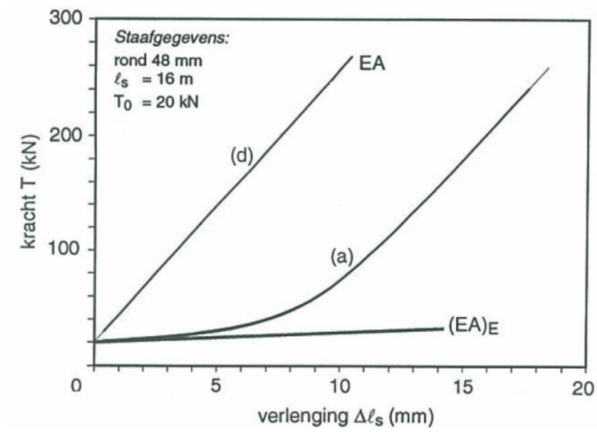

Figure 3.4: relation between tension force T and elongation Δl_s [24]

The method of analysis to solve for the dynamic behaviour can only be applied for linear systems. Therefor, the behaviour as described above cannot directly be applied in the stated problem. To make it applicable, the tether will be linearized in the range of occurring tensile forces. By obtaining the lower and upper bound of the tension force in the mooring lines the behaviour can be linearized between these two values. This introduces am iterative process in where the range of the tension forces applied for the linearization needs to be checked with the resulting tension forces. In (Peters, 1993 [24]) The linearised stiffness of the mooring line $(EA)_{sec}$ is expressed as;

$$(EA)_{sec} = \frac{EA}{1 + EA\frac{(gl)^2(T_i+T_j)}{24T_i^2T_j^2}} \tag{3.5}$$

Where:

EA	= Axial stiffness mooring line
g	= gravitational acceleration
l	= length without no sag
T_i	= Lower bound tension force
T_j	= Upper bound tension force

It is noted that if the range of the upper and lower bound increases, the linearization becomes less accurate. After the linearization the axial stiffness of the mooring lines is defined as;

$$k_m = \frac{EA_{sec}}{l_s} \tag{3.6}$$

The length l (applied in Eq.3.5), which is the length of the mooring line if there would be no sag, depends on the local depth. For this study, it's assumed that each mooring line inclines 45 degrees with the bed. Hence, if the local depth would be expressed as d, the length of the mooring line at that depth will be $\sqrt{2}d$. Furthermore a young's modulus of $E = 3 \cdot 10^9 N/m^2$ and a cross-sectional area of $A_m = 0.75\ m^2$ are applied. the length l_s in Eq.3.6 is the length of the sagged line. This length is characterized by its own weight and the tension force. This tension force results only from the self-weight as the buoyancy force of the tunnel is only balanced by the tethers. The length of the sagged line is expressed by Eq.3.7. Figure 3.5 gives an overview of the symbols.

$$l_s = l\left(1 + \frac{8}{3}\left(\frac{f}{l}\right)^2\right) \tag{3.7}$$

$$f = \frac{gl^2}{8T}$$

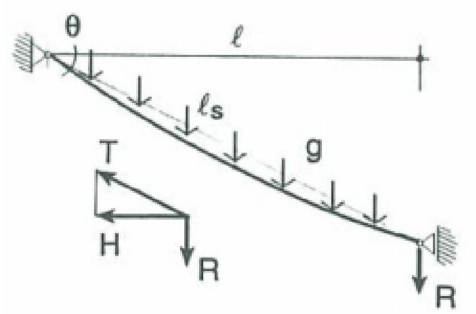

Figure 3.5: Definitions of symbol for sagged line (Peters, 1993 [24]

4

Tether Study

In this chapter, the dynamic behavior of a single vertical tether will be analyzed. The theory introduced in chapter 2 will be applied to one of the tethers from the case study given in chapter 3. A dynamic analysis will be performed by using the frequency domain method of analysis. Next, the tether will be modeled with the use of a finite element software and a time history analysis will be performed to verify both the calculations and the model.

4.1. Dynamic system

The first step of the analysis is to describe the tether construction as a dynamic system. As explained in chapter 2, the tether will be analyzed as an Euler-Bernoulli beam. The figure on the next page gives an overview of how the tether will be implemented as a dynamic system. In here the displacement $w(x,t)$ is shown with its positive direction. The positive direction of the x-axis will be vertically towards the surface and has the value $x = 0$ at the bed and $x = L$ at the connection with the tunnel, where L is the length of the tether. The characteristics of the tether will consist of the property materials (material density ρ and Young's modulus E), cross-sectional characteristics (cross-sectional area A and moment of inertia I) and the tension force in the tether T. All values for these parameters are given in the previous chapter and are assumed constant throughout the length.

The tunnel element has been implemented at the boundary conditions at $x = L$. This element will be characterized by its mass M_t and by the damping C_t which will be evaluated in the same manner as described in section 2.3. The mooring lines (described as linear springs with stiffness k_m) are also implemented at this boundary condition. $q(x,t)$ represented the forcing on the system. In this study, this forcing only consists of the hydrodynamic forcing F_D as described in section 2.3 and the seismic forcing. The latter will not be included in this $q(x,t)$ but in the boundary conditions at $x = 0$. This seismic motion is shown in the figure as the ground acceleration $\ddot{u}_{ag}(t)$.

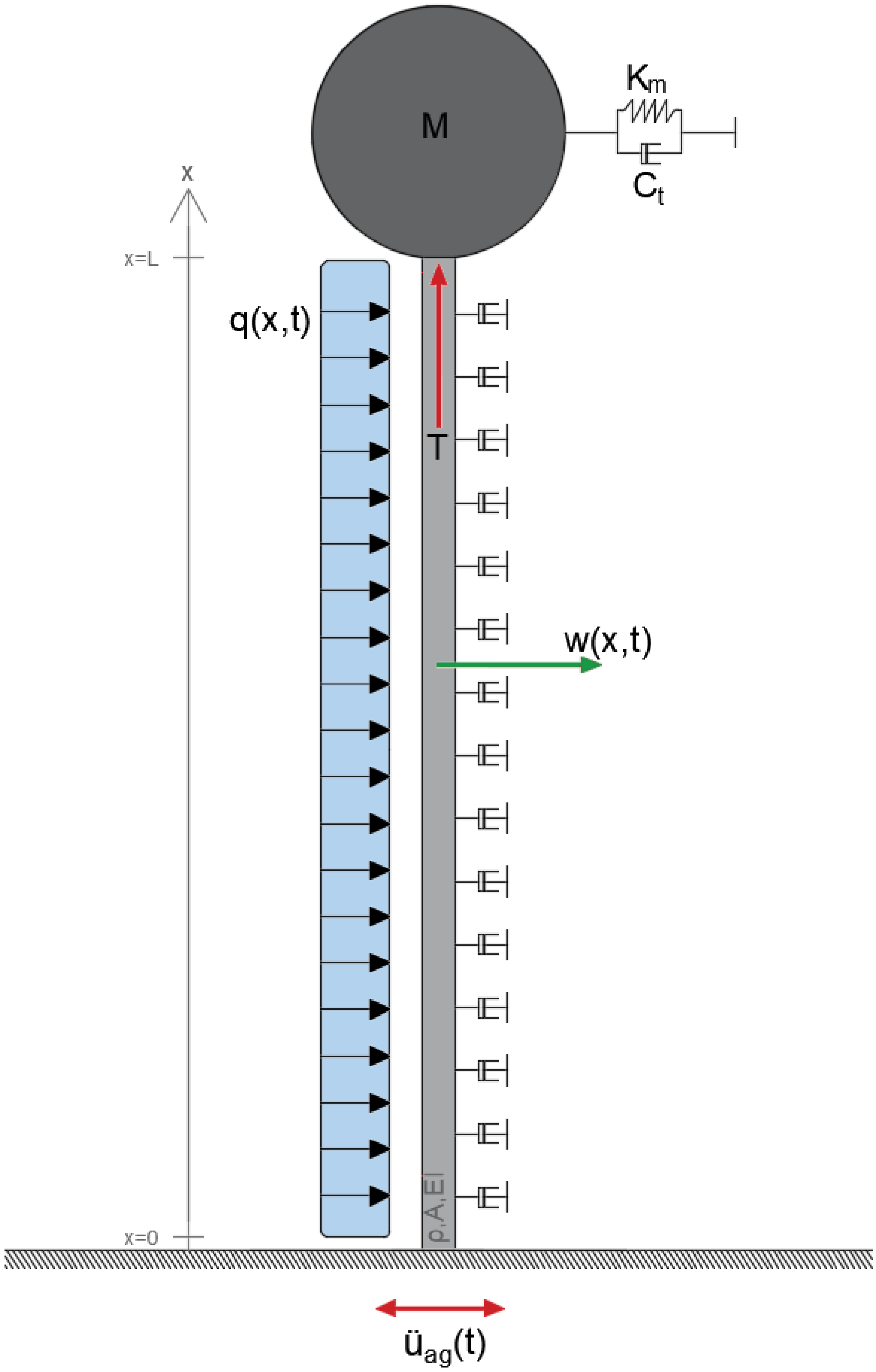

Figure 4.1: Dynamic system singular tether

4.2. Equation of motion and boundary conditions

To first step of this dynamic analysis is to formulate the governing equations which describe the dynamic response. These equations will consist of the equation of motion (EoM) and the boundary conditions (BC's). First the EoM, which has already been given in chapter 2, but is shown here again (now with constant characteristic values and in terms of total displacement W^t).

$$\rho A \frac{\partial^2 W^t}{\partial t^2} + EI \frac{\partial^4 W^t}{\partial x^4} - T \frac{\partial^2 W^t}{\partial x^2} = q(x,t) \tag{4.1}$$

The forcing $q(x,t)$ consists only of the hydrodynamic forcing as in Eq.2.7 but now with the linearized drag force. The seismic forcing (which will be given later) will, for this analysis, only consist of a regular harmonic. Hence, for the linearization, Eq.2.8 will be applied. Substituting this in the EoM gives;

$$\rho A \frac{\partial^2 W^t}{\partial t^2} + EI \frac{\partial^4 W^t}{\partial x^4} - T \frac{\partial^2 W^t}{\partial x^2} = -\left(\frac{1}{2}\rho_w D C_D \left(\frac{8}{3\pi}\omega W_0^t\right)\frac{\partial W^t}{\partial t} + (C_M - 1)\frac{\pi}{4}\rho_w D^2 \frac{\partial^2 W^t}{\partial t^2}\right) \tag{4.2}$$

which is rewritten as:

$$(\rho A + M_w)\frac{\partial^2 W^t}{\partial t^2} + EI \frac{\partial^4 W^t}{\partial x^4} - T \frac{\partial^2 W^t}{\partial x^2} + C_w \frac{\partial W^t}{\partial t} = 0 \tag{4.3}$$

Where:

M_w	= Added mass water	$= (C_M - 1)\frac{\pi}{4}\rho_w D^2$
C_w	= Damping coefficient drag force	$= \frac{1}{2}\rho_w D C_D \cdot \frac{8}{3\pi}\omega W_0^t$

As for the values of the coefficients C_M and C_D, these are taken as $C_D = 1$ and $C_M = 2$ which are mostly recommend for submerged cylindrical shapes [20].

Secondly, the boundary conditions have to be formulated. Since the highest space derivative in the EoM is of the fourth order, four boundary conditions are required, two at $x = 0$ and two at $x = L$. Those at the bed ($x = 0$) are straightforward. Since the EoM is written in terms of total displacement, the displacement at $x = 0$ must be set equal to that of the seismic input motion $u_{ag}(t)$ which forms the first boundary condition (Eq.4.4). For the other boundary condition, the tether is assumed to have a clamped fixation at the bed which allows for no rotation at that point (Eq.4.5).

$$W^t(0,t) = u_{ag}(t) \tag{4.4}$$

$$\left.\frac{\partial W^t}{\partial x}\right|_{x=0} = 0 \tag{4.5}$$

Considering the upper end of the tether. It is assumed that the tether has a hinged fixation at the tunnel. This will give a zero momentum conditions (Eq.4.6). The last boundary condition will describe a force balance. Figure 4.2 shows this balance. Here, Newton's second law is applied (Force equals mass times acceleration). Hence, the mass of the tunnel times the acceleration of the tether evaluated at $x = L$ must equal all acting forces. These forces consist of the shear force in the tether, the horizontal component of the tension force T (which can be computed by the slope of the tether), and the forces due to the damping and the mooring line. Setting up this balance and by using the constitutive relation, the final boundary condition can be formulated (Eq.4.7).

$$\left.\frac{\partial^2 W^t}{\partial x^2}\right|_{x=L} = 0 \tag{4.6}$$

$$M_t \left.\frac{\partial^2 W^t}{\partial t^2}\right|_{x=L} = EI \left.\frac{\partial^3 W^t}{\partial x^3}\right|_{x=L} - T \left.\frac{\partial W^t}{\partial x}\right|_{x=L} - k_m W^t(L,t) - C_t \left.\frac{\partial W^t}{\partial t}\right|_{x=L} \tag{4.7}$$

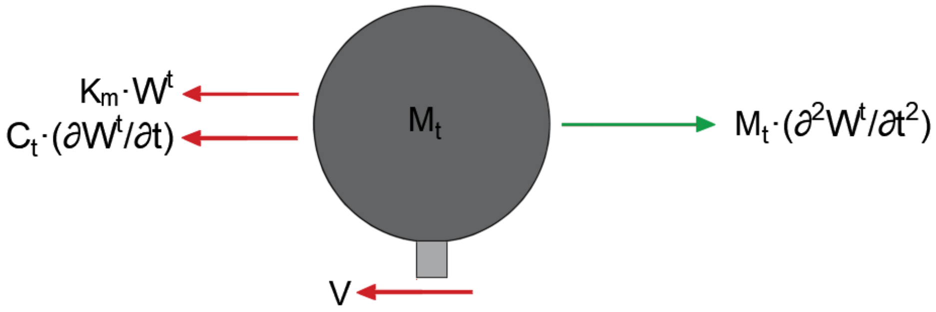

Figure 4.2: Boundary condition 4

4.3. Eigenvalue problem

With the governing equations known, the eigenvalue problem can be solved for gaining the eigenfrequencies and eigenmodes. To do so the homogeneous and undamped version of the EoM is used which reads as follows;

$$(\rho A + M_w)\frac{\partial^2 W^t}{\partial t^2} + EI\frac{\partial^4 W^t}{\partial x^4} - T\frac{\partial^2 W^t}{\partial x^2} = 0 \tag{4.8}$$

By using an assumed solution in the form of Eq.4.9 and substituting it in the EoM shown above, two functions can be obtained. One with only x as a variable and one with only t as a variable.

$$W^t(x,t) = \Phi(x)Q(t) \tag{4.9}$$

Then, with the use of the boundary conditions, one can get a solution of systems from which the eigenfrequencies can be obtained. The total derivation of this is shown in Appendix A. For now only the resulting set of equations is given.

$$EI\Phi''''(x) - T\Phi''(x) - \omega^2(\rho A + M_w)\Phi(x) = 0 \tag{4.10}$$

$$\Phi(0) = \Phi'(0) = \Phi''(L) = \omega^2 M_t \Phi(L) + EI\Phi'''(L) - T\Phi'(L) - k_m\Phi(L) = 0 \tag{4.11}$$

To solve this set of equations a solution is assumed in the following form;

$$\Phi(x) = C1e^{i\lambda_1 x} + C2e^{-i\lambda_2 x} + C3e^{\lambda_3 x} + C4e^{-\lambda_4 x} \tag{4.12}$$

with:

$$\lambda_1 = \beta; \quad \lambda_2 = -\beta; \quad \lambda_3 = i\beta; \quad \lambda_4 = -i\beta \tag{4.13}$$

$$\beta = \frac{T + \sqrt{T^2 + 4EI(\rho A + M_w)\omega^2}}{2EI} \tag{4.14}$$

By substituting the assumed solution in the four boundary condition a system of ordinary differential equations (ODE's) is formed. From this system the eigenfrequencies can be obtained. This has been done by the use of Maple [17]. For now only the resulting frequencies are shown, the total analysis is provided in appendix A.

$\omega_1 = 2.76$ rad/s $=0.44$ Hz
$\omega_2 = 24.02$ rad/s $=3.82$ Hz
$\omega_3 = 65.46$ rad/s $=10.42$ Hz
$\omega_4 = 128.75$ rad/s $=20.49$ Hz

With every eigenfrequency ω_n comes an eigenmode $\Phi_n(x)$. These are obtained my substituting each ω_n in the assumed solution for $\Phi(x)$ giving the eigenmode $\Phi_n(x)$. This solution still contains the unknown constants so only the shape of the eigenmodes can be found whereas for the amplitude, the forced vibrations of the system needs to be solved for.

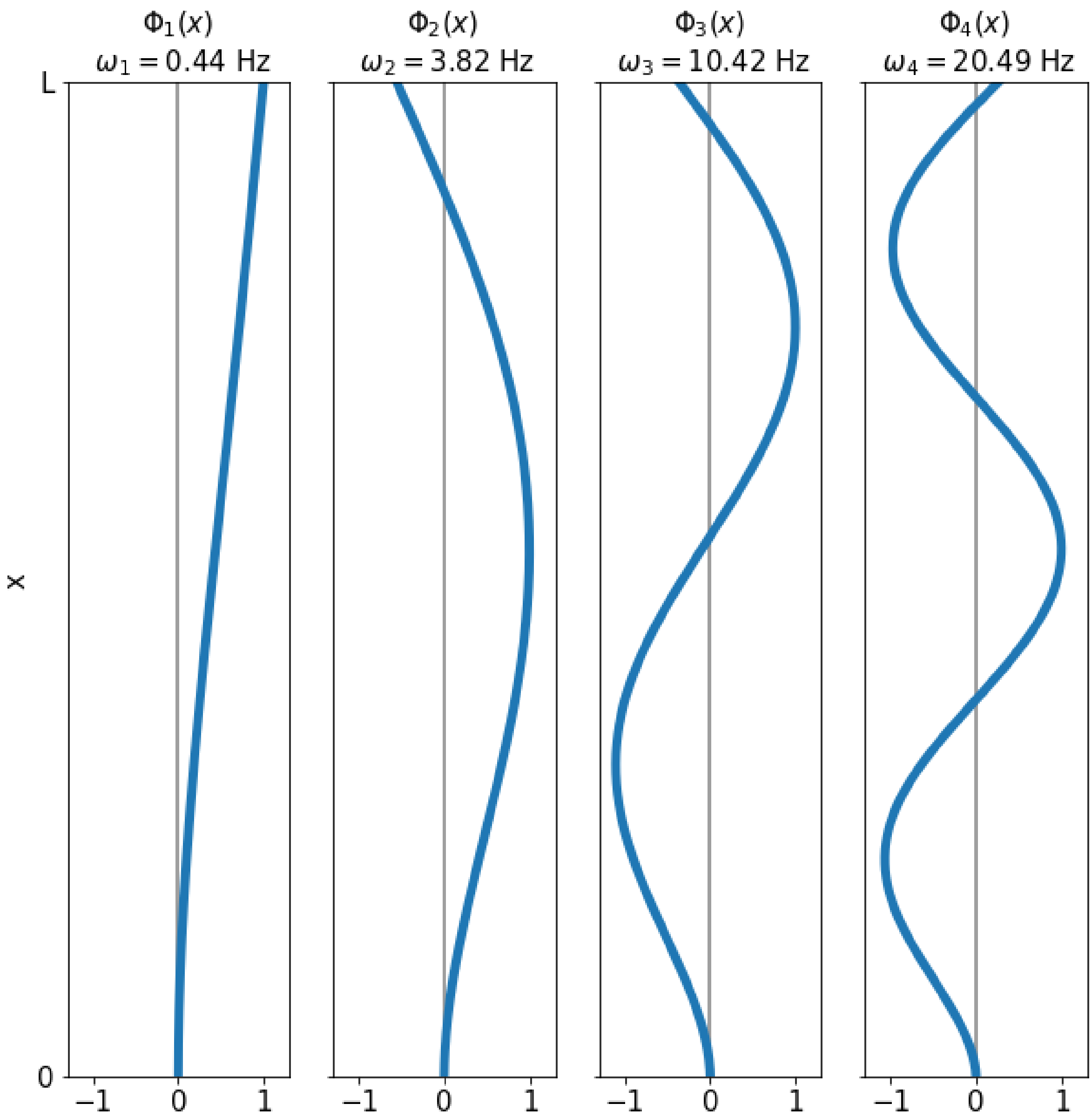

Figure 4.3: Eigenmodes of tether

4.4. Frequency domain analysis

To perform the frequency domain method of analysis, a seismic input is required. For this analysis, a simple sinusoidal motion will be used to keep the computations accessible. Later, when performing the analysis for the tunnel SFT, a more realistic input motion will be used.

For now, the input motion expressed as Eq.4.15 will be used, This expression gives the ground displacement as this is how it's required in the first boundary condition (Eq.4.4).

$$u_g(t) = \begin{cases} 0.01\,\mathrm{sin}(10t) & 1 \leq t < 10 \\ 0 & t < 1 \;\&\; t \geq 10 \end{cases} \tag{4.15}$$

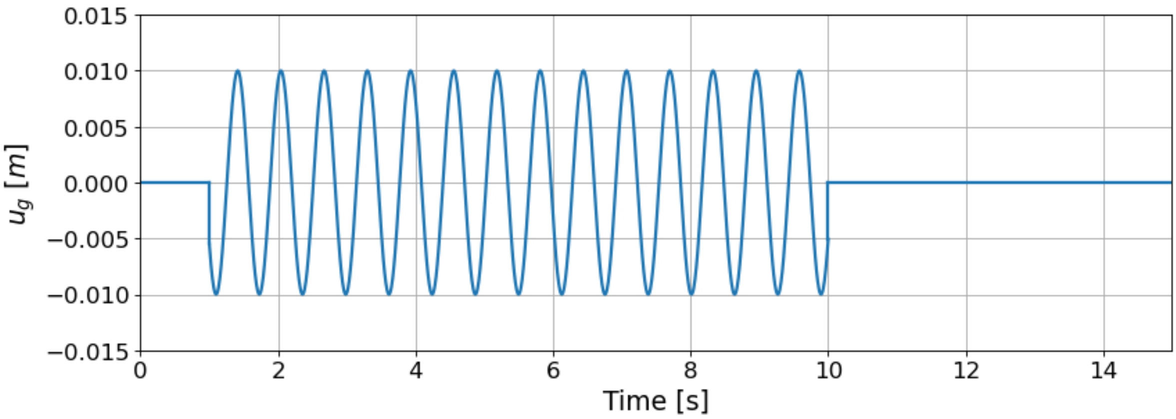

Figure 4.4: Input ground displacement time domain

As this ground motion will be applied in the frequency domain analysis, it is required to first transform this motion to this domain. This will be done by applying the Fourier transformation (Eq.2.1). This gives a function with variable ω instead of t. Plotting this transformed function results in the the following;

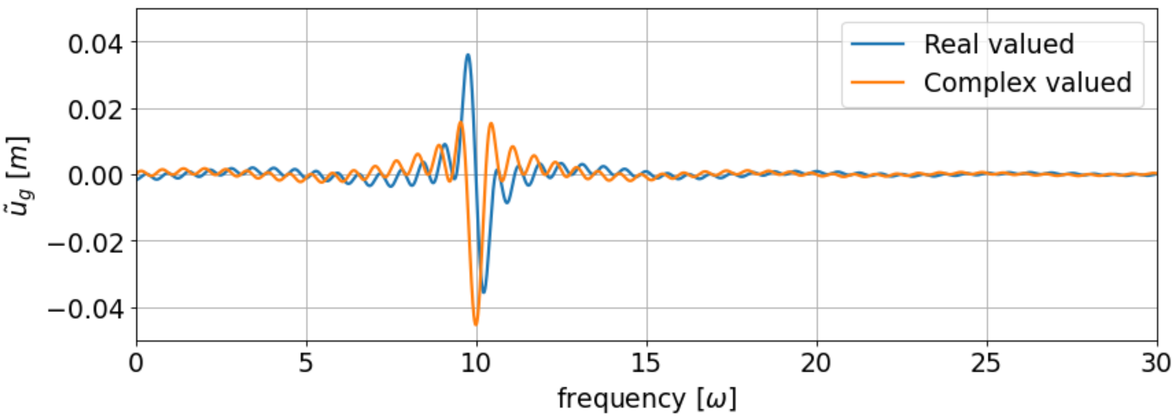

Figure 4.5: Input ground displacement frequency domain

As was done for the input motion, the EoM and boundary conditions are required to be written in the frequency domain as well. Applying the Fourier transform gives the following set of ordinary differential equations.

$$-\omega^2 (M + M_w) \tilde{W}^t(x,\omega) + EI\tilde{W}^{t''''}(x,\omega) - T\tilde{W}^{t''}(x,\omega) + C_w i\omega \tilde{W}^t(x,\omega) = 0 \tag{4.16}$$

$$\tilde{W}^t(0,\omega) = \tilde{u}_g(\omega) \tag{4.17}$$

$$\tilde{W}^{t'}(0,\omega) = 0 \tag{4.18}$$

$$\tilde{W}^{t''}(L,\omega) = 0 \tag{4.19}$$

$$-\omega^2 M_t \tilde{W}^t(L,\omega) = -k_m \tilde{W}^t(L,\omega) - C_t i\omega \tilde{W}^t(L,\omega) + EI\tilde{W}^{t''''}(L,\omega) - T\tilde{W}^{t'}(L,\omega) \tag{4.20}$$

This set is solved similarly as was done for the eigenvalue problem. The assumed solution now reads as;

$$W^T(x,\omega) = C1e^{i\lambda_1 x} + C2e^{-i\lambda_2 x} + C3e^{\lambda_3 x} + C4e^{-\lambda_4 x} \tag{4.21}$$

with:

$$\lambda_1 = \beta; \quad \lambda_2 = -\beta; \quad \lambda_3 = i\beta; \quad \lambda_4 = -i\beta \tag{4.22}$$

$$\beta = \frac{T + \sqrt{T^2 + 4EI(\rho A + M_w)\omega^2}}{2EI} \tag{4.23}$$

The solution gives the dynamic response in the frequency domain. By applying the Inverse Fourier (Eq.2.3) the solution for $W^t(x,t)$ is found. For this the upper bound $\omega^+ = 30$ is used as this range contains the first four eigenfrequencies which should be sufficient.

To gain the displacement of the structure only ($W(x,t)$), one simply subtract the ground input motion. Subsequently, The bending moment $M(x,t)$ and shear force $V(x,t)$ can be found using the relative displacement of the structure $W(x,t)$ and by using;

$$M(x,t) = -EI\frac{\partial^2 W(x,t)}{\partial x^2} \tag{4.24}$$

$$V(x,t) = \frac{\partial M(x,t)}{\partial x} = -EI\frac{\partial^3 W(x,t)}{\partial x^3} \tag{4.25}$$

The results of this analysis are shown in the figures on the next page. Here the displacement at tunnel element $(x = L)$ and the bending moment and shear force at the bed $(x = 0)$ are shown. The total analysis (performed in Maple) is shown in appendix B.

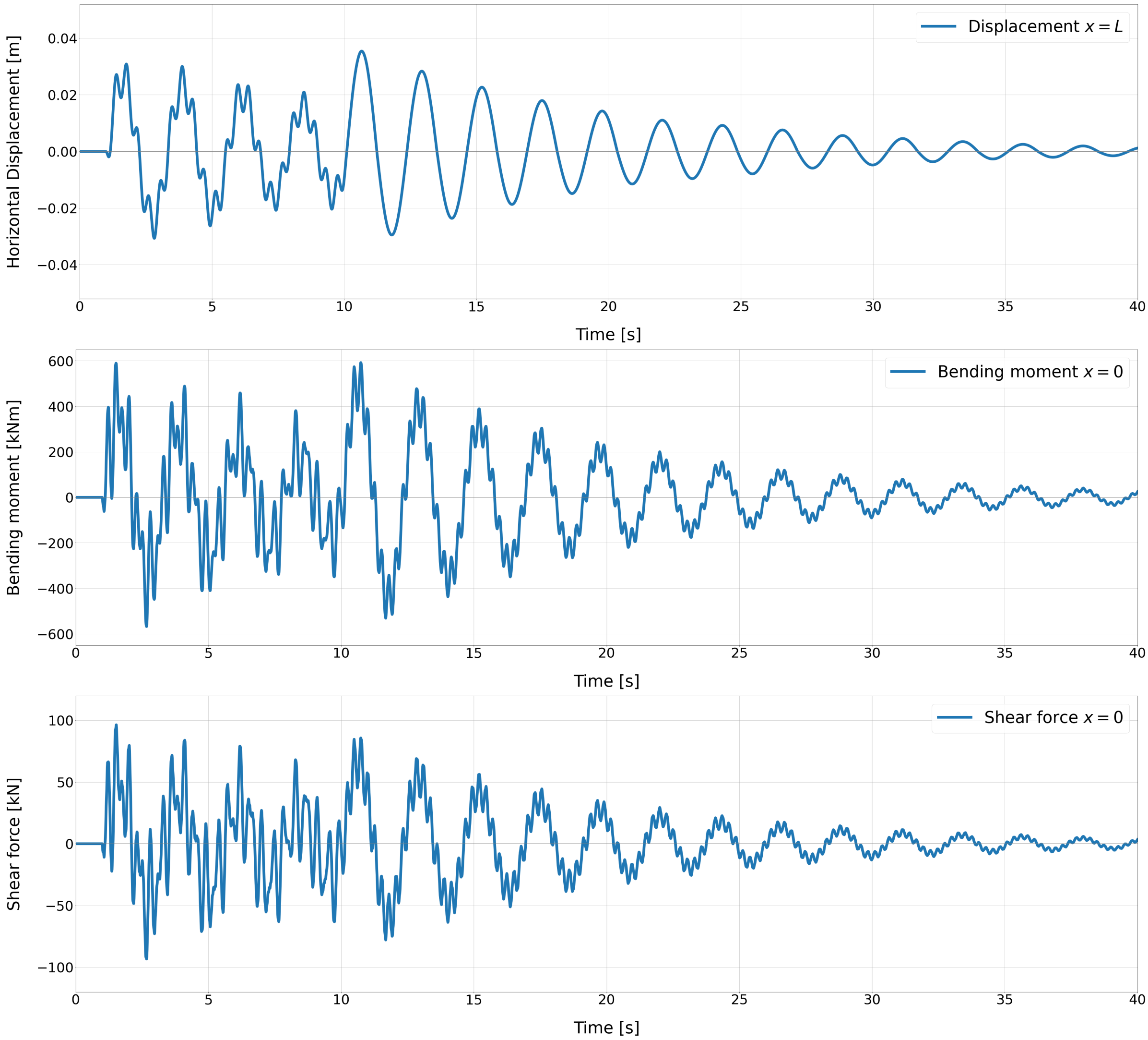

Figure 4.6: Results singular tether study

4.5. Finite Element analysis

To perform the finite element analysis, DIANA FEA (version 10.4) [10] will be used. In here a time history analysis with the same input signal is applied to check if both the frequency domain analysis and the FEA are performed correctly. The inputs for this model will be explained in this section.

4.5.1. Geometry

All the elements are modeled in a 3D environment where for now, only 2 beam elements are used. One which represent the tether and one which represents the tunnel element. For these beam elements, the element class Class-I Beams 3D is used. These class-I beams (element type L12BE) are based on the Bernouli beam theory, the degrees of freedom (DOFs) are shown in figure 4.8 where u_i is translational and ϕ_i is rotational. The length of the beam element which represents the tunnel (the horizontal beam in the figure below) is $100\ m$ which corresponds to the given spacing of the tethers. For the length of the tether a value of $L = 30\ m$ is applied. All other dimensions of both elements are as defined in chapter 3.

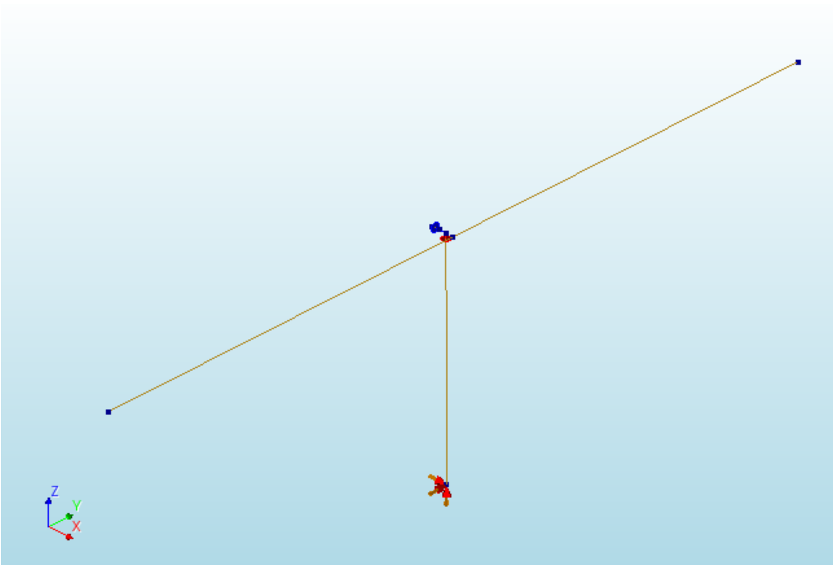

Figure 4.7: model singular tether Diana FEA

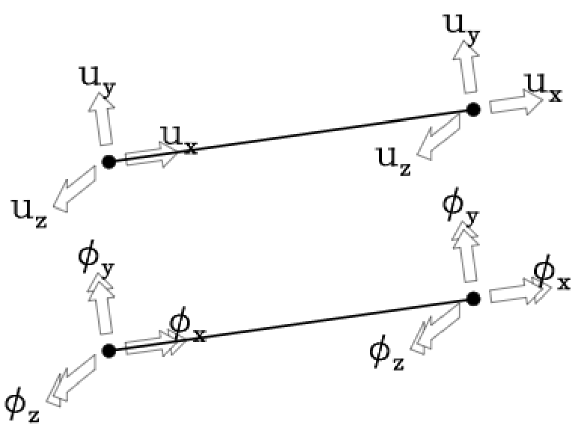

Figure 4.8: DOF class-I beam [10]

4.5.2. Material properties

The materials defined are for the tunnel element and the tether. Both consist of only linear properties in where the Young's modulus, Poisson's ratio (zero for both) and mass density are required. For the tunnel and tethers, the same value for the Young's modulus as in chapter 3 is used but the mass density has been adjusted. This is due to the added mass resulting from the hydraulic forcing. The input values for this mass density have been defined by using equation 4.26. Another adjustment is that a Rayleigh damping has been included for both the tether and tunnel material. This is to provide the effect of damping resulting from the hydraulic forcing. This effect could also be modeled with the use of boundary springs which provide a dashpot at each node. For a singular tether, this would be applicable but when analyzing the entire tunnel length, all these nodes would lead to a lot of elements which affects the computation time drastically. By using Rayleigh damping the amount of required elements is highly reduced. This damping is defined as Eq.4.27. Normally the values for α and β result from the eigenfrequencies of the system but in this case the damping is applied to mimic the effect of the dashpots. Whereas the value of these dashpots is known (the value of C_w for the tether and C_t for the tunnel), a value for α can be determined for which the desires damping value (given that β will be taken as zero) is obtained. This resulting Rayleigh damping now only consists of the damping due to the hydraulic forcing, structural damping isn't accounted for. An overview of all the numerical values for each parameter is given in table 4.1.

$$\text{Mass density tether/tunnel} = \frac{\rho A + M_w}{A} \tag{4.26}$$

$$C = \alpha M + \beta K \tag{4.27}$$

Table 4.1: Material properties FEA analysis singular tether

	Tether element	**Tunnel element**
Young's modulus $[N/m^2]$	2e+11	3.2e+10
Poisson's ratio [-]	0	0
Mass density $[kg/m^3]$	12217	5507
Rayleigh damping [-]	$\alpha = 0.08 \quad \beta = 0$	$\alpha = 0.01 \quad \beta = 0$

4.5.3. Supports and loads

Multiple supports have been added to the model. First those of the tether. At the bed, the tether is fully clamped. Therefore, a support is added where all three directions of translations and rotations are fixed. As for the tunnel, since a seismic loading in only the x-direction will be applied the translations in the other horizontal direction can be fixed. Hence, supports on the edge of the tunnel elements have been added supporting the tunnel in the y-direction.

As for the loads, two different cases have been added. The first regards the tensile load defined as T in chapter 3. For this analysis, this load has been applied as a regular load point in z-direction which has been applied on the topmost node of the tether. The other load case includes the seismic excitation. This has been added as a base excitation for which a uniform translational acceleration of $1\ m/s^2$ in the x-direction is used. Subsequently, a time-dependent factor has been applied for the load combination in which this seismic excitation is included. This time-dependent factor is based on the input motion as defined previously (Eq.4.15) but where previously the ground displacement was required, now the ground acceleration is and so the second time derivative of function 4.15 is used for which the resulting ground acceleration reads as follows;

$$\ddot{u}_g(t) = \begin{cases} -\sin(10t) & 1 \leq t < 10 \\ 0 & t < 1 \ \& \ t \geq 10 \end{cases} \tag{4.28}$$

4.5.4. Connections and tyings

The tunnel element and the upper end of the tether have some spacing in between and so aren't connected yet. To do so, a tying is added between these two elements. This element requires a master node (tether) and a slave node (tunnel element). Next, the tying is set so that the tunnel element and the tether have equal translations in the x-direction.

The final element to add is the mooring line attached to the tunnel element. To do so, a dummy element is added to the model. This dummy element consists of a small Class-I beam element perpendicular to the tunnel element and set on a distance of $1\ m$ from the upper node of the tether. This dummy element is supported fully fixed over its total length and with an extremely large Young's modulus and mass density is assumed completely rigid. Next, a spring element is added between the upper node of the tether and this dummy element. This spring is provided with a value for spring stiffness as defined previously. The figure below shows how the dummy element is implemented in the model with the tether (1), tunnel element (2), dummy element (3) and the spring connection (4).

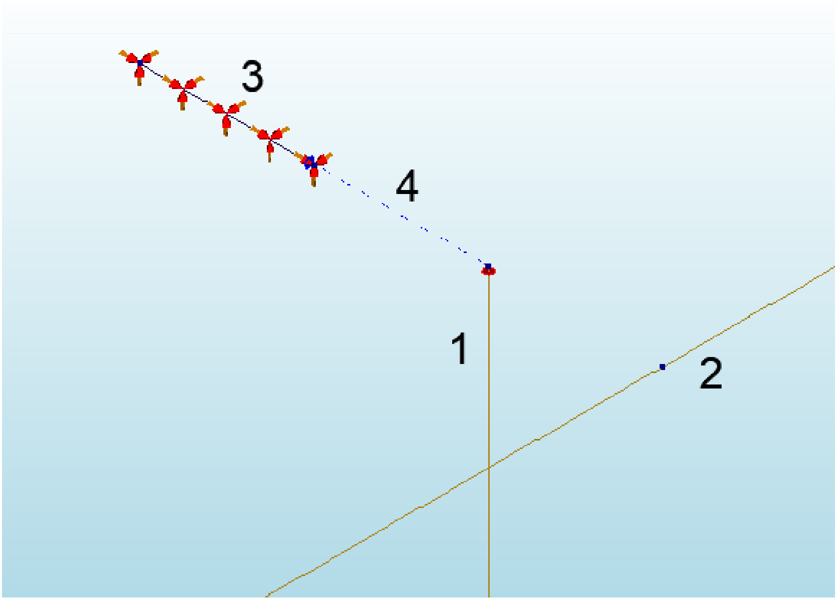

Figure 4.9: Dummy configuration Diana

4.5.5. Meshing

Before performing the analysis, the system needs to have a discrete element mesh. For this, a default mesher type is used. All elements meshed to elements with each a length of 1 m.

4.5.6. Analysis procedure

This analysis includes two parts. An eigenvalue analysis and a time history analysis. The first one is to check if the eigenperiods match those found in the previously performed eigenvalue problem, the second is to compute the effect of the sinusoidal ground excitation.

To include the effect of the tensile force T in the eigenvalue analysis, the properties of the free vibration need to be defined. Here a stiffness matrix is defined by calculating the linear elastic field resulting from the tensile force load set. If this isn't done, the tensile force would have been evaluated as just an external loading and would be excluded from the eigenvalue analysis. With this done, the eigenvalue analysis is performed. For this, the Implicitly restarted Arnoldi method is applied for which the first four eigenfrequencies are asked for.

For the time history analysis, a structural nonlinear analysis is applied in DIANA. For the time integration, the Newmark method [23] is applied with a beta value of $\beta = 0.25$ and a gamma value of $\gamma = 0.5$. Also, the dynamic effects are added in where a consistent mass matrix and damping matrix are applied. As the initial stress due to the tensile force was needed for the eigenvalue analysis, the same is required for the time history analysis. This is done by introducing a start step in the analysis. As was done for the eigenvalue analysis, again initial stresses are introduced to the calculations by calculating the linear elastic field resulting from the tensile force. This way, the tension force applied at the top causes tension throughout the whole tether from $t = 0$ until the end of the computation. Next, a time step is chosen in which the time steps and iteration methods are provided. For the time steps a value 0.01 second is used for 4000 steps, providing an output from $t = 0$ s till $t = 40$ s. For the iteration method, the Newton-Raphson method [13] is applied. The output asked for is the global displacement (relative to base), the bending moment and shear forces.

4.6. Results FEA and comparison

The results of the FEA analyses are shown here. Firstly, the results from the eigenvalue analysis. The four figures below show the first four eigenperiods with corresponding eigenmodes of the model. The provided periods in the figures are in Hertz. Table 4.2 provides an overview of the eigenfrequencies found in both analyses. The table shows that both eigenfrequency analyses result in the same eigenfrequencies and so are assumed to be correct.

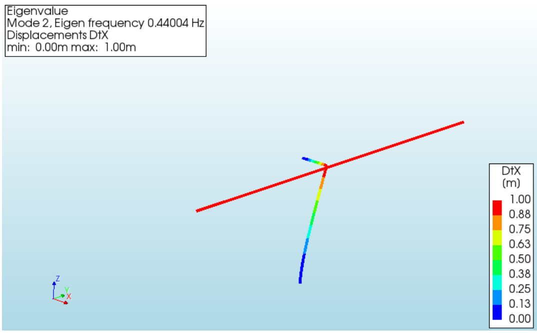

(a) First eigenmode $T_1 = 0.44$ Hz

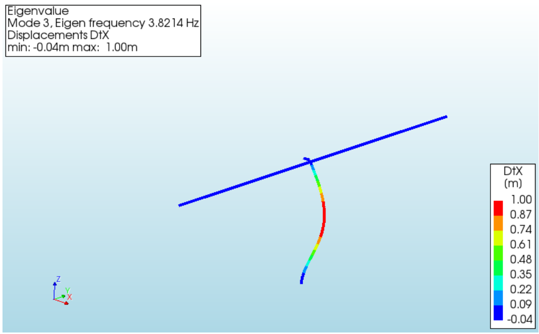

(b) Second eigenmode $T_2 = 3.82$ Hz

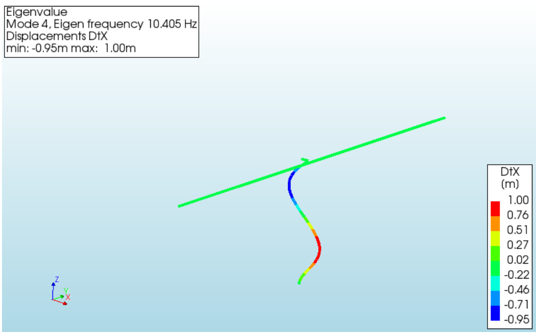

(c) Third eigenmode $T_3 = 10.40$ Hz

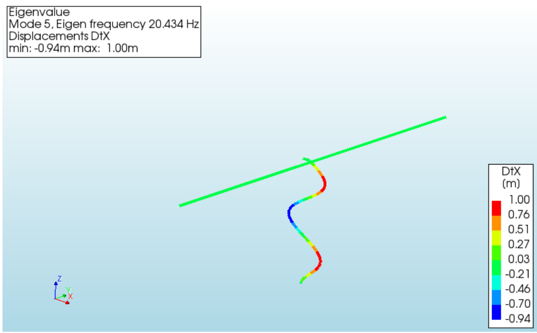

(d) Fourth eigenmode $T_4 = 24.43$ Hz

Figure 4.10: Results eigenvalue analysis Diana

Table 4.2: Comparison Eigenfrequencies

Eigenfrequency	Maple	Diana
ω_1	0.44 Hz	0.44 Hz
ω_2	3.82 Hz	3.82 Hz
ω_3	10.42 Hz	10.41 Hz
ω_4	20.49 Hz	20.43 Hz

Next the results of both seismic analyses. The figures on the next page show the results of both the frequency domain analysis performed in Maple and the results from the time history analysis performed in DIANA. The same outcomes have been plotted as previously (figure 4.6), namely, the displacement at the top end and the bending moment and shear force at the bed. The results of both analyses are shown in figure 4.11. Again, similar results are obtained for both analyses. The resulting bending moment and shear force of the maple analysis are a bit more 'shaky' which is due to numerical errors in the differentiation of the displacement.

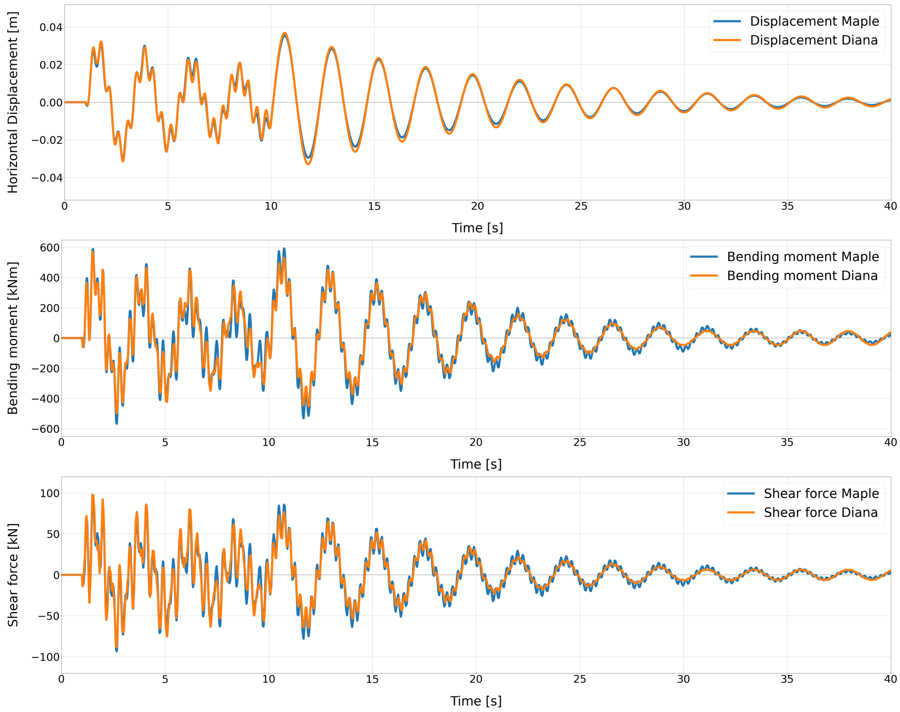

Figure 4.11: Comparison of results Maple and Diana

Effect on tensile force

To see whether the horizontal ground excitation has an effect on the tension force of the vertical tethers, the resulting normal force N_z from the FEA model at $x = L$ is shown below. It shows that the initial normal force equals the tensile force T as a result of the buoyancy force which is as expected. Next, the effect of the input motion becomes visible as this normal force starts to oscillate although this oscillation is very limited as the quantity hardly changes.

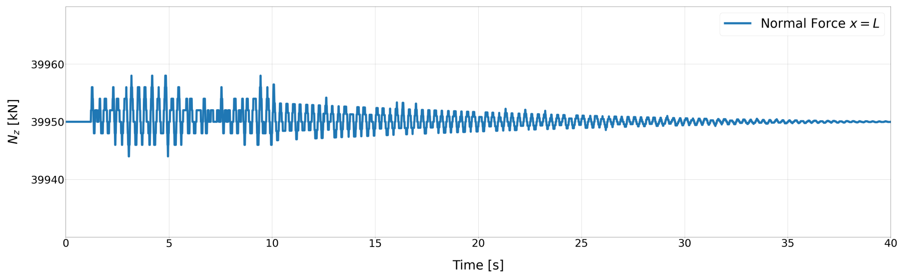

Figure 4.12: Normal force tether at $x = L$

4.7. Conclusion

Based on the comparison of the results, it seems fair to conclude that the Maple model is correctly solved and that the FEA model is sufficiently accurate. With this check, the rest of the model can be built in which the entire tunnel span, all tethers and mooring lines and the connections with the land tunnel are included. It's good to notice that some aspects may be missing such as structural damping. This damping is mostly included by the use of Rayleigh damping which has now been used to generate the damping caused by the hydrodynamic forcing. Excluding this damping results in larger forcing in the structure and so this model made for this study will give an overestimation compared with a model including the structural damping.

5

Total Tunnel Study

This chapter introduces the total analysis of the SFT. In DIANA, all the tethers, mooring lines and tunnel sections are modeled by the use of the previously described case study. Next, the total model will be tested on multiple seismic inputs. These input signals will be scaled by the use of prescribed spectra with the purpose of obtaining more general input signals. With the use of this model and the different input motions, multiple time-history analyses will be performed for gaining knowledge about the seismic response of the SFT.

5.1. Model description

With the use of the model made in the previous chapter, a model of the entire tunnel is made. This model now consists of the total tunnel length with all the tethers and mooring lines as described in chapter 3 and the inclusion of the land connections. The described bathymetry will be used to obtain the different lengths of the tethers and mooring lines and of the overall length of the tunnel itself. Most of the input for this model is the same as in the previous chapter. Aspects that differ from the previous will be explained in this section.

5.1.1. Tunnel geometry and supports

Whereas in the previous analysis, the tunnel only contributes as a point mass at the boundary condition, now the tunnel itself will be evaluated as well. This asks for more input concerning the geometry. Therefore, in this analysis, the tunnel elements will be provided by a more detailed cross-section in where the different moments of inertia will be described as well. These moments of inertia are derived by the use of Steiner's parallel axis theorem [1] which provides the following equations.

$$I_{\bar{x}\bar{x}} = I_{xx} + \bar{x}_c^2 A \tag{5.1}$$

$$I_{\bar{x}\bar{z}} = I_{xz} + \bar{x}_c \bar{z}_c A \tag{5.2}$$

$$I_{\bar{z}\bar{z}} = I_{zz} + \bar{z}_c^2 A \tag{5.3}$$

The subscript in the above given expressions indicates the moments of inertia for the different coordinate systems. $\bar{x}_c$ and $\bar{x}_c$ indicate the distance in x and z-direction from the center of the coordinate system. The moments of inertia I_{xx} and I_{zz} give the regular moment of inertia for the shape itself. A is the cross-sectional area.

The cross section as given in section 3.2.1 will be slightly simplified to easily obtain the moments of inertia. For the analyses made here they will be evaluated as two annuluses (region between two concentric circles) with both a diameter of 17.5 m and a thickness of 1.60 m. The annuluses have a centre-to-centre distance of 30 m.

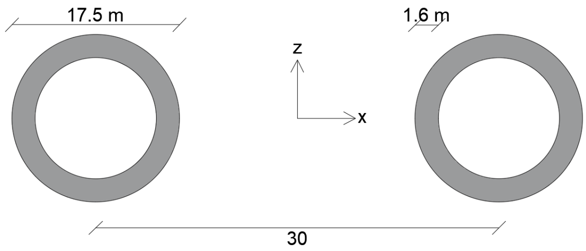

Figure 5.1: Evaluation cross-section

For a single annulus, the following moments of inertia are given.

$$I_{xx} = I_{zz} = \frac{1}{4}\pi\left(R_u^4 - R_i^4\right) \tag{5.4}$$

$$I_{xz} = 0 \tag{5.5}$$

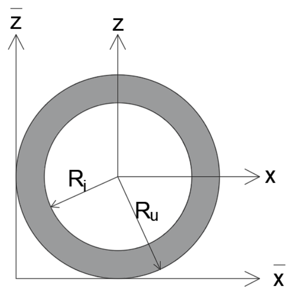

Figure 5.2: Coordinate system annulus

Based on this the following moments of inertia for the given cross-section are found:

$$I_{\bar{x}\bar{x}} = 41067.4 \text{ m}^4 \tag{5.6}$$

$$I_{\bar{x}\bar{z}} = 0 \text{ m}^4 \tag{5.7}$$

$$I_{\bar{z}\bar{z}} = 5102 \text{ m}^4 \tag{5.8}$$

Another difference are the supports of the tunnel. In the previous chapter, the full length of the tunnel has been supported in y-direction since the outer ends of the tunnel were not connected to anything. In this analysis, the tunnel will be supported by the tethers which can be seen as intermediate support, buoyancy force (defined in the next section) and supports will be added at the outer end of the tunnel element. These last supports represent the connection with the land tunnel and are for now assumed to be fully fixed. The connections of the tethers and the tunnel elements will, as was done previously, be realized by the use of tyings. Figure 5.3 shows the geometry of the model used in this chapter.

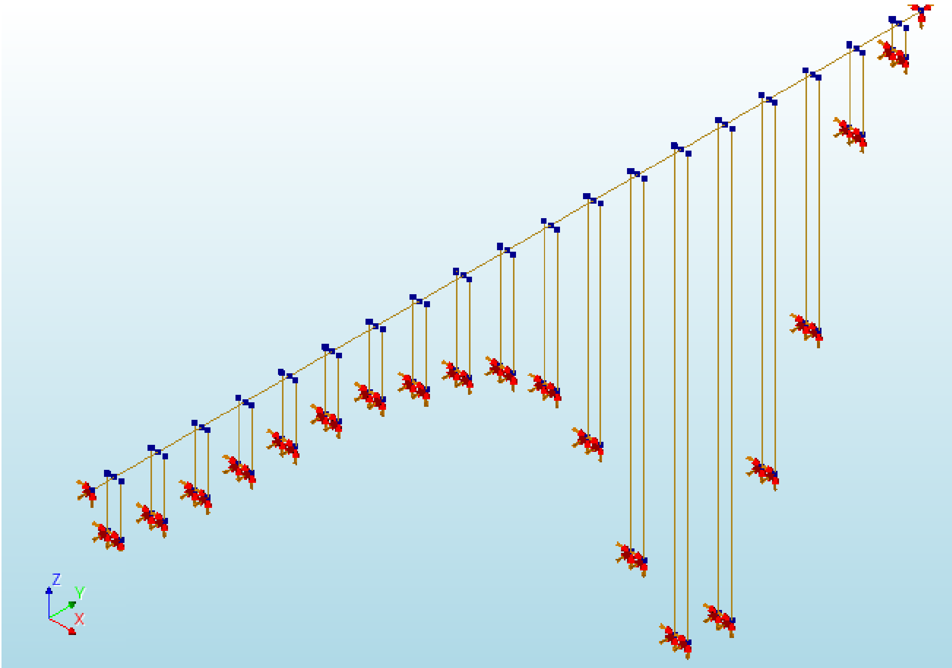

Figure 5.3: Geometry of the total model

5.1.2. loads

As mentioned in the previous subsection, the vertical support of the tunnel will be (among other things) replaced by a load. Two vertical line loads are added which represent the buoyancy force (upwards) and the self-weight of the tunnel (downwards). The values of these forces are as described in section 3.2.1. The seismic forces shall be applied differently as well. In the previous analysis, the seismic input was applied in the x-direction (transverse direction). In reality, the input motion may come from any angle which results in a different forcing on the tunnel. Hence, in this analysis, not only a transverse input motion is applied but also a longitudinal input motion (y-direction). Section 5.7.1 provides more context on the different angles of attack. The tensile force remains unchanged.

By applying the line loads on the tunnel elements, an initial moment distribution and so initial stresses are introduced. Normally these would also give an initial extension of the tethers but this would not comply with reality. The next subsection clarifies this.

5.1.3. Analysis procedure

The time-history analysis performed for the analyses made in this chapter will consist of different phases. As mentioned in the previous subsection, the use of the different line loads on the tunnel element would cause an initial extension of the tethers. In reality, this extension would happen and would be the reason for the tension force in the tethers. Hence, the tensile force, which is already applied on the tethers would be the result of the resulting upwards force and the extension. By applying the tensile force and allowing the extension of the tethers, the effect of the resulting force would be applied twice. To prevent this, three phases are added before starting with the time steps to gain the correct initial conditions. The first phase uses the tether geometry only and does not include the tunnel at all. The tensile force is applied to each tether to gain the correct tension stress in each element. The second phase starts by removing all displacements from the previous phase but keeping the stresses. This way, each tether remains under tension but keeps its original length with no extension. Next, still in the second phase, the tunnel elements are added with the supports and the outer ends and with the buoyancy force and self-weight which give the moment distribution over the tunnel elements. In the final phase, the resulting displacements are again removed. This results in the complete tunnel with initial tension stresses in the tethers and moment distribution along the tunnel but with zero initial displacements. With these initial conditions, the time-history analysis can be applied as was done in the previous analysis.

5.2. Seismic inputs

For the analysis made in chapter 4, a simple sinusoidal input motion was used to keep the computations made in Maple accessible. As this may provide a dynamic response, the input motion is far from realistic when designing for seismic excitations. Hence, for the analysis made in this chapter, more realistic input motions will be used.

Eurocode 8 part 1 [11] describes the criteria which should be met when representing the seismic action with the use of a time-history representation. Here, a distinction is made between artificial accelerograms and recorded or simulated accelerograms. The latter are used when the seismic features of the site are known. Since the case study for this study isn't linked to any geographical location, these are not known and so artificial accelerograms will be used for this analysis.

These artificial accelerograms are generated by scaling the accelerograms of other seismic events to the spectra described by Eurocode (with a 5% damping). For control design, the criteria (which will be clarified later) should be evaluated for at least three different seismic records. The three records used for this study are (1) El Centro, California during the California earthquake of 18 May 1940 with a magnitude of 7.1; (2) Gebze, Turkey during the Kocaeli earthquake of 17 august 1990 with a magnitude of 5.8; (3) Mexico City which occurred at 19 September 1985 (magnitude 8.1). The accelerograms of each earthquake are shown in figure 5.4. The response spectra of the three signals are shown in figure 5.5 on the next page. Each signal was obtained from the online database provided by CESMD [8].

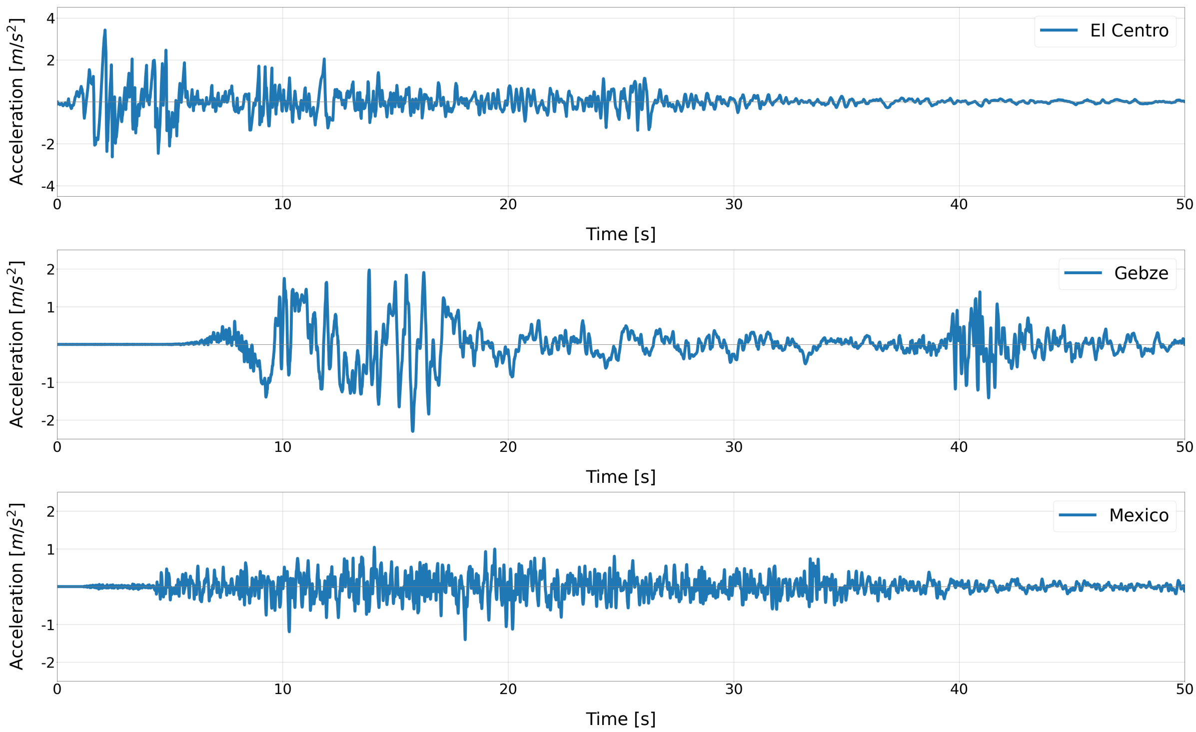

Figure 5.4: Original input signals

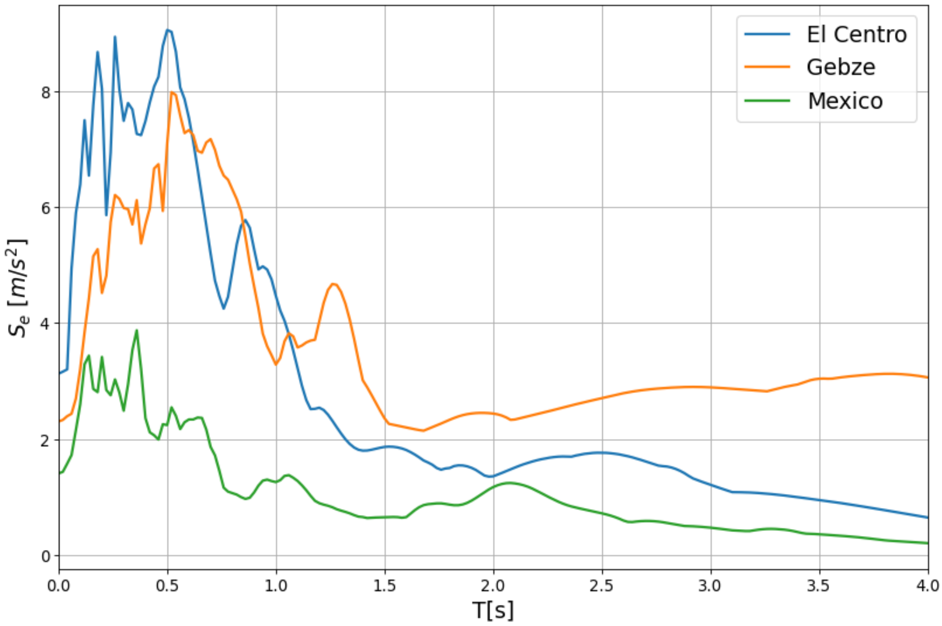

Figure 5.5: Response spectra of input signals

As stated previously, each input signal should be scaled such that the response spectrum of each signal matches the spectra provided by Eurocode. To do so, the latter needs to be defined. For a horizontal elastic acceleration response spectrum Eurocode provides the following expressions:

$$0 \leq T \leq T_B: \qquad S_e(T) = a_g \cdot S \cdot \left[1 + \frac{T}{T_B} \cdot (\eta \cdot 2.5 - 1)\right] \tag{5.9}$$

$$T_B \leq T \leq T_C: \qquad S_e(T) = a_g \cdot S \cdot \eta \cdot 2.5 \tag{5.10}$$

$$T_C \leq T \leq T_D: \qquad S_e(T) = a_g \cdot S \cdot \eta \cdot 2.5 \left[\frac{T_C}{T}\right] \tag{5.11}$$

$$T_D \leq T \leq 4: \qquad S_e(T) = a_g \cdot S \cdot \eta \cdot 2.5 \left[\frac{T_C T_D}{T^2}\right] \tag{5.12}$$

Where:

$S_e(T)$ = Elastic response spectrum;
T = Vibration period of a linear single-degree-of-freedom system;
a_g = Design ground acceleration $(a_g = \gamma_1 a_{gR})$;
T_B = Lower limit of the period of the constant spectral acceleration branch;
T_C = Upper limit of the period of the constant spectral acceleration branch;
T_D = Value defining the beginning of the constant spectral acceleration branch;
S = soil factor
η = damping correction factor given by Eq.5.13

$$\eta = \sqrt{\frac{10}{5 + \xi}} \geq 0.55 \tag{5.13}$$

In order to define the different parameters, firstly, Eurocode distinguish two types of elastic response spectra. Type 1 for magnitudes greater than 5.5 and type 2 for magnitudes less than 5.5. As all previous given signals have a magnitude greater than 5.5, type 1 will be used for which the following values are provided;

Table 5.1: Values of parameters Type 1 horizontal elastic response spectra

Ground Type	S	$T_B(s)$	$T_C(s)$	$T_D(s)$
A	1.0	0.15	0.40	2.0
B	1.2	0.15	0.50	2.0
C	1.15	0.20	0.60	2.0
D	1.35	0.20	0.80	2.0
E	1.4	0.15	0.50	2.0

Considering the ground types given in the table above, Eurocode characterizes the different types going from hard rock-like formations (A) to the softer and cohesionless soil formations. As described in chapter 3, the ground has already been classified as type A. Therefore, these values will be applied for the spectrum. For the damping, Eurocode states that each input signal should be scaled to a spectrum with a damping of 5% ($\xi = 5\%$) resulting in $\eta = 1$.

Finally the design ground acceleration a_g which is defined as $a_g = a_{gR} \cdot \gamma_I$. Here a_{gR} is the reference peak ground acceleration and γ_I the importance class. The latter depends on the type of structure. To define a value for this parameter, Eurocode classified different structures as shown in table 5.2. As a tunnel can be of large importance in providing supplies for a certain area and failure during usage could be highly catastrophic, importance class IV will be used.

Table 5.2: Importance classes for buildings by Eurocode 8 [11]

Importance class	Buildings	Importance factor γ_I
I	Buildings of minor importance for public safety, e.g. agricultural buildings, etc.	0.8
II	Ordinary buildings, not belonging in the other categories	1.0
III	Buildings whose seismic resistance if of importance in view of the consequences associated with a collapse, e.g. schools, assembly halls, cultural institutions etc.	1.2
IV	Buildings whose integrity during earthquakes is of vital importance for civil protection, e.g. hospitals, fire stations, power plants, etc.	1.4

The reference peak ground acceleration (a_{gR}) (PGA) would normally be obtained form the Global Seismic Hazard Map [21]. This map gives a design peak ground acceleration for the different seismic zones for the entire planet . This value corresponds to a 10% probability of exceedance in 50 years, P_{NCR}, of the seismic action for which the structure should be able to withstand without local or global collapse. The peak ground acceleration in this map ranges from $0.2g$ (light green) up to roughly $0.5g$ (brown). Whereas these brown areas with the extreme high design PGA's are scarce, most seismic vulnerable regions are assigned with a PGA of around $0.3g$. As this is a more common value, a PGA of $0.3g$ will be used for this study.

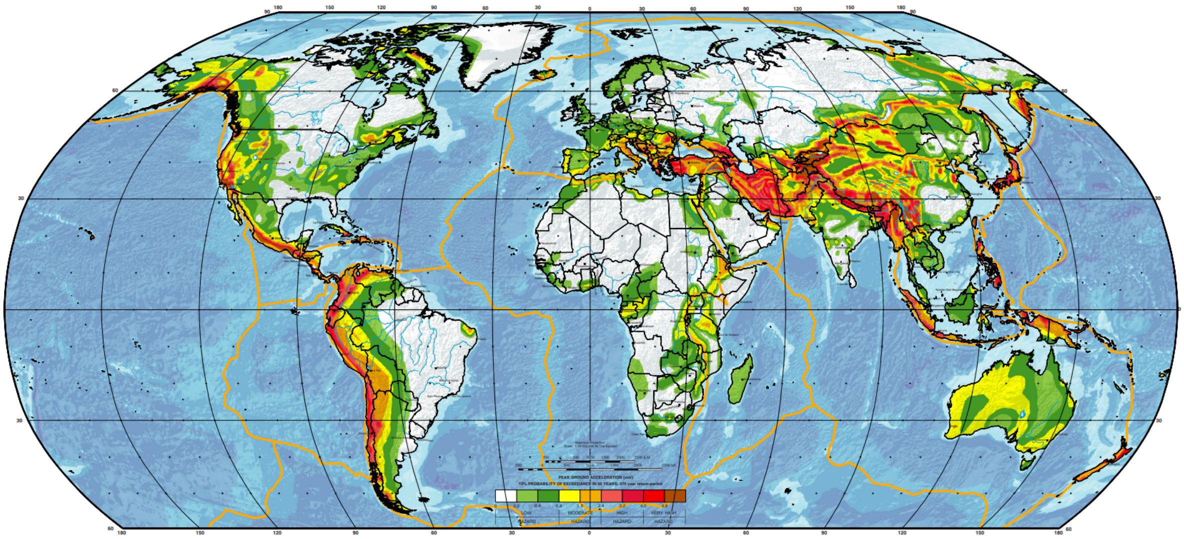

Figure 5.6: Global seismic hazard map with a peak ground acceleration with 10% probability of exceedance in 50 years [21]

The spectrum resulting from the previously chosen values is shown in figure 5.7. In the same plot the response spectrum of the three different input signal as in figure 5.5 have been plotted as well.

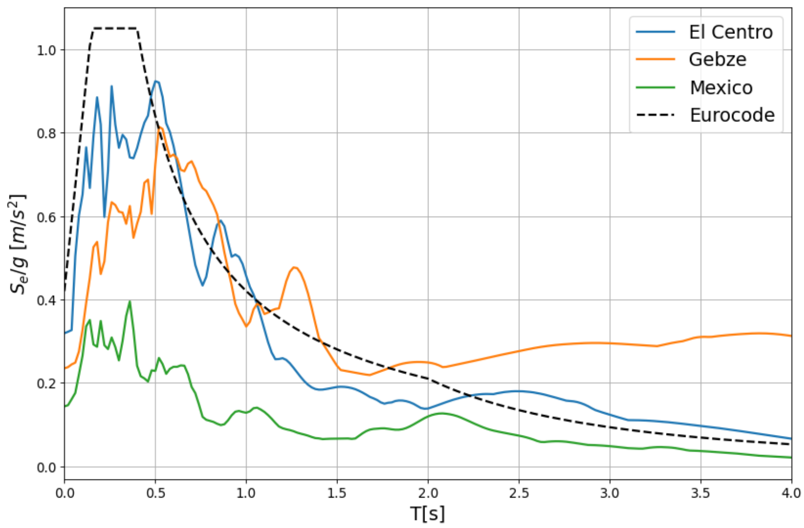

Figure 5.7: Type 1 elastic response spectrum for ground type A (5% damping) along with the input spectra

The next step is to scale the three spectra such that they match the spectra derived from Eurocode. This is done by the use of the software Seismosoft [26] with which an input accelerogram can be matched with a prescribed target response spectrum using the wavelets algorithm proposed by Abrahamoson (1992) [2] and Hancock et al. (2006) [15] or the algorithm proposed by Al Atik and Abrahamson (2010) [5].

Figure 5.8 below shows the resulting spectra obtained by this scaling. Figure 5.9 show the resulting accelerograms.

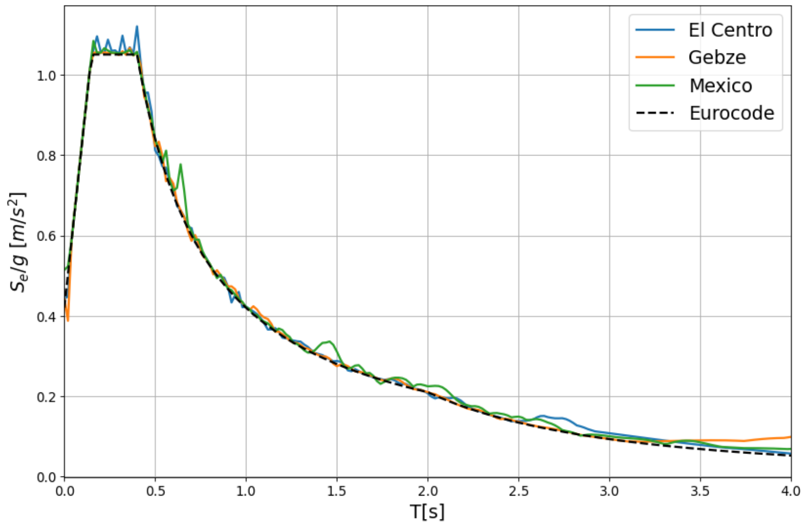

Figure 5.8: Scaled input spectra

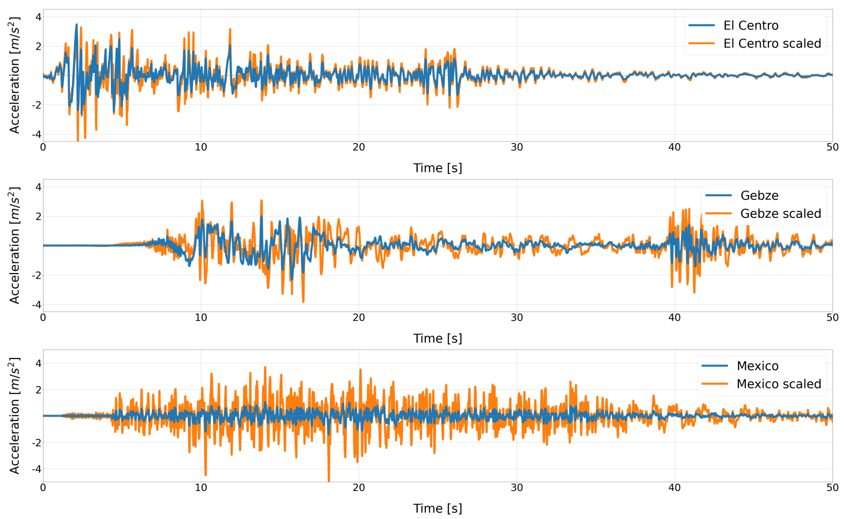

Figure 5.9: Scaled input signals

Now that each signal has been scaled to the prescribed spectrum, all three of them are now highly similar in energy content per frequency. This doesn't mean that the three signals are now close to identical. All three of them still differ in duration and epicentral distance and so when performing the time-history analyses, applying the three scaled signals does not have to result in identical results.

5.3. Design Criteria

The design criteria for the SFT may be based on the Serviceability limit state (SLS) or the Ultimate limit state (ULS). The SLS is more based on e.g. the maximum allowed deformations for comfortable usage and acceptable cracking of the concrete where the ULS criteria only evaluate collapse or not. Earthquakes may cause failure mechanisms of the SFT on different levels, where small excitations may eventually lead to loss of water tightness and larger may result in direct collapse. For this study, only the ULS will be used for the criteria in which the maximum occurring loads during the seismic attack are compared with the bearing capacity of the different elements. For the concrete tunnel elements, tensional stresses are expected to be more critical than compressive as the tensile capacity is much lower and so this quantity will be checked throughout the different analyses.

Normally the tensile strength of concrete is around $2-5$ MPa [28] but in studies done by J.M.Rapheal 1984 [25] it was found that the apparent tensile strength for concrete under seismic loading can be larger as the loading is of a short duration. In here the tensile strength under seismic loading is expressed as Eq.5.14.

$$f_t = 3.4 f_c^{2/3} \tag{5.14}$$

Where f_c is the compressive strength of concrete in kg/cm^2 which is mostly taken as 20 N/mm^2 $\approx$ 204 kg/cm^2. Applying Eq.5.14 provides a tensile strength of $f_t = 118$ kg/cm^2 ≈ 11.5 N/mm^2. This value will be used as the upper limit of the allowed tensile stress in the tunnel elements.

The other criteria formed for this analysis considers the tension in the tethers. As explained previously, an initial tension stress of 200 N/mm^2, which results from the buoyancy force on the tunnel elements, is already applied. Tension must remain in these elements as a lowering would eventually cause slack which should always be avoided. Therefore, one criterion of the tethers should consider the minimum occurring tension in these elements. Besides a lower limit, an upper limit should be formed as well for the same reason as was done for the tunnel elements. The tensile strength of the steel tethers is taken as 420 MPA. Fatigue will for this study not be considered as the seismic events are of such short duration and only happen occasionally that the stress changes are assumed not problematic.

Table 5.3: Design criteria SFT

Element	description	Value
Tunnel	Maximum tensile stress must remain under tensile strength concrete (for seismic loading)	$\sigma_{tunnel,tension,max} < 11.5$ N/mm^2
Tether	Maximum tensile stress must remain under tensile strength tethers	$\sigma_{tether,tension,max} < 420$ N/mm^2
Tether	Tensile stress must never approach zero to prevent slack	$\sigma_{tether,tension,min} >> 0$ N/mm^2

5.4. Stresses Tunnel cross-section

When the time-history analysis is performed, bending moments and shear forces in the tunnel elements are obtained throughout the evaluated time range. To verify whether the defined design criteria for the tunnel elements are met, the stresses resulting from these bending moments and shear force should be expressed throughout the cross-section of the tunnel. To do so Eq.5.15 is used. With this expression, the resulting tensile stresses resulting from the normal force and bending moment in the x and z direction for the arbitrary point (x,z) in the cross-section can be obtained. The resulting stresses are tensile when $\sigma(x,z) < 0$.

$$\sigma(x,z) = \frac{N_y}{A} + \frac{M_x x}{I_{\bar{x}\bar{x}}} + \frac{M_z z}{I_{\bar{z}\bar{z}}} \tag{5.15}$$

The points of interest for these stresses are the outer most out boundaries of the cross section as these are the locations where the highest values are expected. Hence, six points will be evaluated which are shown in the figure below and for which the corresponding x and z values are given in table 5.4.

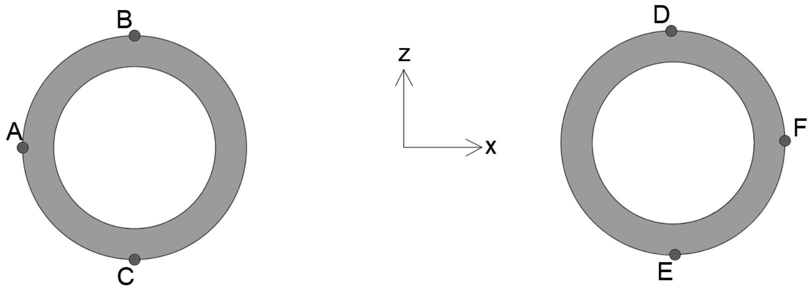

Figure 5.10: Point of interest for stress check in cross-section

Table 5.4: Coordinates check points in cross-section

Point	A	B	C	D	E	F
x [m]	-23.75	-15	-15	15	15	23.75
z [m]	0	8.75	-8.75	8.75	-8.75	0

This analysis is executed throughout the total tunnel length at each tether connection, land-tunnel connection, and halfway the span of each tether/tether-land-tunnel pair. Figure 5.11 visualises these points.

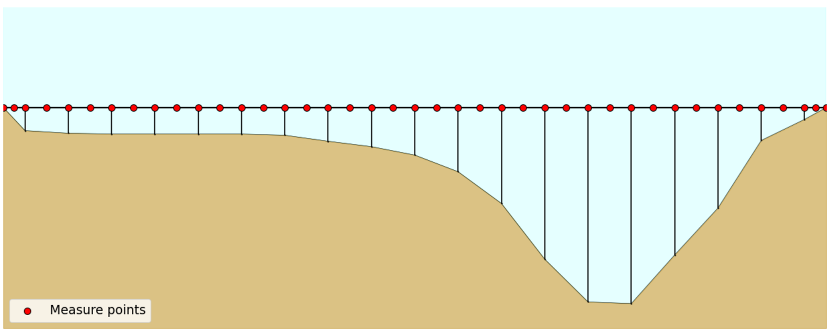

Figure 5.11: Measure points for tunnel stresses

As explained previously, the buoyancy force and the self-weight of the tunnel already introduce a stress development throughout the total tunnel span. Figure 5.12 shows the initial stresses. Here, only the maximum of the different stresses in the points A-F per cross-section is shown. Through these points, a curve is fitted to visualize the envelope of the stresses through the tunnel.

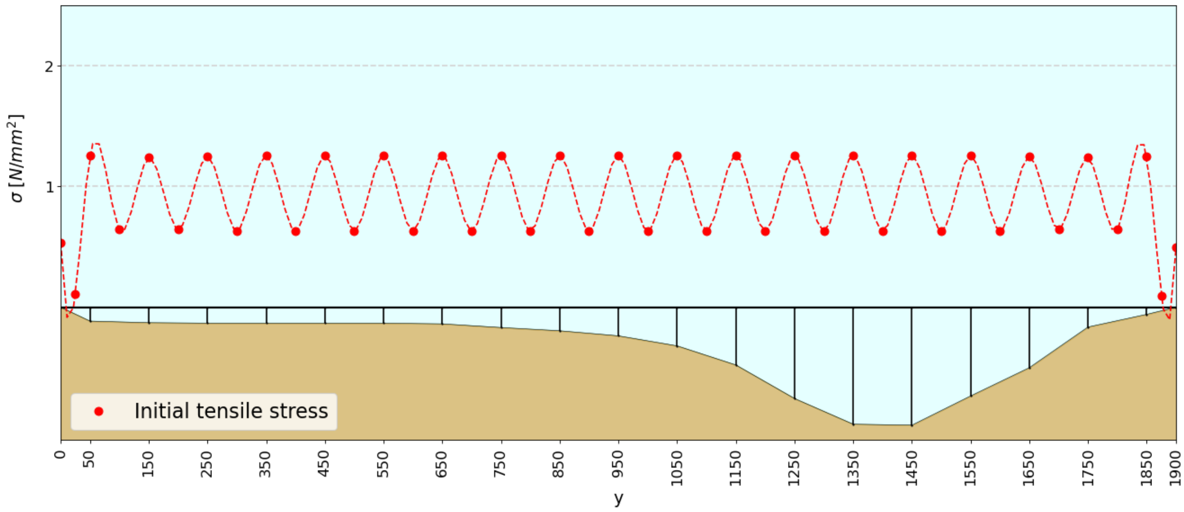

Figure 5.12: Initial maximum tensile stress tunnel elements

5.5. Results

This section provides the results of the different analyses performed on the total tunnel model. The results include the eigenvalues, tunnel tensile stresses, tether tensile stresses and the displacements of both tunnel and tethers.

5.5.1. Eigenvalue analysis

First the results of the eigenvalue analysis. Table 5.5 shows the results for the tethers where, for each, the first three eigenperiods are given along with the total length. Each tether has been given a number as well, this corresponds with its location with Tether 1 being the leftmost tether. In figure 5.13, the results of table 5.5 are shown as a scatter plot with on the x-axis the eigenperiod and on the y-axis the tether length. It shows a linear relation in where an increase of length results in an increase of the eigenperiod and so of the flexibility. As for the eigenperiods of the tunnel, table 5.6 provides these in where a distinction is made for the different deformation directions of the eigenmodes (see figure 5.14). For each direction of deformation, the first 5 eigenperiods of the tunnel are given.

Table 5.5: Eigenperiods of tethers

Element	Length [m]	T_1 [sec]	T_2 [sec]	T_3 [sec]
Tether 1	115	1.55	0.73	0.45
Tether 2	128	1.76	0.84	0.52
Tether 3	132	1.82	0.87	0.55
Tether 4	132	1.82	0.87	0.55
Tether 5	132	1.82	0.87	0.55
Tether 6	132	1.82	0.87	0.55
Tether 7	138	1.92	0.92	0.58
Tether 8	168	2.40	1.17	0.74
Tether 9	195	2.82	1.38	0.89
Tether 10	237	3.50	1.72	1.12
Tether 11	320	4.81	2.39	1.57
Tether 12	478	7.30	3.65	2.42
Tether 13	756	11.71	5.85	3.89
Tether 14	969	15.08	7.52	5.03
Tether 15	977	15.20	7.58	5.05
Tether 16	735	11.39	5.68	3.77
Tether 17	501	7.69	3.83	2.54
Tether 18	164	2.34	1.13	0.72
Tether 19	59	0.66	0.28	0.16

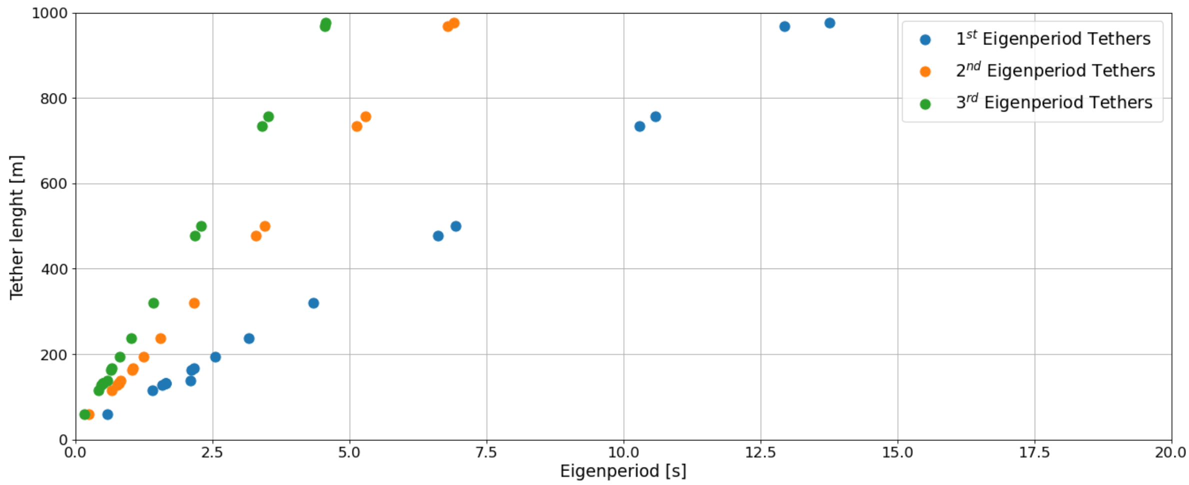

Figure 5.13: Eigenperiods tethers

Table 5.6: Eigenperiods tunnel

	T_1 [sec]	T_2 [sec]	T_3 [sec]	T_4 [sec]	T_5 [sec]
Transverse	17.28	8.72	4.76	2.93	1.98
Vertical	5.35	3.94	3.05	2.57	2.30
Longitudinal	1.58	0.79	0.53	0.39	0.32

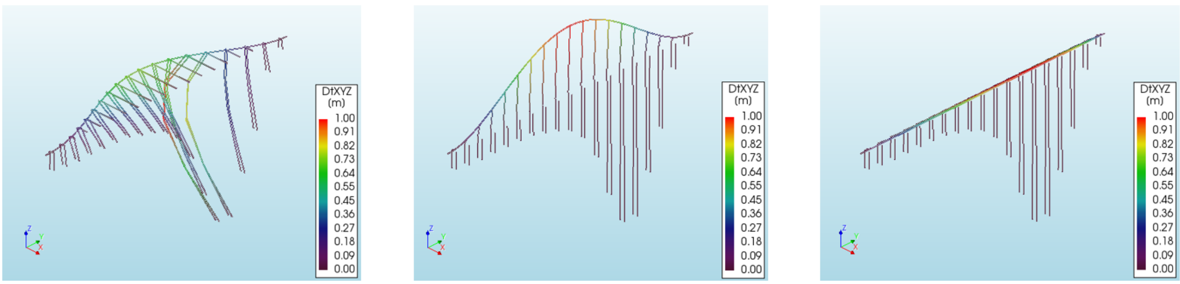

Figure 5.14: Horizontal (left), vertical (middle) and normal (right) fundamental eigenmode tunnel

Figure 5.15 shows the fundamental eigenperiods (T_1) of all tethers and of the tunnel plotted on the response spectra of the input signal (as provided in figure 5.8). Note that these spectra are only defined between $T = 0$ and $T = 4$. The spectra provide the response for each eigenperiod for the different input signals where the highest responses are found in the range of $T = 0.15 - 0.40$ seconds. From $T = 0.40$ up to $T = 2$, intermediate response values are found and after $T = 4$ second, response values are minimal. The figure shows that most of the eigenperiods are in the range of the intermediate and of the lower values of the spectra. This suggests that the response of each element would be limited as well.

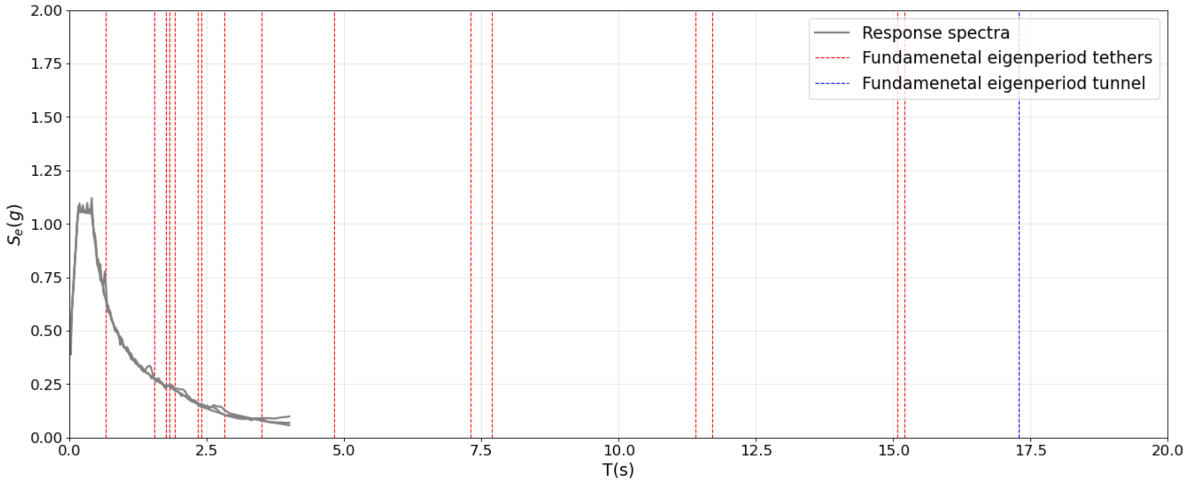

Figure 5.15: Fundamental eigenperiods on input spectra

5.5.2. Time-History analysis

Per signal, two time-history analyses have been executed. One in the transverse direction (x) and one in the longitudinal direction (y). Hence, in total six time-history analyses have been performed for this chapter. This section shows the resulting tensile stresses in the tunnel, tensile stresses in the tethers and, even though there are no criteria described for these, the displacements of the tunnel and tethers for each of these analyses. First the results for the input motions in the transverse direction, secondly, those for the input motion in the longitudinal direction are provided.

Transverse direction

Tunnel stresses

The top image in figure 5.16 shows the resulting tensile stresses in the tunnel cross-sections from the input motions in the transverse direction. Here the initial tensile stress envelop, along with those of the different input motions are shown. The red dashed horizontal line shows the upper limit of the allowed tensile stresses as defined in the design criteria. The bottom image in the figure presents the effect of the transverse input motion which is obtained by subtracting the initial state from the total results. Where the tensile stresses do show a significant increase in some nodes, the maximum remains still far below this upper limit which indicates that the tunnel remains safe from exceeding the tensile strength. Looking at the envelope of the tensile stresses, it is clear to see that the nodes at the connections with the land tunnel are the most affected by the seismic action. Based on this, it can be concluded that the seismic energy, transported through the tethers doesn't affect the tunnel elements much. As for the response of the tunnel. As was found previously the tunnel is rather flexible in the transverse direction. As the flexibility is high, the tunnel elements can deform easily which results in a lowering effect on the stresses. Would the tunnel be stiffer in the transversal direction, then larger stresses are expected along with lower transversal deformations.

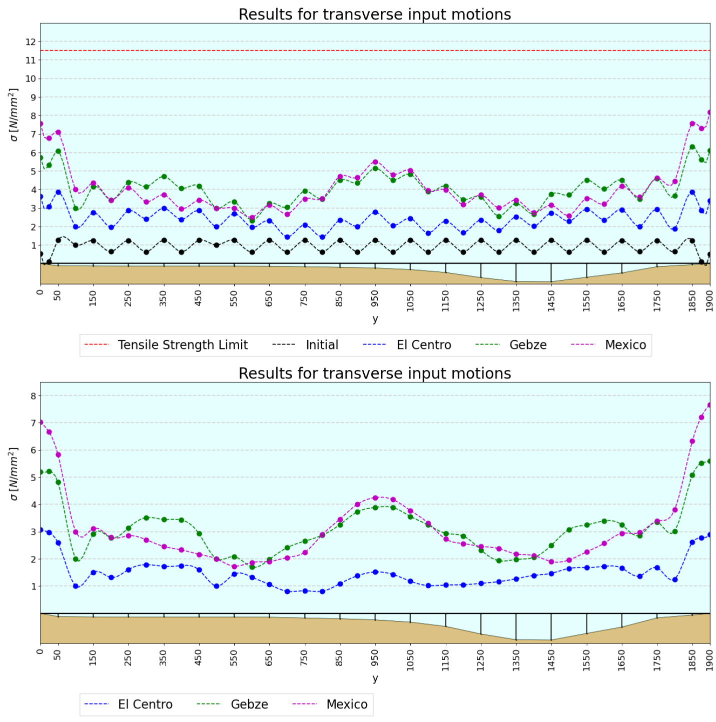

Figure 5.16: Resulting tensile stress due to transverse input motions (top) and the effect of transverse input motions (bot)

Figure 5.18 on the next page shows an overview of the different resulting forces in the tunnel (N_y, M_x & M_z) along with the different tensile stresses resulting from these forces (σ_{N_y},σ_{M_x} & σ_{M_z}) for a singular node in the model resulting from the El Centro signal. This overview shows that the resulting tensile stress is mostly formed from the tensile stress due to the bending moment M_z which has by far the largest contribution to the total. The resulting normal forces do not add up to the total tensile stress as only compressive stresses are found and the stresses due to bending moment M_x remain mostly around its initial level.

Tether stresses

Considering the tethers, the figures below show the minimum and maximum obtained tension stress in each tether. As the tethers are rather large flexibility, the horizontal input motions have a limited effect on these. This is also shown in the figure below where the stresses hardly change and the tethers keep their tensile stress around the initial state ($200\ N/mm^2$).

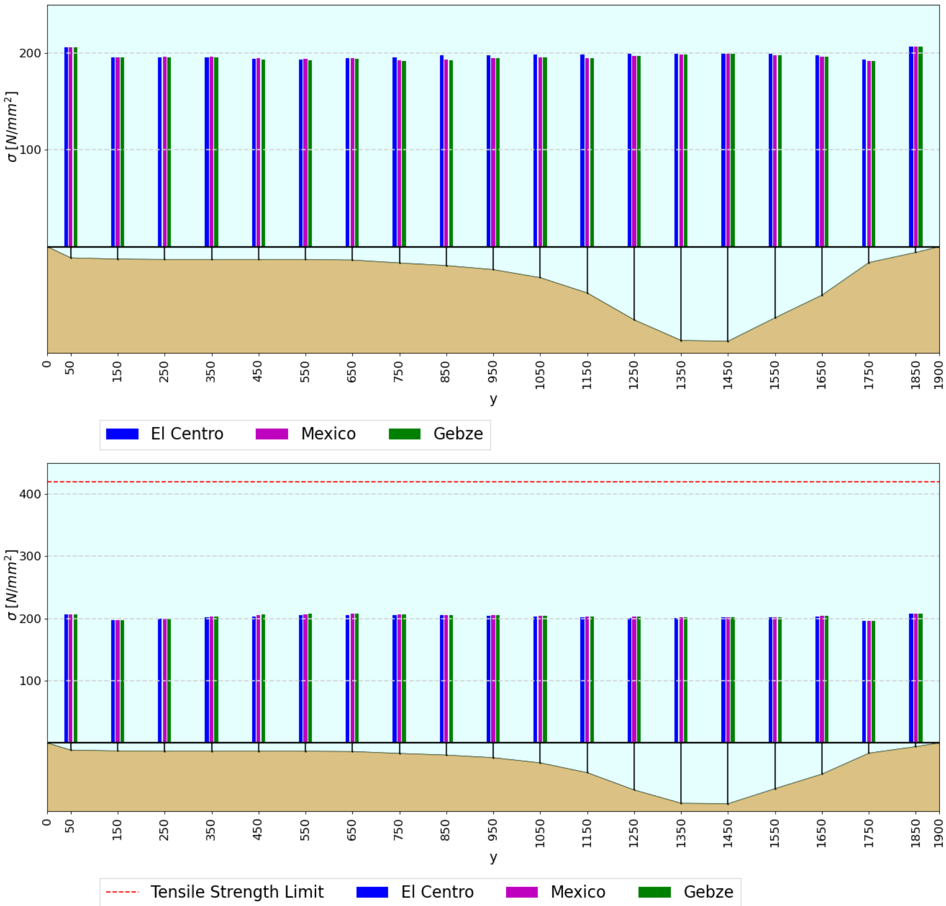

Figure 5.17: Minimum tension stress (top) and maximum tension stress (bot) tethers for transverse motion

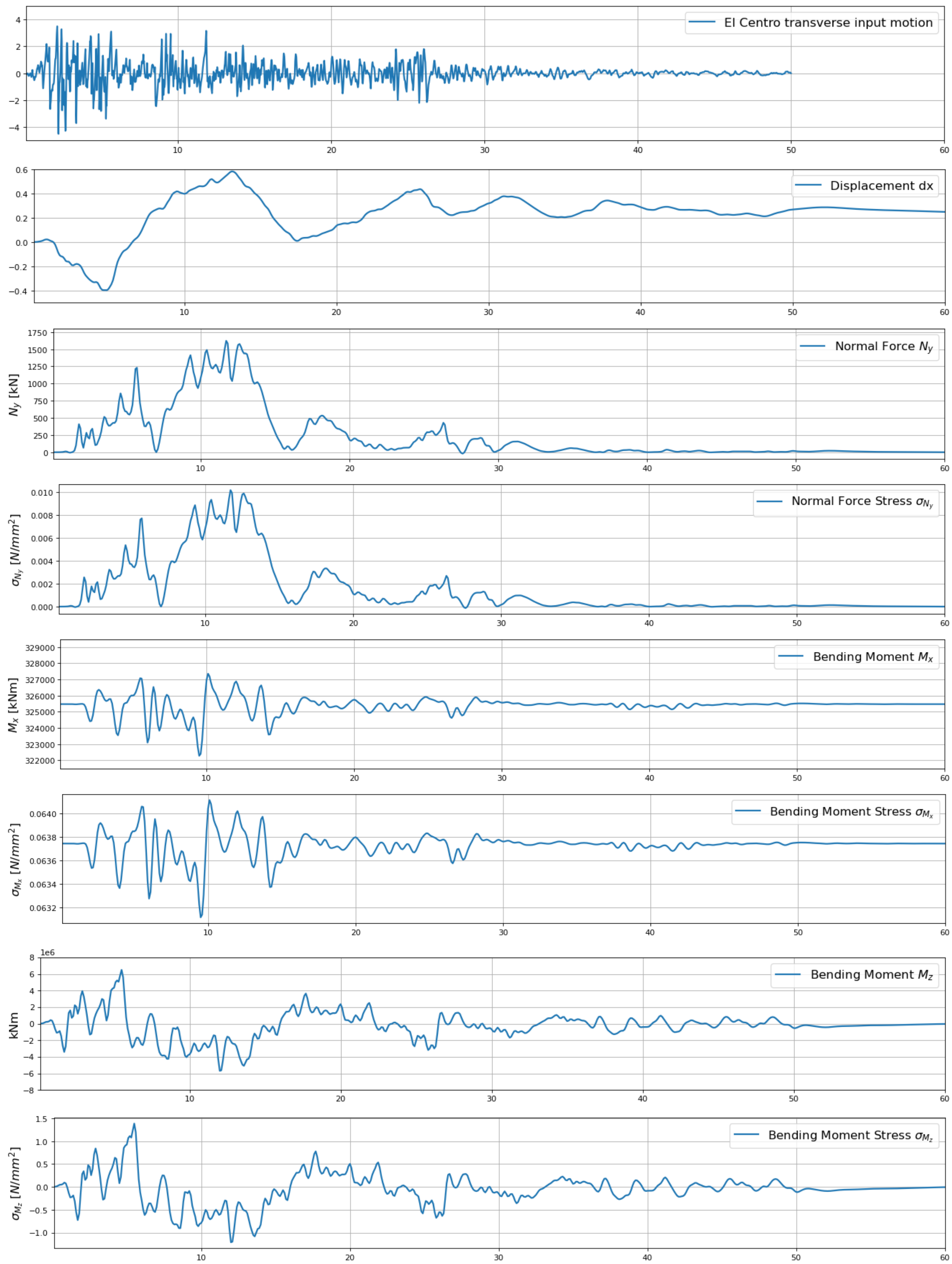

Figure 5.18: Results El Centro transverse direction singular node

Tunnel displacements

The displacements shown in the figure below are the maximum transverse displacements of the tunnel due to the transverse input motions. The longitudinal displacements remain zero. As explained previously, the SFT has some flexibility in the transverse direction. This results in a limited effect on the stresses but also in larger displacements. The figure below illustrates this. Overall the effect is still limited as the maximum is found to be $0.9\ m$ over a total tunnel length of $1900\ m$.

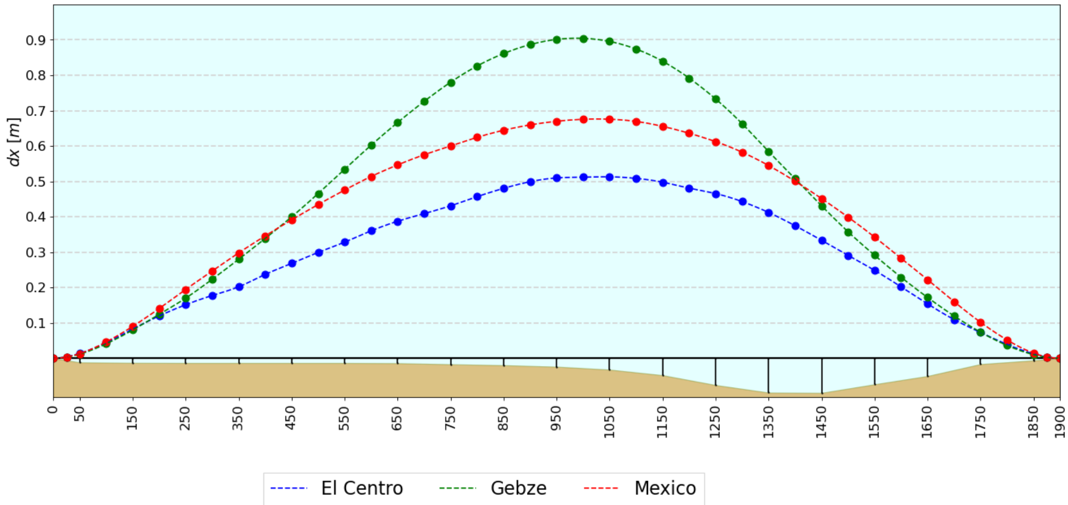

Figure 5.19: Maximum transverse displacements

Tether displacements

The figure below shows the time history of the transverse displacements of the 3^{rd} tether (from left to right). The displacements of this tether are shown at the bed ($z = 0$), $z = 0.25L$, $z = 0.50L$, $z = 0.75L$ and at the tunnel element ($z = L$), where L is the length of this tether. Here only the result of the El Centro input signal is given. It shows that from the bed towards halfway the tether, the displacement increases. From there, halfway the tether towards the tunnel element, the displacement decreases as the much larger mass of the tunnel elements, restrain the movements of the tether. Note that the maximum displacement of $z = L$ equals the displacement given for the El Centro signal in figure 5.19 at $y = 250\ m$. As the displacement of the tether largely declines when x approaches L, it can be assumed that the tunnel has a larger effect on the behaviour of the tethers.

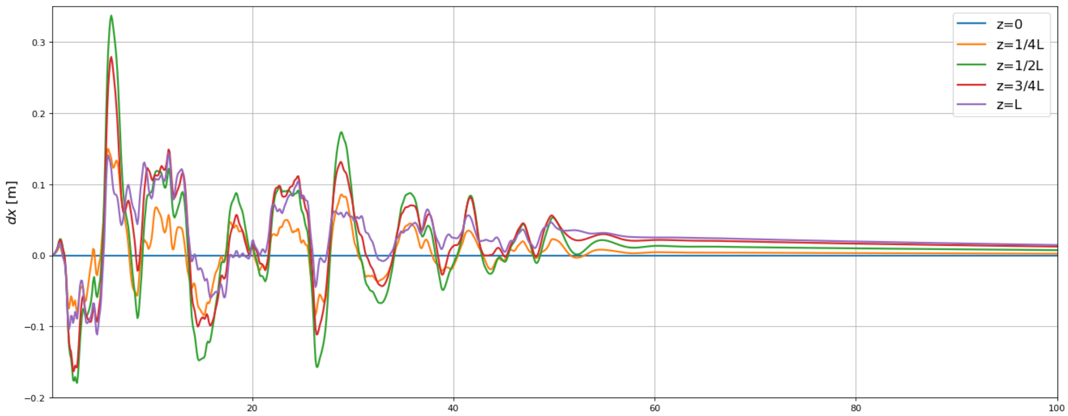

Figure 5.20: Displacement Tether 3 for transverse input motion

Longitudinal direction
Tunnel stresses
Next, the results for the longitudinal input motion. Like has been done for the transverse input motion, first, the tension stresses in the tunnel elements and the effect of the input signals are presented. The figure below shows the maximum obtained tension stress in these elements for the different input signals (top figure the total and bottom figure only those resulting from the input signal). Again, the highest stresses are found near the land tunnel connections. Also, it is clear to see that from the outside towards the middle of the tunnel, the stresses decline. Again it is assumable that the tethers have little to no influence on the stresses obtained in the tunnel elements and that these are mostly affected by the land connections. Comparing these results with those of the transversal input motion, the stresses found here are slightly larger. This is due to the higher axial stiffness of the tunnel compared with the transversal. This higher stiffness is due to the fact that the tunnel is fully clamped at both outer ends and can therefore hardly have any deformations in the axial direction. It is therefore also expected that the longitudinal deformations are less than the previously obtained transversal.

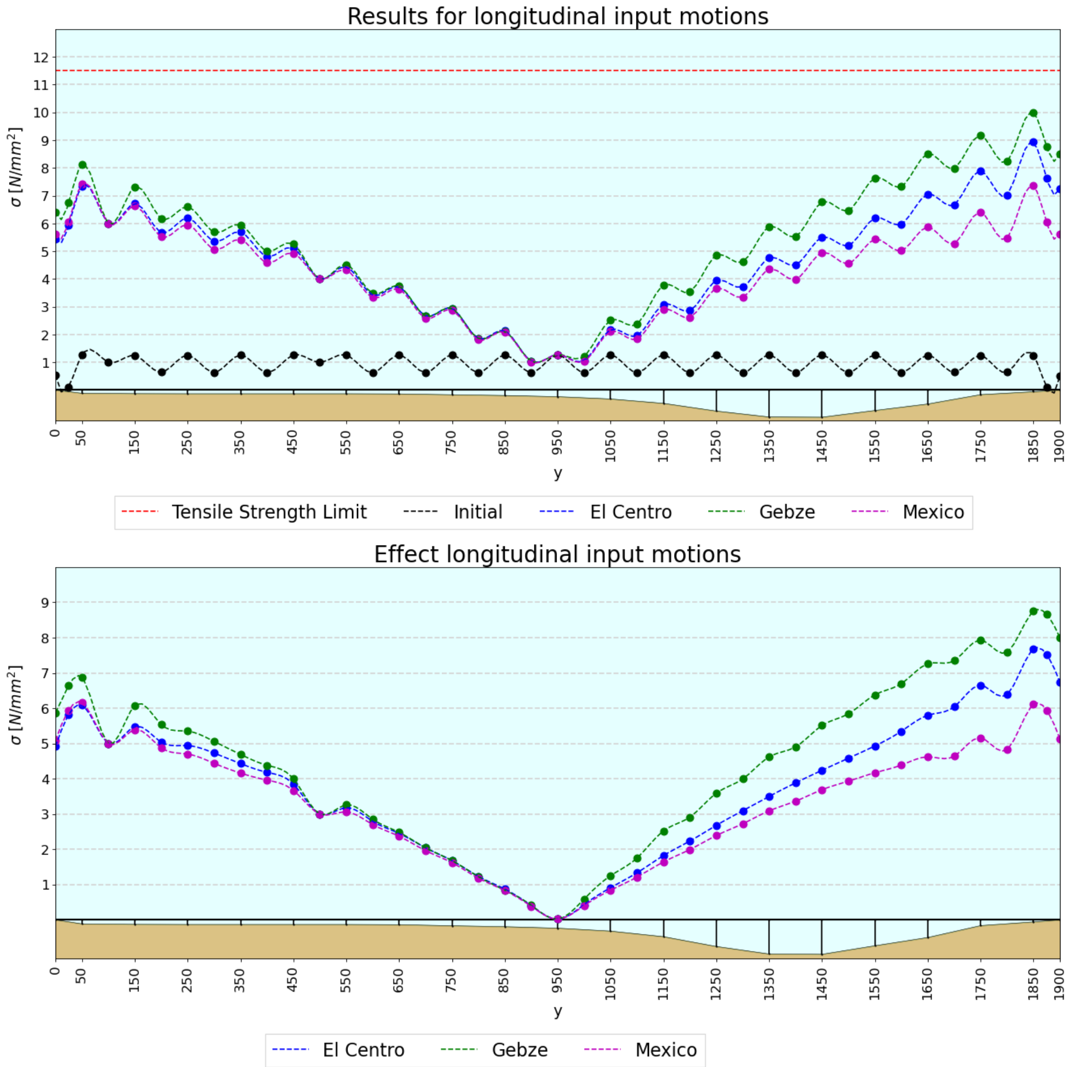

Figure 5.21: Resulting tensile stress due to longitudinal input motions (top) and the effect of longitudinal input motions (bot)

As has been done for the transverse input motion, the response of a singular node for the longitudinal motions is shown as well. Figure 5.23 on the next page shows these results. Where for the transverse input motion the total tension stress was mostly formed by the tensions resulting from bending moment M_z, the tensile stresses due to the longitudinal input motion are mostly formed due to the tension forces resulting from the normal force N_y. Bending moment M_x hardly deviates from its initial value and bending moment M_z remains zero throughout the entire analysis.

Tether stresses

The tethers have again been evaluated and the minimum and maximum obtained tensile stresses are again shown here. The results as shown in the figure below show that the longitudinal motion has a much larger effect on the tethers than the transverse input motion has. The maximum and minimum found in this analysis deviate more from the initial tensile stress as to where in the previous analysis the stress hardly changed. This shows that the stresses in the tethers are mostly dependent on the movement of the tunnel. As to where the tunnel has a larger stiffness in the normal direction, the displacements of the tethers are hindered as well resulting in larger stresses in these elements.

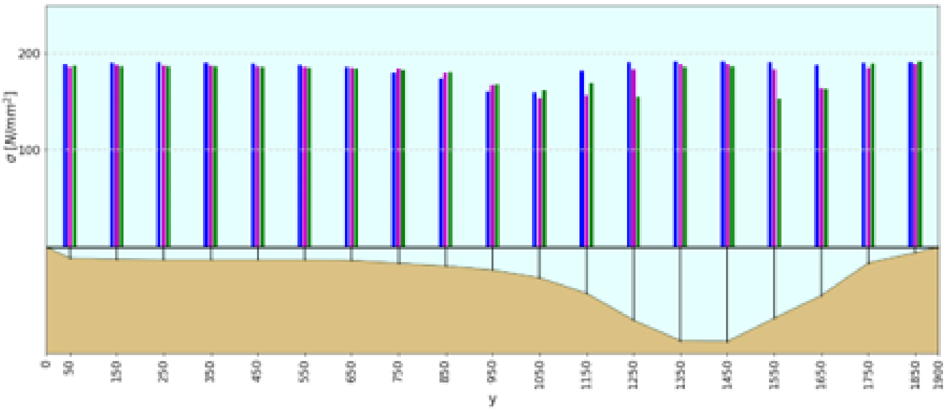

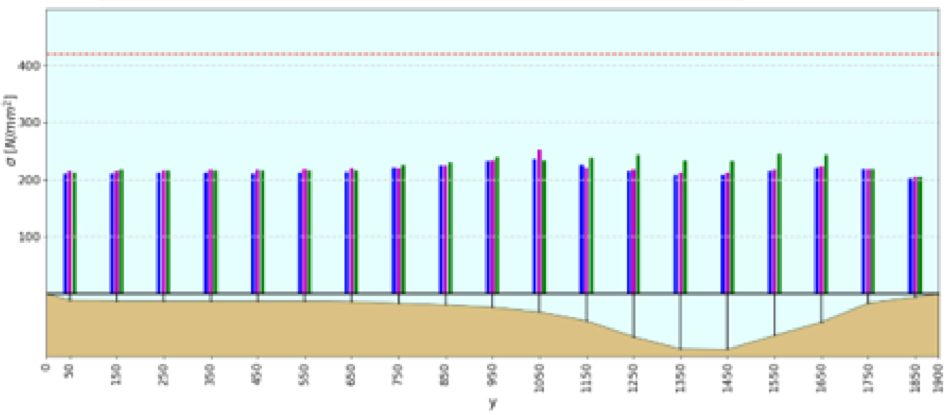

Figure 5.22: Minimum tension stress (top) and maximum tension stress (bot) tethers for longitudinal motion

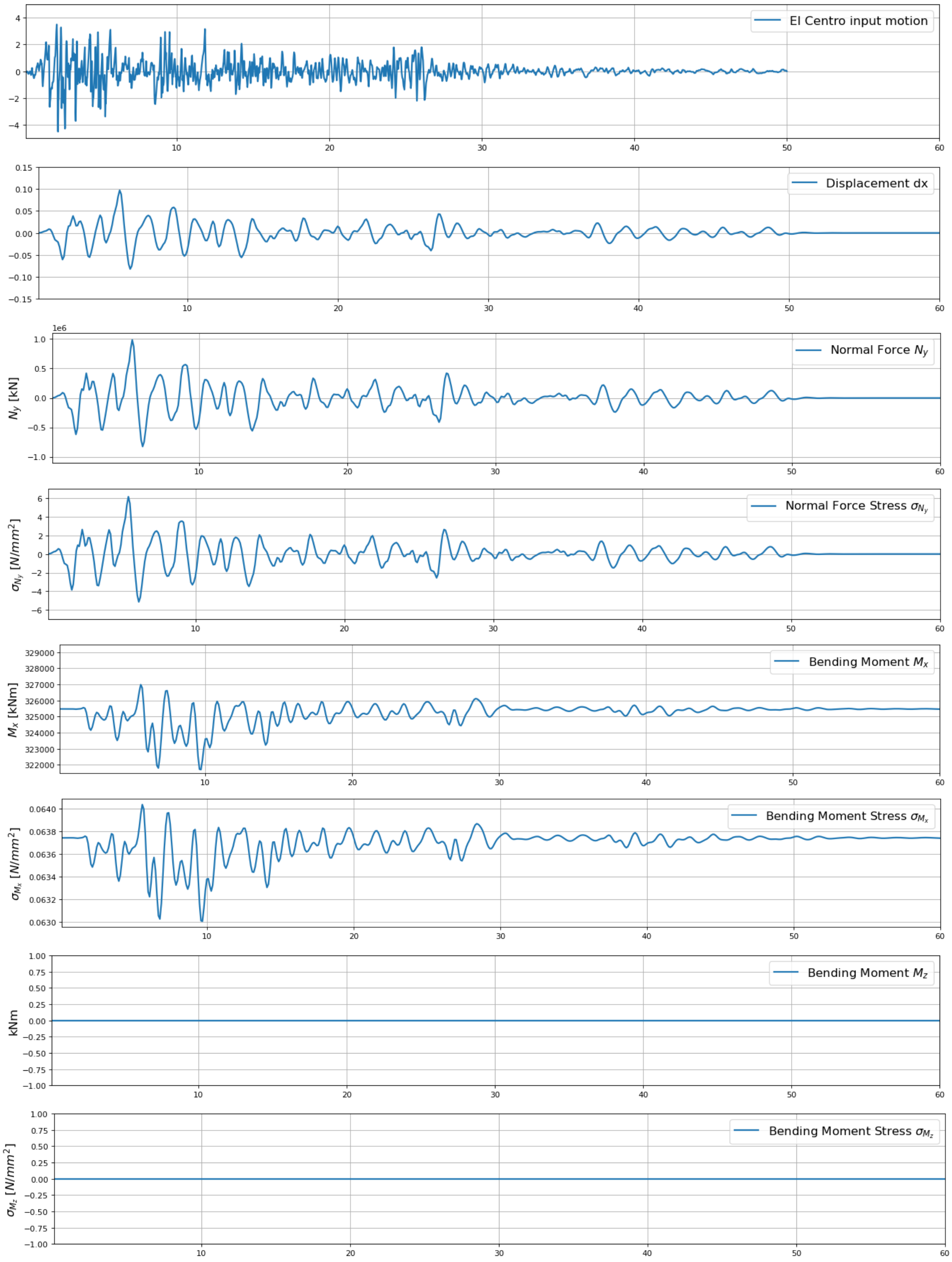

Figure 5.23: Results El Centro longitudinal direction singular node

Tunnel displacements

The resulting longitudinal displacements due to the longitudinal input motions are shown here. Compared with those of the transverse displacement, much smaller deformations are obtained. This results from the much larger stiffness of the structure in the normal direction as explained previously. The maximum displacement ranges from $0.09\ m$ up to $0.11\ m$ depending on the input signal.

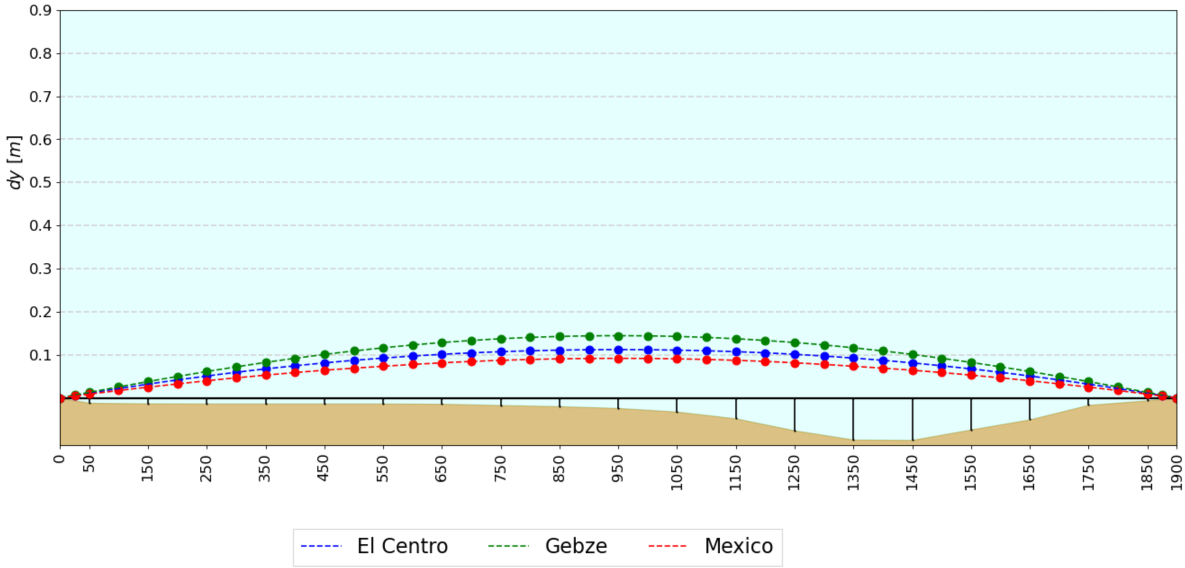

Figure 5.24: Maximum longitudinal displacements

Tether displacements

Figure 5.25 provides the same information as figure 5.20 but now for the longitudinal input motions. Equal results are obtained for the transverse input motion where the displacement increase from $z = 0$ towards $z = 0.50L$ and decreases from $z = 0.50L$ towards $z = L$. The displacement at the tunnel elements is now much smaller compared with the transverse input signal. This is due to the lower flexibility of the tunnel in the normal direction compared with the transverse direction.

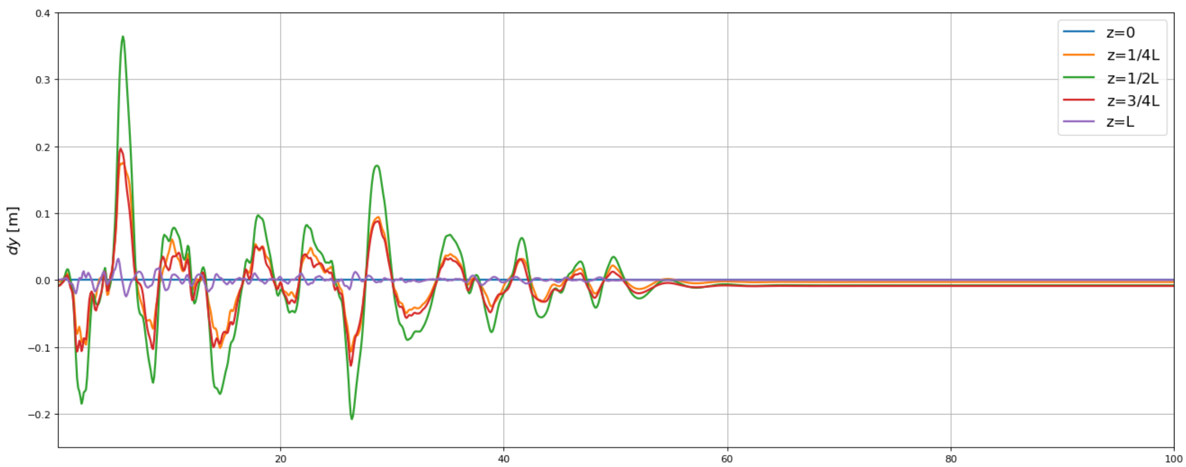

Figure 5.25: Displacement Tether 6 for longitudinal input motion

5.6. Wave passage effect

In the previously performed analyses, the input motions applied to the model were uniform throughout the entire model. Hence, each support of the structure would be excited at the same time as any other support. Where this may hold for the transverse input motion where the seismic wave does reach the support elements more or less at the same time, it does not for the longitudinal input motion. The incoming seismic waves travel with a certain propagation speed through the soil. For long structures, such as the SFT studied here, this would mean that the supports closer to the epicenter may notice this excitation a few seconds sooner than the supports further away from the epicenter. Previous studies show that including this effect does increase the seismic impact for both bridges (Bogdanoff et al. (1965) [7]) as for SFT's (Chen et al. 2010 [9],) To see how this phenomenon affects the SFT in this study, computations including this effect have been carried out.

To analyze the wave passage effect, a delay in excitations for the support in the finite element model is added. First, an assumption is made regarding the propagation speed of the seismic wave (v_s). In this analysis two velocities are compared with the uniform excitations for which the values $v_s = 800\ m/s$ and $v_s = 2000\ m/s$ are applied. Next, the seismic wave is applied at $t = 0\ s$ at the left land connection. From this point, the wave travels in the longitudinal direction where it will reach the first tether located 50 m away from the land tunnel. With the given propagation velocities, the arrival time of the seismic wave at this support is calculated. This process is done for every support of the tunnel until the seismic wave reaches the right land tunnel. Figure 5.26 shows the input signal of the El Centro event, applied on the outer ends of the SFT with $v_s = 800$ m/s.

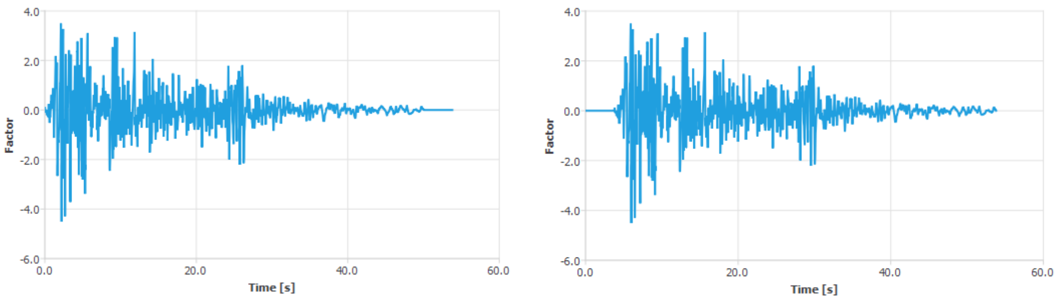

Figure 5.26: Input signal for the left land connection (left) and right land connection (right)

Figure 5.27 shows the resulting tensile stresses in the tunnel resulting from the uniform excitation and the wave passage effect. By applying the delay on the different supports, much higher stresses are observed. This could be due to the fact that, when applying the multi-support excitation, more modes of vibrations are excited. Another explanation could be that when applying the uniform excitation, the SFT moves as a rigid body and every node in the system has more or less the same velocity and direction as any other. When applying the multi-support excitation, the velocity and propagation direction of a node at one side of the tunnel could be completely different from a node on the other side of the tunnel which results in increasing forces. Comparing the different propagation speeds (where uniform can be seen as $v_s = \infty$), shows that the effect of the seismic wave increases as the propagation speed decreases. It is not expected that this relation is linear as when the propagation speed reaches zero, the effect is expected to decline.

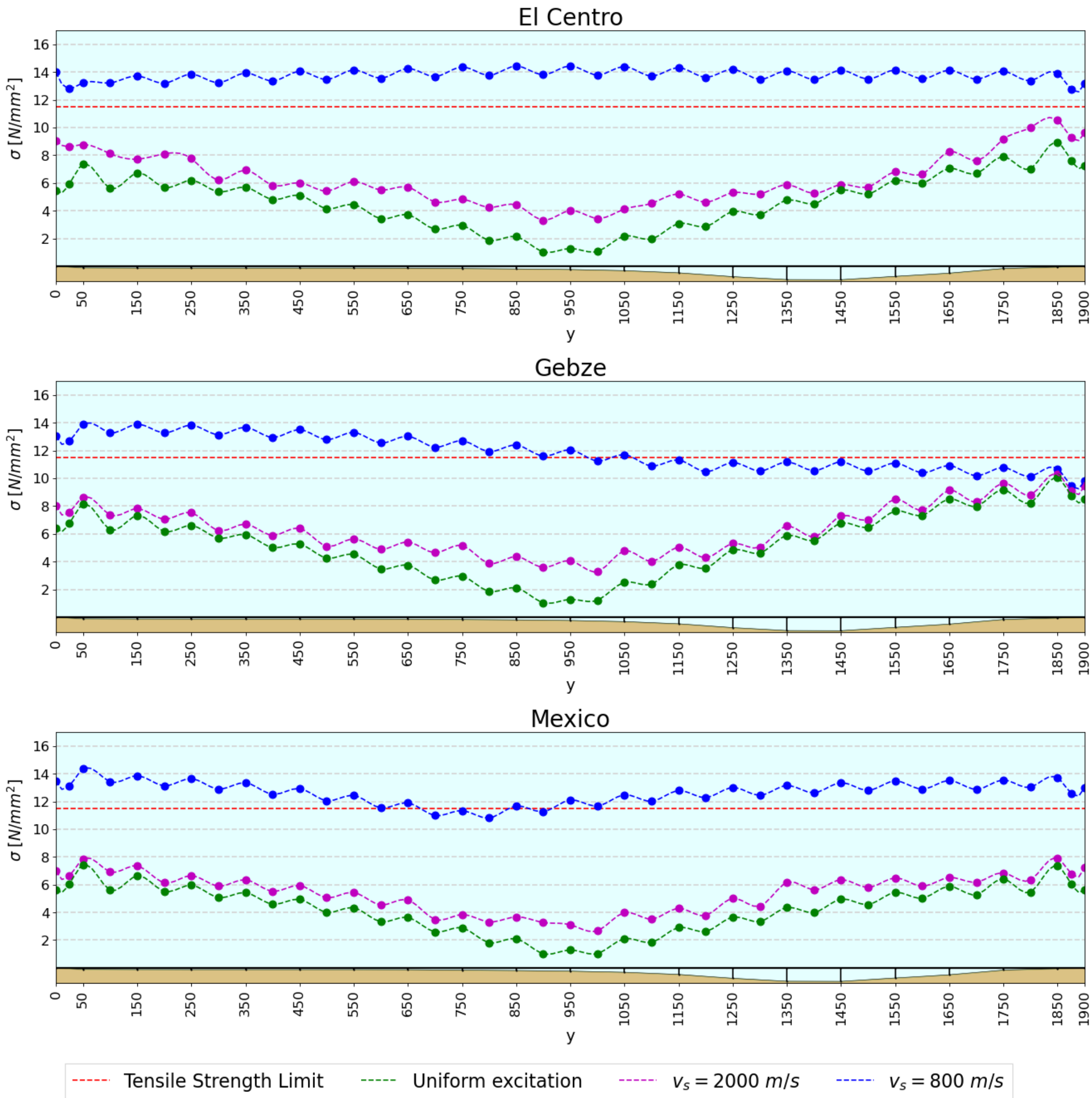

Figure 5.27: Tensile stresses for wave passage effect

5.7. Vertical input motion and angle of attack

The seismic motions applied in the previous analyses were either in the transverse direction or longitudinal direction and both included as horizontal input motions. In reality, an input motion would consist of both a horizontal component and a vertical component. The horizontal component may have any orientation regarding the structure and different types of seismic waves may result in different directions of excitation [14]. Therefore, it is very unlikely that the seismic input will consist of only one horizontal component. This section will discuss how both the orientation regarding the input direction (angle of attack) and the vertical motions may affect the SFT.

5.7.1. Angle of attack

The previous analyses showed that applying an input motion in the transverse direction or in the longitudinal direction result in completely different results. As explained in the section above, it is very unlikely for an earthquake to consist of only one horizontal component and that the angle of attack may take any value. The figure below illustrates the different horizontal components of an earthquake and this angle of attack (θ),

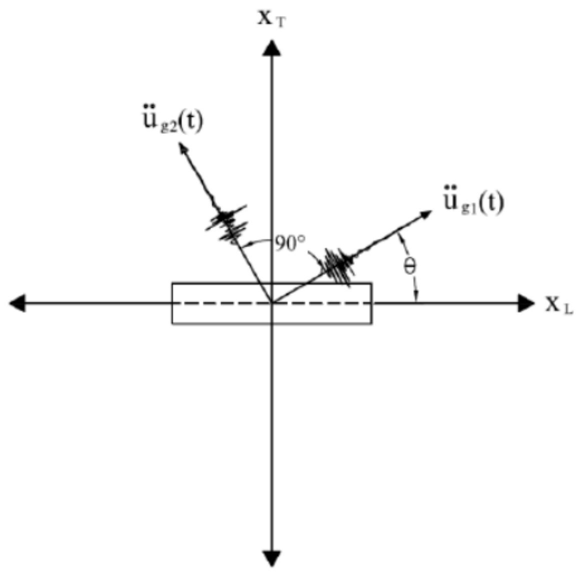

Figure 5.28: Angle of attack

Much research has been done regarding the critical angle of attack on e.g. steel bridges (Altunisik et al. (2016) [3]) and skewed concrete bridges (Atak et al. (2014) [4]). Both found that the critical direction was neither pure orthogonal nor transversal but may lay in a large intermediate range. Hence it is expected that the critical angle for the SFT studied may neither be one of the two applied. Yet, the aim of this study is not to find the most critical values but to gain a better understanding of how the input motions affect the tunnel. By applying the input motions only in the two main directions of the structures, it is easier to distinguish the different directions from each other and see how each of them affects the tunnel differently. One could argue that an earthquake may always have horizontal components both the transversal as well as in the longitudinal direction. Both input motions could be applied simultaneously. However, an earthquake always has one main direction which contains the largest excitation, the secondary component (perpendicular to the main direction) would be much smaller. Applying both scaled input motions simultaneously results in an excitation with a severity much larger than was scaled for. As there aren't any methods described by Eurocode for scaling the secondary component of an earthquake, only the main directions are applied.

5.7.2. Vertical input motions

The tethers in the previous analyses were hardly affected by the horizontal excitations. As the tethers are very slender and the lateral stiffness is limited, it is not unexpected that these resulting stresses remain limited. Studies were performed concerning the effect of vertical input motions on long-span cable-stay bridges (Bipin, 2014 [27]). It was found that mostly the cables were affected by these vertical input motions. The cables of these bridges show many similarities with the tethers and whereas the vertical motions were left out of the scope of this study, it might still be of interest to see how the vertical input motions affect the tunnel and to see whether these are more critical for the tethers. To do so, the same input motions as applied in the previous analyses are applied on the model but now as an acceleration in the vertical direction (NEN provides other expressions for vertical spectra but for now the horizontal signals will be applied just to show the differences in the results). By applying the same procedure as was done in the previous analyses, the tensile stresses in the tunnel elements and tethers are found. For the tunnel tensile stress, the following results were obtained:

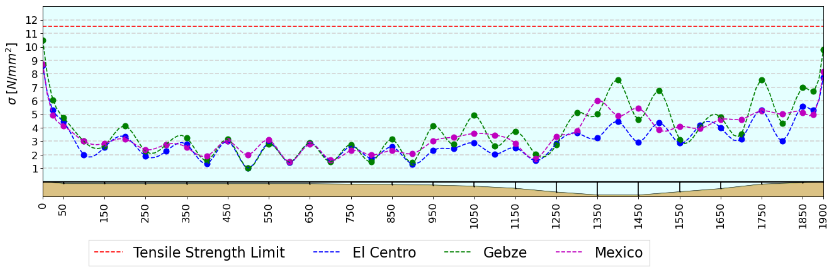

Figure 5.29: Tension stresses tunnel elements due to vertical input motions

The resulting tunnel stresses show some similarities compared with those resulting from the horizontal input motions. Higher tensile stresses are found near the land connections from where the stresses more or less decline towards the midspan of the tunnel.

The results of the tether tensile stresses are shown in figure 5.30. These results do show a larger effect of the input motions as both maximum and minimum values obtained are much further from the initial value and for some tethers even surpass the design criteria. From this, it can be concluded that for the tethers, vertical input motions are more critical and so for further studies on this subject, it is highly advisable to evaluate these in more detail.

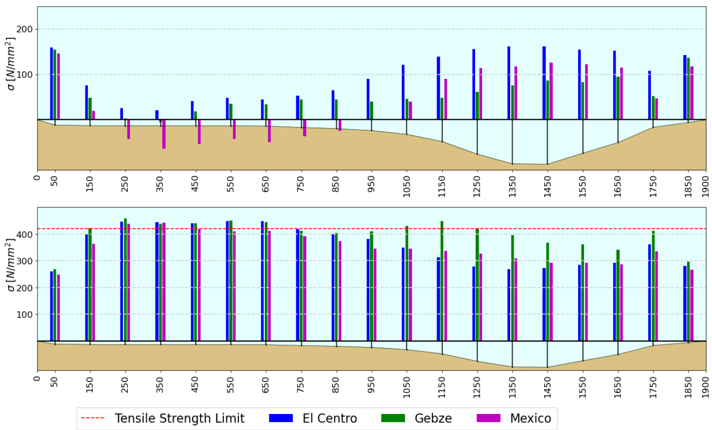

Figure 5.30: Minimum tension stress (top) and maximum tension stress (bot) tethers for vertical motion

5.8. Conclusion

In this chapter, the eigenvalue analysis and the seismic analyses for the different input signals have been performed. For these analyses, it was found that:

- The eigenmodes of the tunnel have been subdivided in three directions; transversal, vertical and longitudinal. It was found that especially the transversal eigenperiods of the structure are high and so the SFT has a large flexibility in the transverse direction. This flexibility declines for the vertical direction as lower eigenperiods are found here. This is due to the extra vertical stiffness the tethers provide. Much lower eigenperiods were found for the normal direction as the SFT is fully clamped at both sides.
- The fundamental eigenperiods of the tethers were found in the range of 0.66 up to 15.08 seconds. Larger tether length results in higher eigenperiods as was shown in figure 5.13.
- Most of the fundamental eigenperiods of both the tethers as the tunnel lay far from the peak values of the response spectra (for which the peak values are found for periods smaller than 0.5 second) and so are found in a range where the seismic response is limited.
- The results of the transverse input motion show a limited effect on the tensile stresses in the tunnel and in the tethers. This is due to fact that the tunnel is relatively flexible in the transverse direction and the eigenperiods are far from the peak values of the spectra. Looking at the resulting displacement this transverse flexibility is found back in much larger displacements (compared with the results of the longitudinal displacement)
- The results of the longitudinal input motion were found to be more critical than those of the transverse. As the resulting eigenperiods in this direction were much lower, higher response values in the spectra are obtained and as the axial flexibility is much lower, larger stresses are found. This smaller flexibility does result in lower displacements
- Applying the wave passage effect (multi-support excitation) results in much larger stresses than when applying a uniform excitation for the longitudinal input motion as the SFT doesn't move as a rigid body as it did for the uniform excitation. With the wave passage effect included different nodes in the tunnel may have different acceleration in a different direction which results in larger stress. Also applying the seismic wave may result in the excitation of more modes of vibration.
- Vertical input motions are beyond the scope of this study but the appliance of one does result in more severe seismic responses in the tethers as was shown in figure 5.30. This is due to the fact that the axial stiffness is much larger than the lateral stiffness of these elements.

6

Design effects on seismic impact

The analyses made in the previous chapter were all based on the design as defined in chapter 3. This chapter will be used to examine how altering the design influences the seismic response of the tunnel to gain a global idea of the effect of each of these elements on the dynamic behaviour.

6.1. Design alterations for the SFT

In the case study described in chapter 3, some choices were made regarding the design which may affect the seismic response if chosen differently. To see how these design options affect the seismic response, different configurations for the tunnel will be made after which the same analyses will be performed. By comparing the results of these analyses, a global idea of how each design option, alters the dynamic behaviour of the SFT can be obtained. The design options which will be tested are; the number of mooring lines, the inclination of the tethers, the number of tethers, the alignment of the tunnel and the application of base isolation. For each analysis, the eigenvalues, the tensile stresses in the tunnel elements, the tensile stresses in the tethers and the displacements of the tunnel elements will be evaluated. For the stresses in the tunnel elements, only the effect of the seismic excitation will be presented, which is obtained by subtracting the initial tensile stresses of the total. For the displacements, only the transverse displacements due to the transverse input motions and the longitudinal displacements for the longitudinal input motions are examined as displacements orthogonal on the input directions are negligible. Finally, only the scaled El Centro input signal is applied which is applied uniformly for both the transverse and the longitudinal direction.

6.2. Mooring Line Configuration

To evaluate the effect the mooring lines have on the seismic response, multiple configurations will be tested. Whereas in the initial design, the same number of mooring lines as tethers were added. For this section, two configurations will be tested with one having half the number and another having twice the number of mooring lines. The figure below illustrates the different configurations. The stiffness of the mooring lines is still as described in chapter 3.

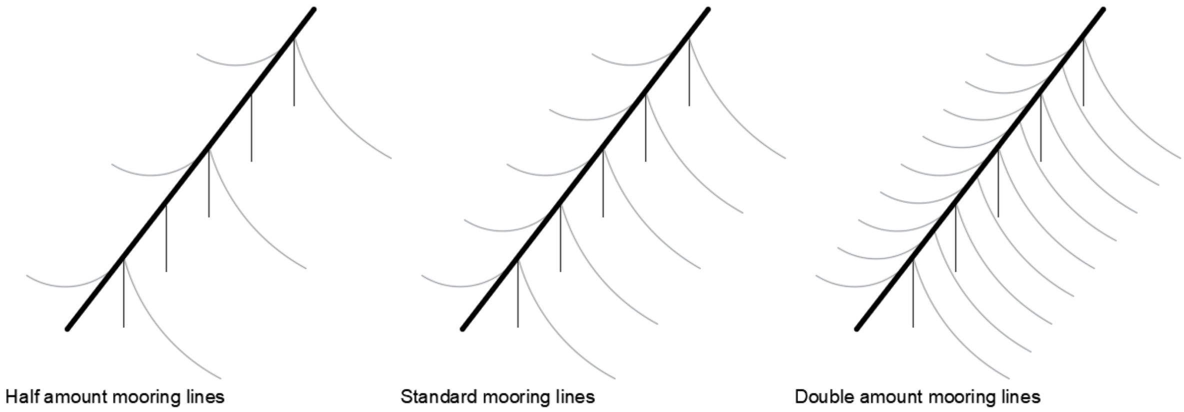

Figure 6.1: Mooring line configurations

6.2.1. Results Eigenvalue analysis

The different mooring line configurations result in different eigenvalues for the tunnel elements. An increase in mooring lines attached to the tunnel results in a higher transverse stiffness and so lower eigenperiods for the eigenmodes in the horizontal plane. Figure 6.2 gives an overview of how the eigenperiods for each direction differ per mooring line configuration. The left figure provides the eigenperiods for the eigenmodes in the horizontal direction, the middle figure for the vertical direction and the right figure for the normal direction. The x-axis provides the information regarding the different configurations (here ML stands for mooring line) and the y-axis provided the corresponding eigenperiod in seconds. The color of the marker tells which eigenperiod is shown (for each direction the first five eigenperiods are provided). The figures show that adjusting the number of mooring lines does not affect the eigenmodes in the vertical and normal direction, but it does affect the eigenmodes in the horizontal direction. Adding more mooring lines results in a lower transversal flexibility of the structure and so in lower eigenperiods for these eigenmodes (as explained previously). The eigenperiods of the tethers are not affected by altering the mooring line configuration

So an increasing number of mooring lines shifts the fundamental eigenperiods of the tunnel elements more towards the higher values of the response spectra of the input signals which should eventually result in higher effects of the seismic input. Figure 6.3 displays the shift of the 2^{nd} eigenperiod of the horizontal mode on the input spectra (the spectra are only shown between $T = 0$ and $T = 4$ as they are only described in this range). Whereas the higher values of the response spectra are located in the range of $T = 0 - 0.5\ s$, the fundamental eigenperiods as shown in figure 6.2 are far from these peak values. So whereas adding the number of mooring lines as was done in the configuration above does stiffen the structure, the eigenvalues remain in the lower bounds of the response spectra and so little difference is expected.

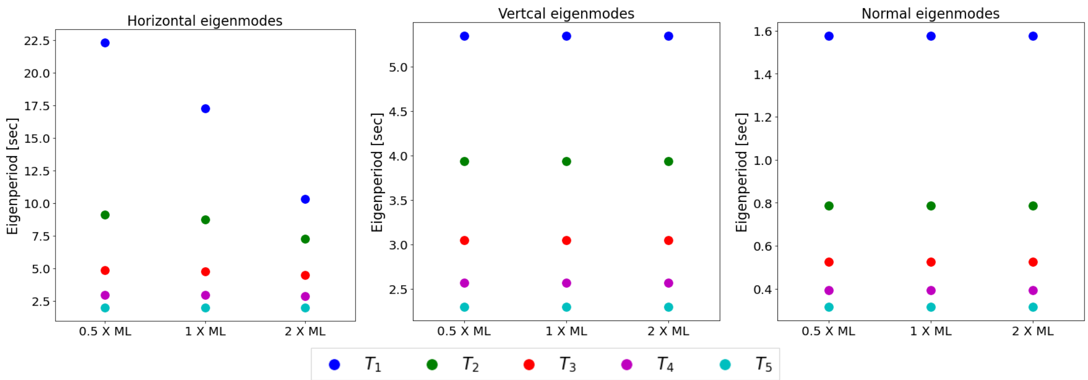

Figure 6.2: Resulting eigenperiods for tunnel per mooring line configuration

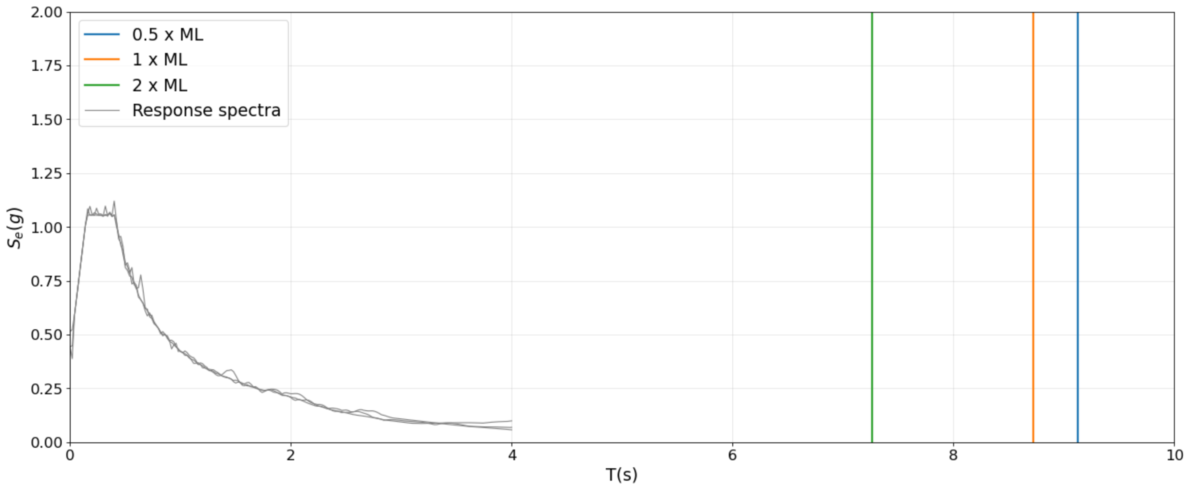

Figure 6.3: Effect of mooring lines on 2^{nd} horizontal eigenmode

6.2.2. Results Time-History analysis

The time-history analyses for the three configurations are performed with the input motion in the transverse and longitudinal direction. Here the resulting tunnel stresses, tethers stresses and tunnel displacements are presented.

Stresses tunnel elements

Figure 6.4 show the resulting tunnel stresses for each configuration for both input directions. As explained at the beginning of this chapter, only the stresses resulting from the input motion are displayed. The results show that the resulting tunnel stresses from the three different configurations are as good as equal to each other. This means that the effect that the mooring lines have on the seismic performance is negligible. This is due to the low stiffness these sagging mooring lines have. The results from the eigenvalue analysis showed that by doubling the number of mooring lines the primary eigenperiods are, shifted towards, but remain far from the peak values of the seismic spectra, and so it is still not expected that more severe responses would occur. Whereas for the transverse input motion, some small differences are noticeable, the results for the longitudinal motions are the same, this is because the mooring lines do not provide any stiffness in the longitudinal direction.

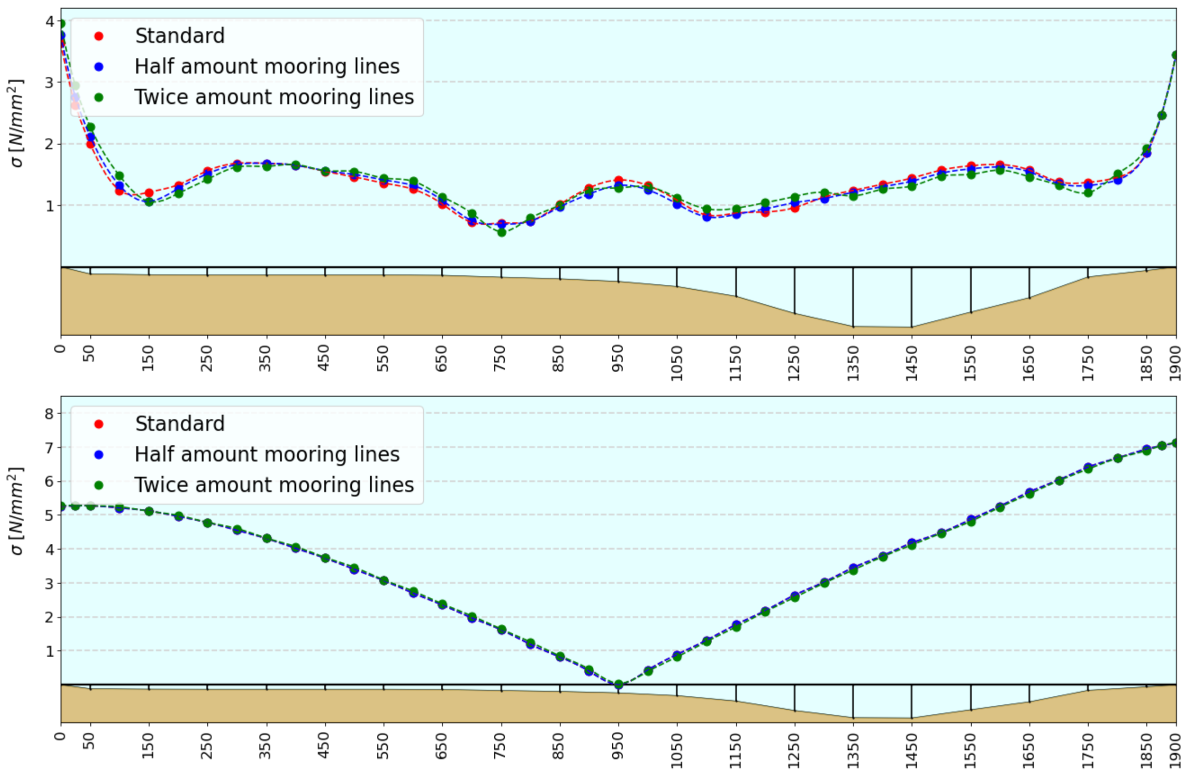

Figure 6.4: Tunnel tensile stresses for mooring line configuration for transverse (top) and longitudinal input motion (bot)

Stresses tethers

The resulting tether stresses are shown in figure 6.5. Here the left column provides the results for the transverse input motion and the right column for the longitudinal input motion, the top row displays the minimum and the bottom row the maximum. All four figures show that for each mooring line configuration, the resulting tether stresses are the same and so one can conclude that the mooring lines do not affect the tether stresses.

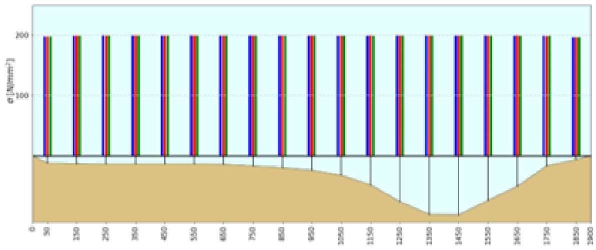

(a) Minimum tensile stresses transverse input motion

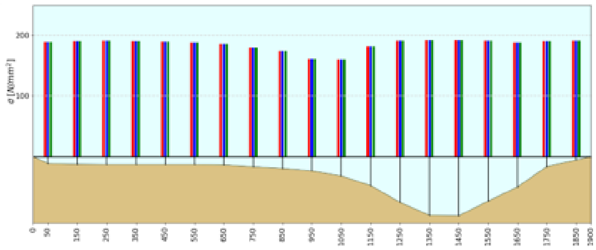

(b) Minimum tensile stresses longitudinal input motion

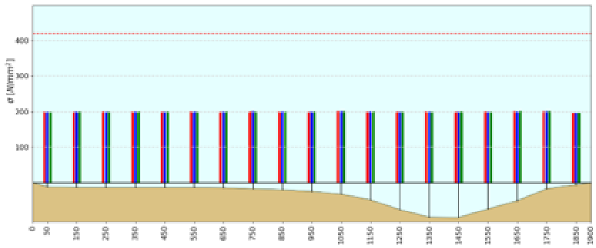

(c) Maximum tensile stresses transverse input motion

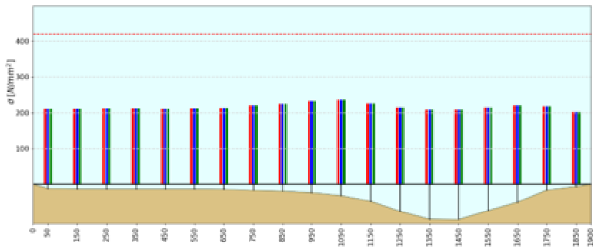

(d) Maximum tensile stresses longitudinal input motion

Figure 6.5: Tensile stresses tethers for different mooring line configuration

Displacements tunnel element
The resulting tunnel displacement are given in figure 6.20. The top figure provides the transverse displacement due to the transverse input motion and the bottom figure provides the longitudinal displacement due to the longitudinal input motion. The longitudinal displacement due to the transverse input motion and the transverse displacement due to the longitudinal input motion are both zero. Where the mooring lines do not affect the longitudinal displacement, they do affect the transverse displacement. By doubling the number of mooring lines, the displacement decreases by 9%. When the number of mooring lines is halved the displacement increases by 15%.

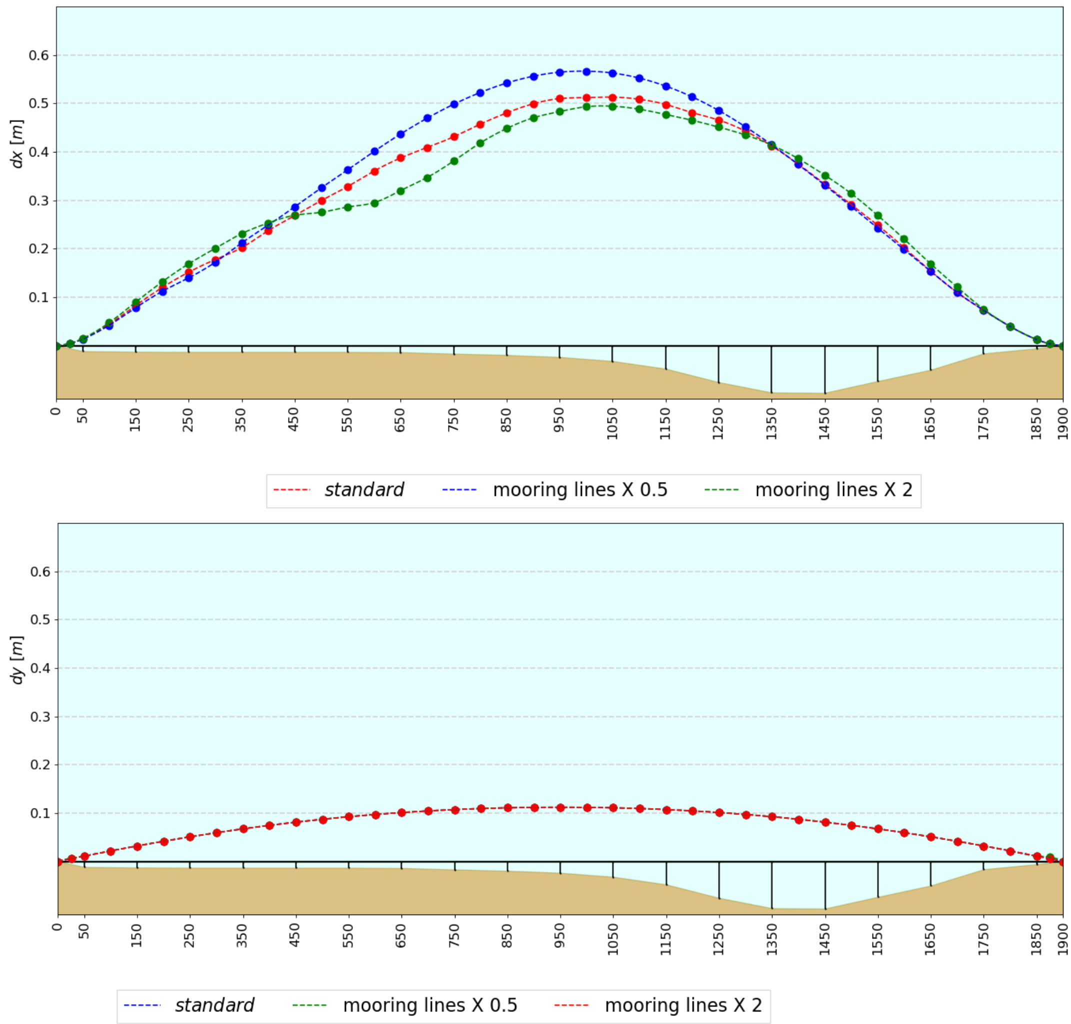

Figure 6.6: Displacements for different mooring line configuration for transverse (top) and longitudinal input motion (bot)

Conclusion
Overall it can be concluded that as the stiffness of the sagged mooring lines is not sufficient enough, the effect on the tethers and the stresses in the tunnel is very limited. Adding more does result in lower displacements. If more mooring lines would be added to the system it is expected that eventually, they would affect the tunnel stresses. This would occur as the horizontal eigenmodes are shifted to higher values of the spectra (figure 6.3).

6.3. Tether configuration

So far only vertical tethers have been used as a support system for the SFT. In this section the effect of inclined tethers will be analysed. Figure 6.7 shows the configuration of these inclined tethers where φ gives the angle of inclination. Since the inclined tether may now support the SFT not only vertically but also horizontally, the mooring lines have been removed as their purpose was to act as an horizontal constraint. For this study the initial configuration ($\varphi = 90°$) will be compared with two configurations, one with inclination angle $\varphi = 70°$ and one with inclination angle $\varphi = 45°$. Figure 6.8 shows the FEM's for these different tether configuration. By decreasing the inclination angle, the normal force in the tethers due to the buoyancy decreases as well, to obtain a clearer insight on the effect in the tethers, the tether cross-sections for each inclination angle has been adjusted such that the resulting initial tensile stress remain around 200 N/mm^2.

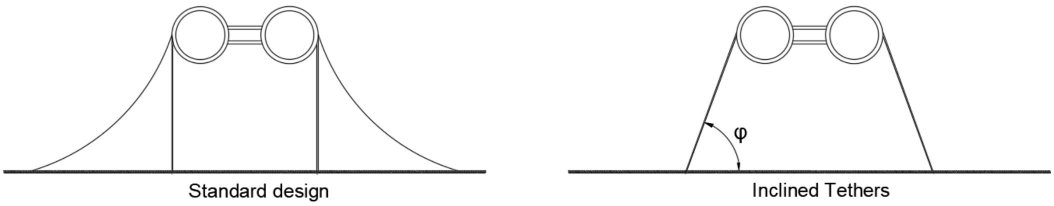

Figure 6.7: Inclined tether schematization

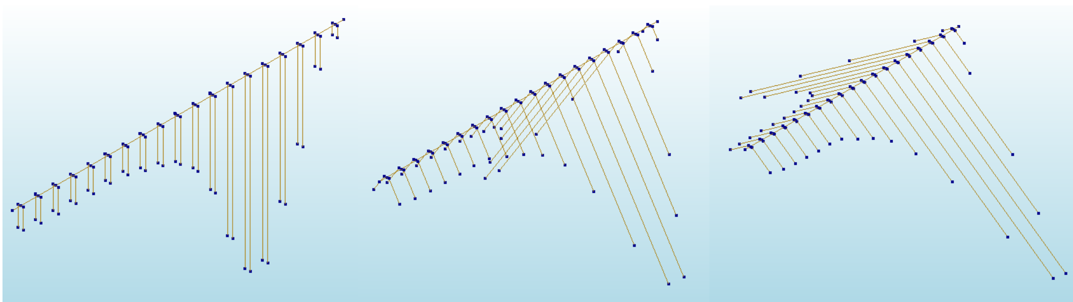

Figure 6.8: FEM for $\varphi = 90°$ (left), $\varphi = 70°$ (middle) and $\varphi = 45°$ (right)

6.3.1. Results Eigenvalue analysis

The resulting eigenperiods of the tunnel for the three different eigenmodes are shown in figure 6.9. The results show that when decreasing the inclination angle, the eigenperiods for the horizontal eigenmodes decrease and those of the vertical eigenmodes increase. i.e. decreasing the inclination angle results in a stiffer structure in the transverse direction and a more flexible structure in the vertical direction. This is as expected as the more horizontally orientated tethers have a smaller contribution in the vertical support than the vertical tethers have.

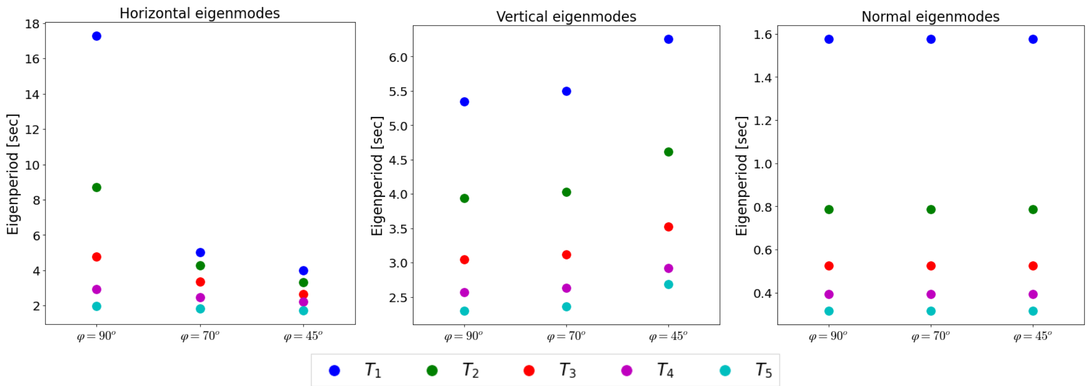

Figure 6.9: Resulting eigenperiods for tunnel per tether inclination

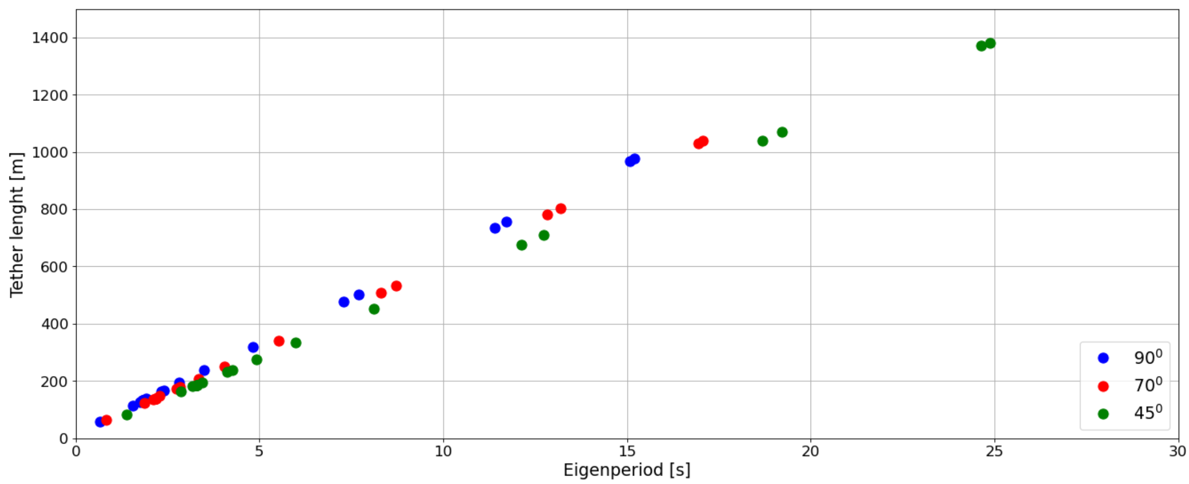

Figure 6.10: Eigenperiods tethers per inclination angle

Figure 6.10 shows the eigenperiods of the different tethers. With a decreasing inclination angle, a larger tether length is found and so much larger eigenperiods are found for the tethers with $\varphi = 45°$. As for the relation between tether length and eigenperiod, the eigenperiods of the tether under a smaller inclination angle seem to have slightly increased. This is mostly due to small deviations of the initial tensile stress in the model. It can be expected that the relation for the different angles remains the same.

6.3.2. Results Time-History analysis

Stresses tunnel elements

Figure 6.11 shows the effect of the inclination angle for both transverse and longitudinal input motions. For the transverse input motion, the range of the stresses for the different configurations is limited. As the inclination angle decreases larger differences between the stresses at the tethers and the stresses mid-span are obtained (larger oscillations of the line) but yet on average, similar results are obtained. This again shows that the tethers have a limited effect on the stresses in the tunnel. The results of the longitudinal input motion don't show any difference for the different inclination angles which is expected as the inclination only provided an extra stiffness in the transverse direction.

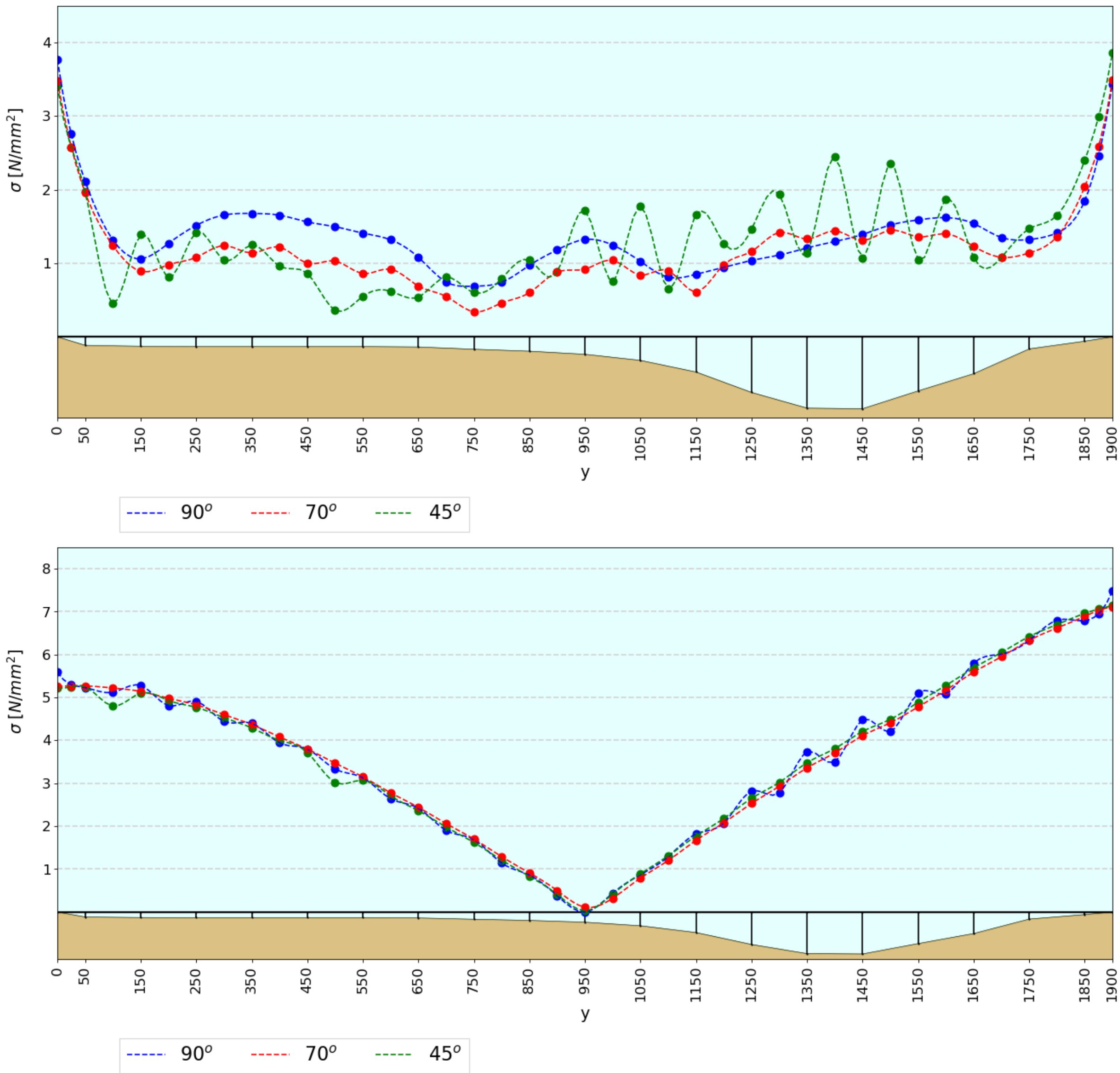

Figure 6.11: Results different tether inclinations for transverse (top) and longitudinal input motion (bot)

Stresses tethers

Figures 6.12a - 6.12d show the resulting maximum and minimum tensile stresses obtained in the tethers. For the transverse input motion, a decrease of inclination angle provides an increasing effect on the tethers. As the inclination angle decreases the tethers are orientated more in line with the seismic input direction. This results in a larger effect on these elements as can be seen in the figures. The results for the longitudinal input motion remain mostly the same.

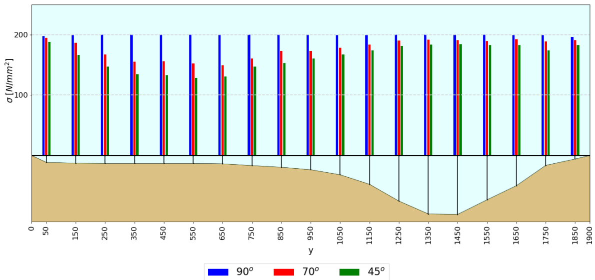

(a) Minimum tensile stresses transverse input motion

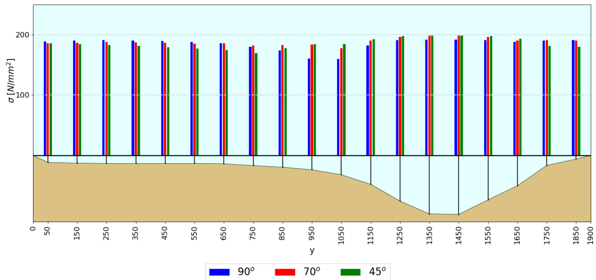

(b) Minimum tensile stresses longitudinal input motion

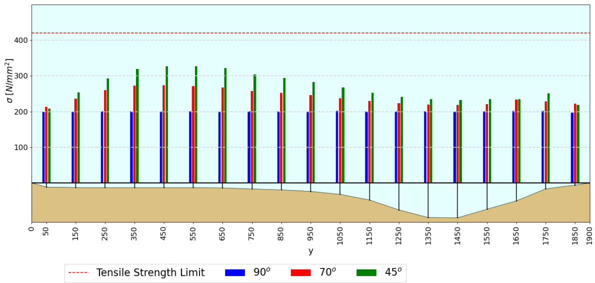

(c) Maximum tensile stresses transverse input motion

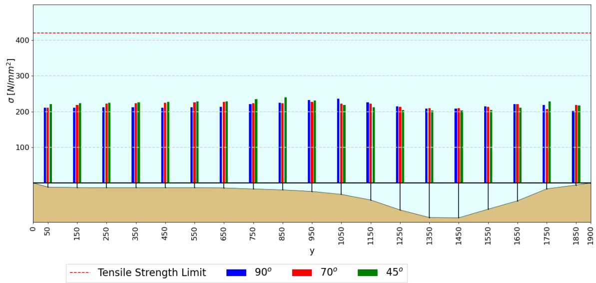

(d) Maximum tensile stresses longitudinal input motion

Figure 6.12: Tensile stresses tethers for different inclination angles

Displacements tunnel element

The displacements for both input motions are shown here. Again, for the longitudinal input motions, no differences are found as the transverse inclination does not effect the longitudinal stiffness of the structure. For the transverse displacements a decreasing displacement is found for a decreasing inclination angle. As the tethers are more inclined, the bedding stiffness increases and the displacements are more hampered. By applying an angle of $70°$ the maximum displacement is reduced by 32%. Applying an angle of $45°$ gives a reduction of 37% (compared with the vertical tethers).

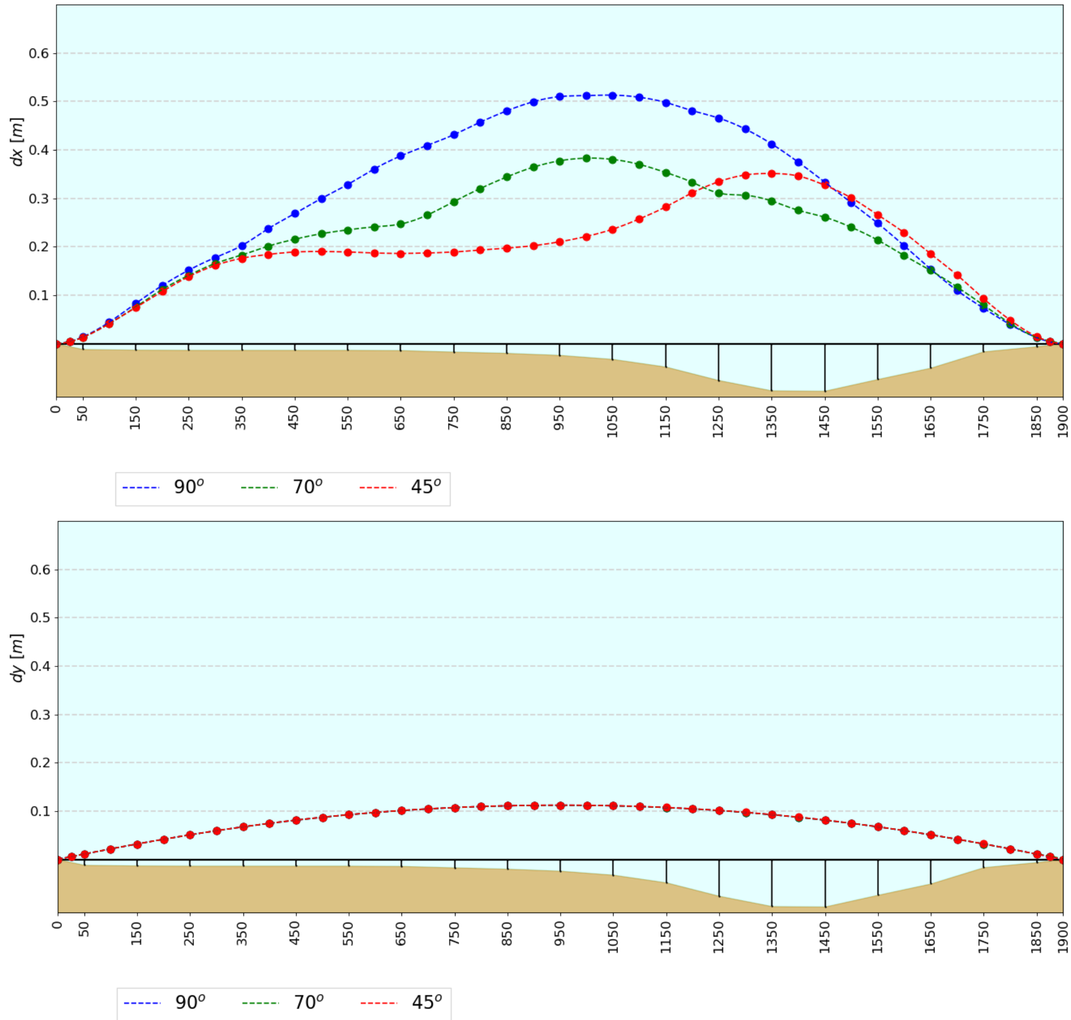

Figure 6.13: Displacements for different inclination angles for transverse (top) and longitudinal input motion (bot)

Conclusion

The different tether configurations show that inclining the tethers results in an increased effect of the horizontal motions on the tethers as the inclining the tethers act more as a horizontal support than the vertical do. This does also results in a smaller horizontal displacement of the tunnel. It is expected that by inclining the tether, the effect of vertical input motions will decrease in terms of tether stresses but increase in terms of the vertical tunnel displacements.

6.4. Tether spacing

The next analyses will be used to test the effect of the number of tethers. In the case study described in chapter 3, a tether spacing of $\Delta L = 100$ m was applied. The see how the number of tethers influences the seismic response, again two configurations will be made. One with a spacing of $\Delta L = 200$ m resulting in half the number of tethers and one configuration with $\Delta L = 50$ m resulting in twice the number of tethers. The figures below show the schematizations and FEM's for these different configurations. As the spacing changes, the resulting tension forces in the tethers change as well. By increasing ΔL from 100 to 200 meters, the resulting tension force is double and for reducing the spacing to $\Delta L = 50$ m the tension force is halved. To remain an initial tensile stress 200 N/mm^2 in the tethers for each configuration, the cross-sectional area for the tethers is doubled for $\Delta L = 200$ m and halved for $\Delta L = 50$ m. Table 6.1 gives an overview of the different dimensions applied.

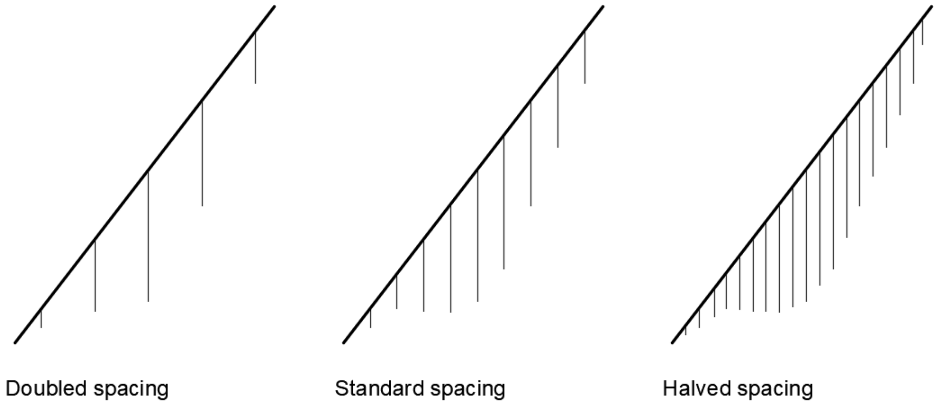

Figure 6.14: Tether spacing configurations

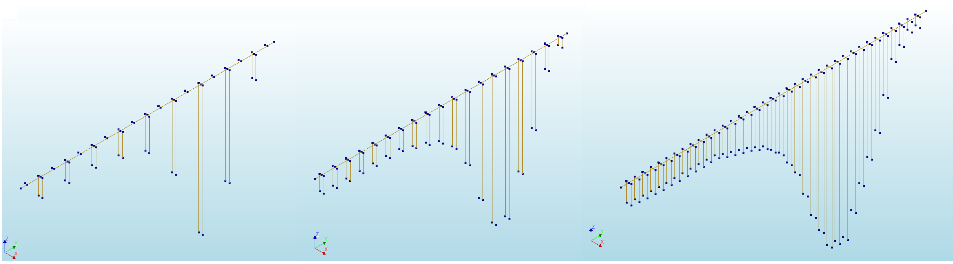

Figure 6.15: FEM's for different spacing configurations

Table 6.1: dimensions tethers per spacing configuration

△L	diameter [m]	thickness [m]	cross-sectional Area [m]^2
50	0.75	0.045	0.11
100	0.75	0.1	0.20
200	0.75	0.26	0.40

6.4.1. Results Eigenvalue analysis

The eigenperiods for the different eigenmode directions show that adjusting the number of tethers has no effect on the modes in both horizontal and normal direction. It does show an increase of eigenperiods for the vertical modes. As fewer tethers are added to the tunnel elements, the tunnel may have more flexibility in the vertical direction and so the vertical eigenperiods of the tunnel are expected to increase for increasing spacing. As for tethers, even with the different cross-sectional areas, the fundamental eigenperiods do not change as the ratio tension force / cross-sectional area remains equal.

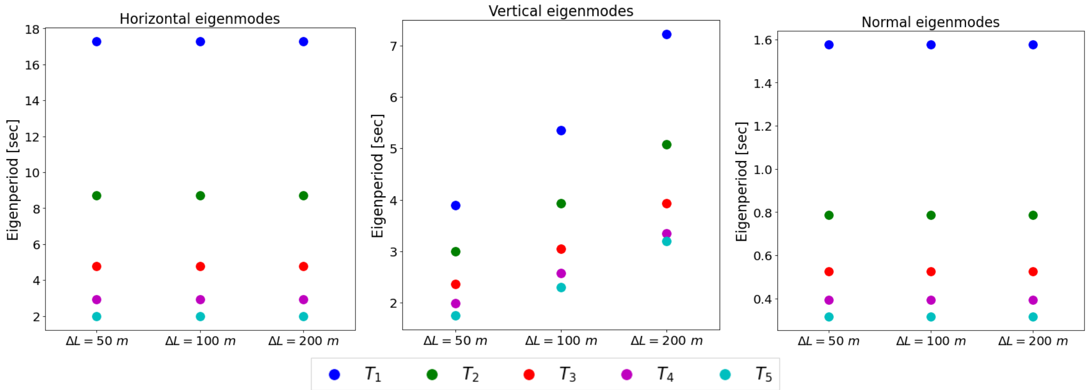

Figure 6.16: Resulting eigenperiods for tunnel per tether spacing

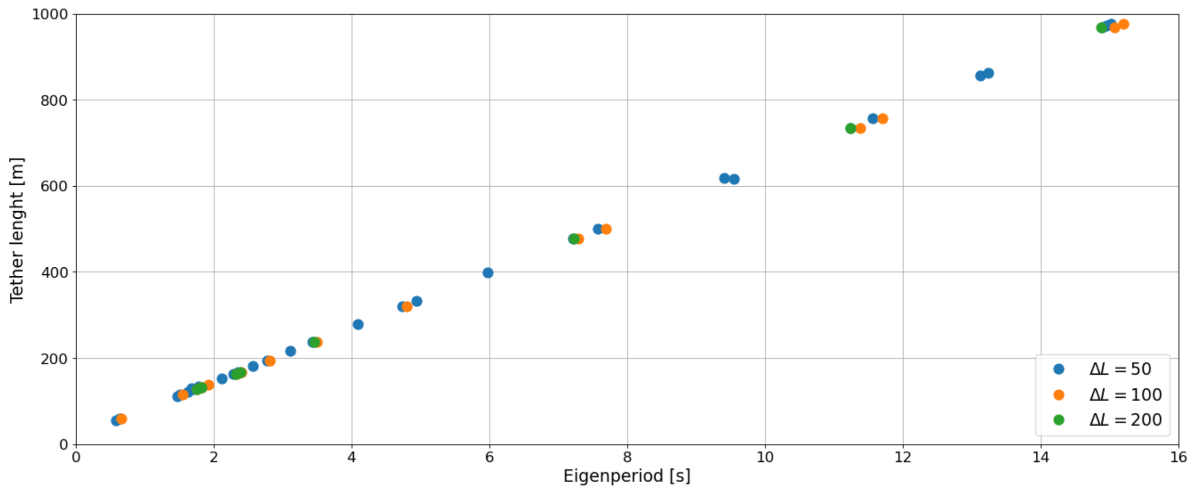

Figure 6.17: Eigenperiod tethers per spacing

6.4.2. Results Time-History analysis

Stresses tunnel elements

Looking at the resulting tensile stresses in the tunnel it is clear to see that the number of tethers attached to the SFT does not affect the seismic response of the structure (given that the same tensile stress is preserved). Figure 6.18 shows that with the different spacing applied the seismic response stays the exact same. As was explained in the previous chapter, the tethers are highly flexible and are relatively low in mass compared with the tunnel elements. As this flexibility is high, the seismic activity may result in large deformations (see section 5.5.2) but the stresses remain mostly unaffected. The large difference in mass results in a negligible effect of these tethers on the tunnel elements which is again shown in these different configurations.

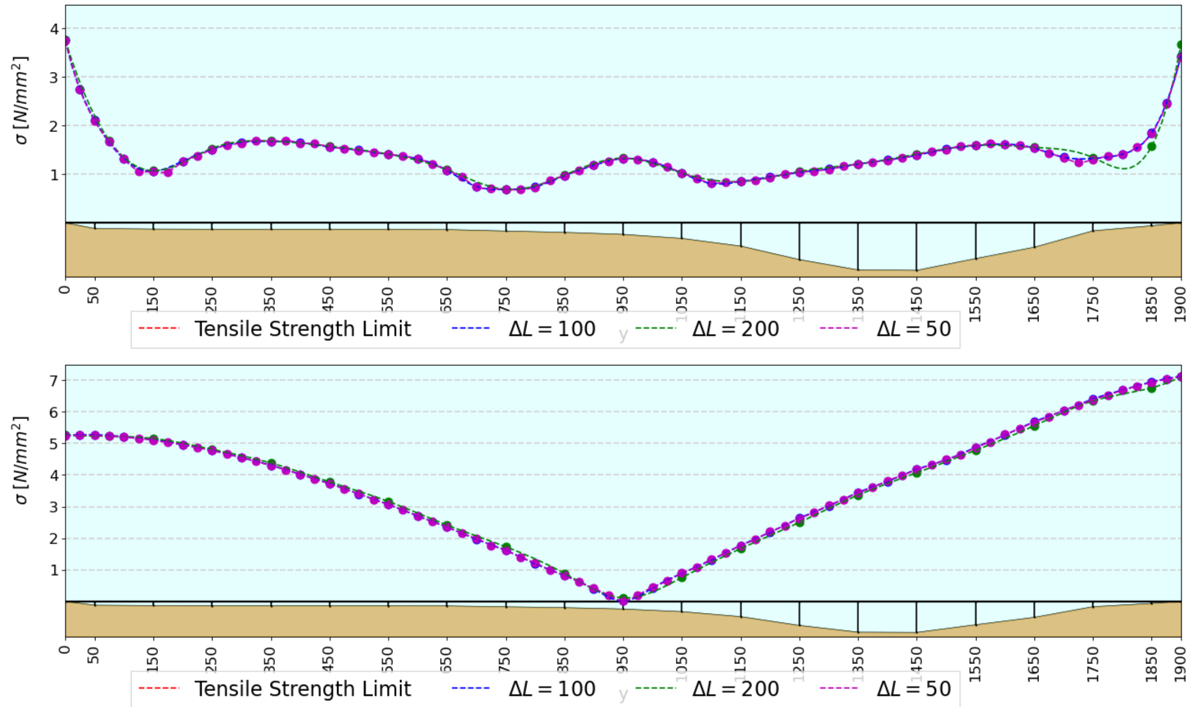

Figure 6.18: Results different tether spacing for transverse (top) and longitudinal input motion (bot) (lines overlap)

Stresses tethers

The tensile stresses in the tether presented below show minimal differences as well for the different spacing and so it can be concluded that the spacing does not effect these as well for same reason as explained in the previous section.

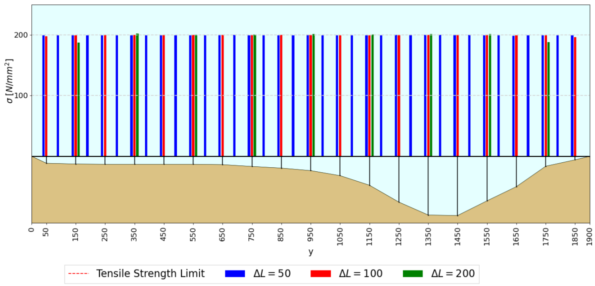

(a) Minimum tensile stresses transverse input motion

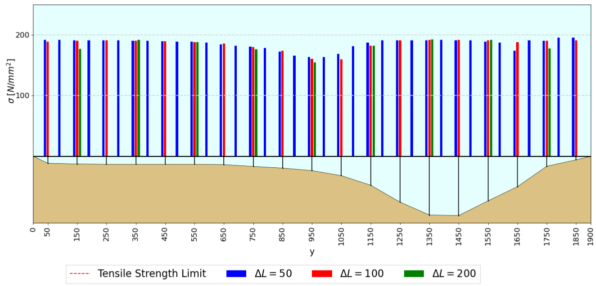

(b) Minimum tensile stresses longitudinal input motion

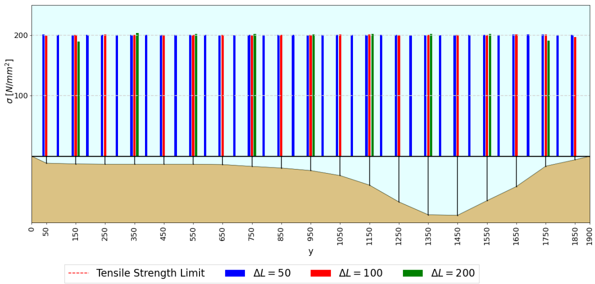

(c) Maximum tensile stresses transverse input motion

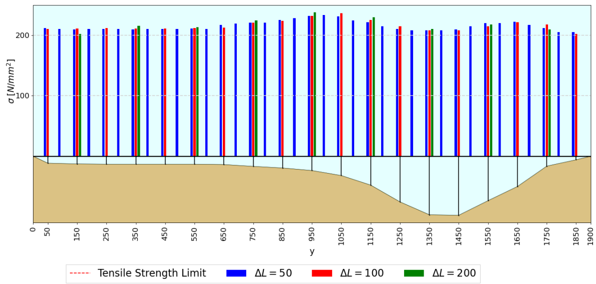

(d) Maximum tensile stresses longitudinal input motion

Figure 6.19: Tensile stresses tethers for different inclination angles

Displacements tunnel element

Ultimately, the tunnel displacement for the different tether configurations. Again no differences are found for these configurations. It is noted that as for these horizontal input motions, no differences are obtained in any of the results. This will most likely differ for the vertical input motions as the spacing does affect the eigenmodes in the vertical direction. Applying a smaller spacing (and so more tethers) would most like reduce the vertical displacement induces by the vertical input motions but may also increase the stresses in the tunnel and tethers. This would be a point of interest for further studies.

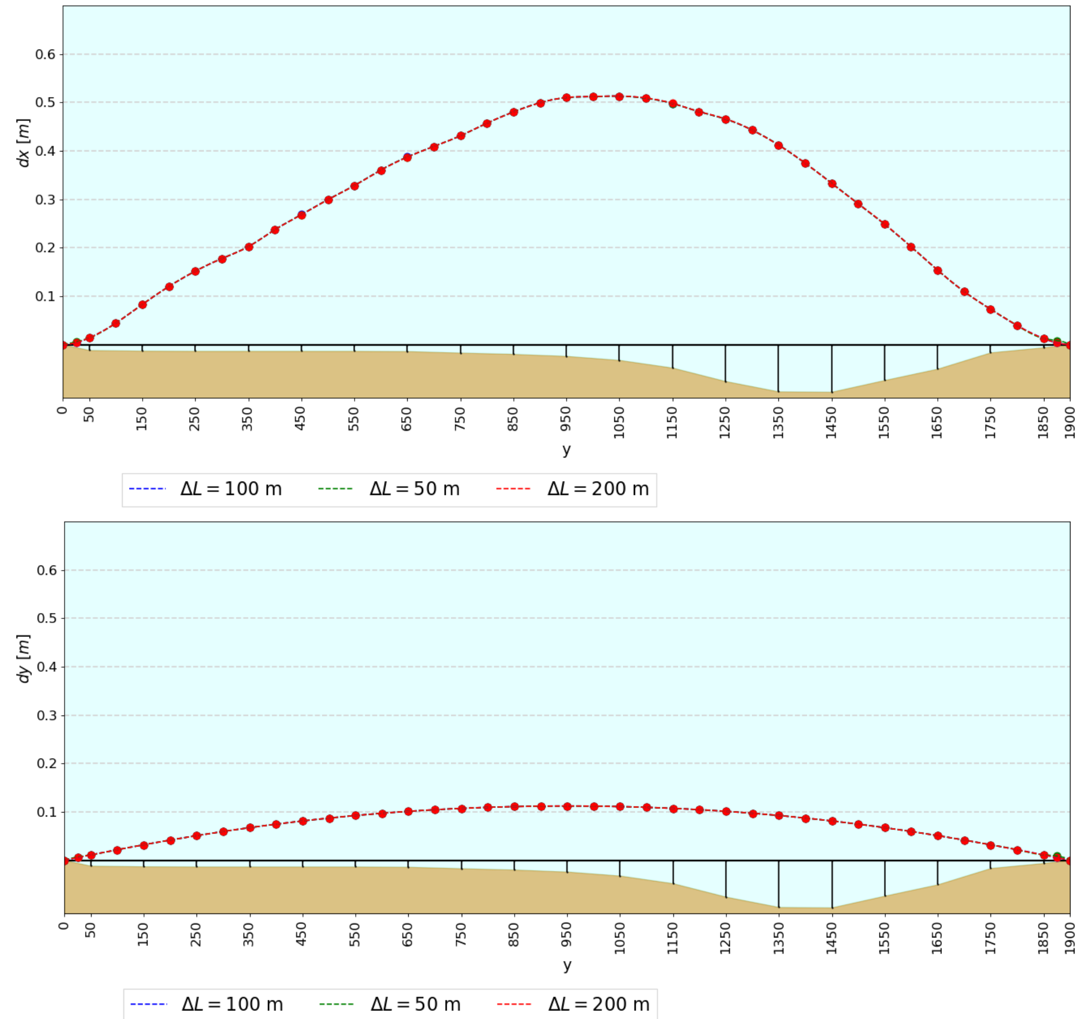

Figure 6.20: Displacements for different tether spacing for transverse (top) and longitudinal input motion (bot) (lines overlap)

Conclusion

As was stated multiple times already, it seems that the tethers have no effect on the seismic response of the tunnel due to horizontal input motions. As their flexibility is large and their mass low (compared with the tunnel elements) they have little to no influence on the behaviour of the tunnel elements. It is expected that they do affect the tunnel behaviour for vertical input motions.

6.5. tunnel alignment

So far only a straight alignment of the tunnel has been evaluated. It was found that for concrete bridges, a curved deck is more vulnerable to an earthquakes than a straight bridge deck (Banerjee et al. 2017 [6]). This results from the irregular geometry which leads to in-plane deck rotations which causes increased momentum. To verify whether this holds for the SFT as well, an s-shaped tunnel alignment as shown in figure 6.21 is applied to the FEM.

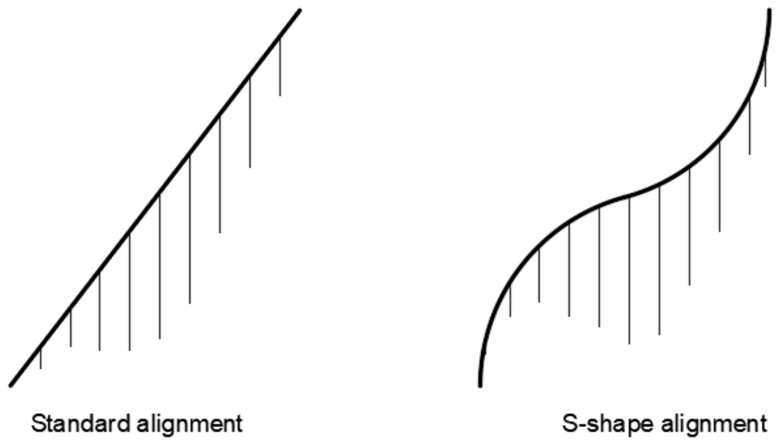

Figure 6.21: Tunnel alignments

To obtain the s-shape alignment two successive arcs are added with both an arc angle of $45°$ and a radius of $R = 1250\ m$. Figure 6.22 shows the configuration of these arcs. As the arcs are added, the total length of the tunnel is slightly increased resulting in a larger spacing and so larger tension forces in the tethers. To obtain the same initial tensile stress in the elements, the thickness of the tether applied in the model is slightly increased as well. The rest of the model and the methodology remain unchanged.

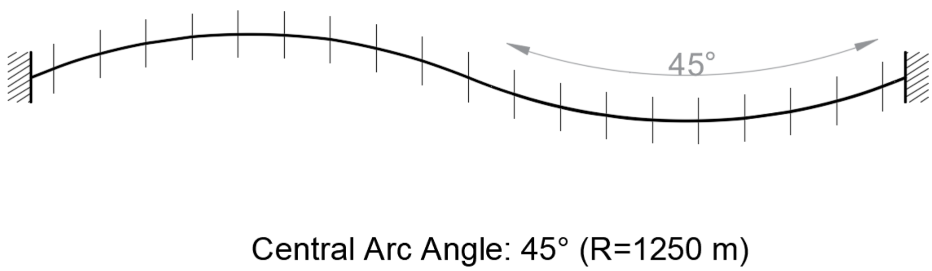

Figure 6.22: Dimensions of curvature (topview)

6.5.1. Results

6.5.2. Results Eigenvalue analysis

Since the s-shaped alignment does not have a continuous alignment with the main axis, it's hard to distinguish the different eigenmodes in the normal and horizontal directions. For that reason, all resulting eigenmodes in the x-y plane have been adopted as horizontal and compared with both horizontal and normal eigenmodes of the straight alignment. The results shown in figure 6.23 show a small increase of the eigenperiods for the s-shaped SFT. This is due to the increased tunnel length and spacing which makes the whole structure more flexible. The eigenperiods of the tethers (figure 6.31) show a small increase as well which comes from small deviations of the applied tensile stress which results from an increasing spacing due to the curvature.

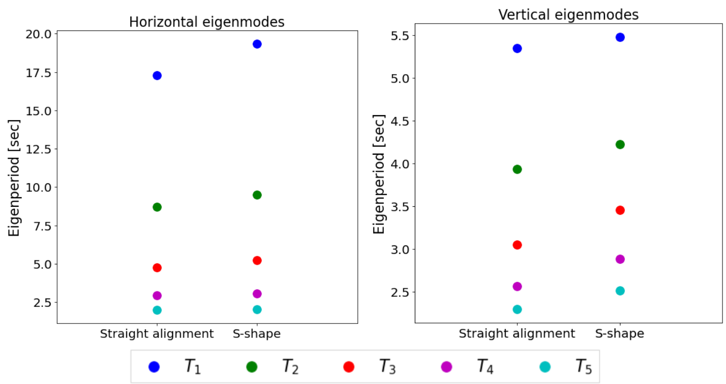

Figure 6.23: Resulting eigenperiods for straight alignment and an s-shaped alignment

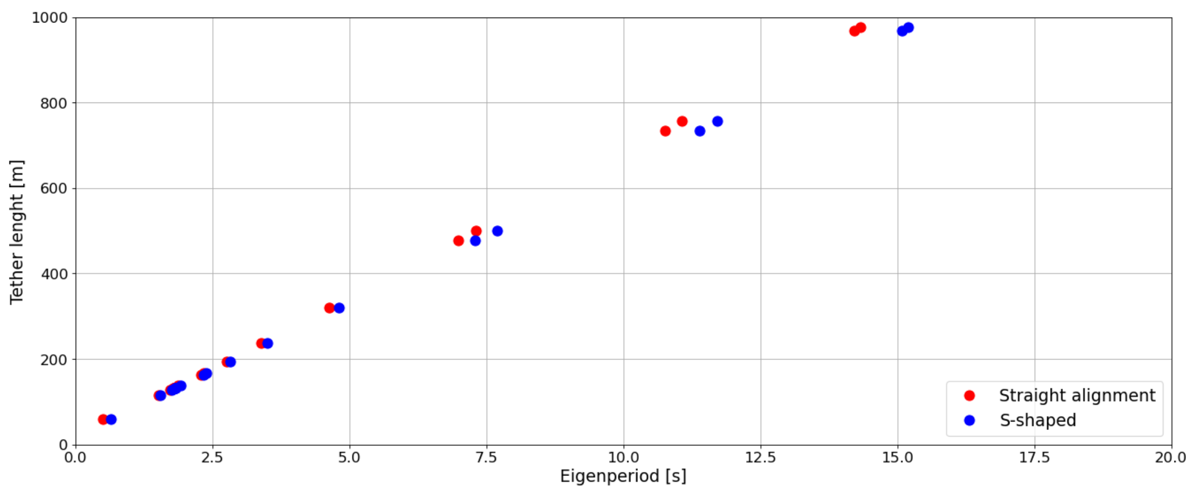

Figure 6.24: Eigenperiods tethers for straight alignment and an s-shaped alignment

6.5.3. Results Time-History analysis

Stresses tunnel elements

The effect of the input motion shows that for the s-shaped SFT, the tensile stresses do slightly increase. Looking at the effect of the longitudinal input motion, the largest increases occur at the land connections and mid-span. At these locations, the tangent of the arc deviates most of the direction of the seismic input and so are in the in-plane rotations expected to be the highest at these locations. This results in larger bending moments and so larger stresses.

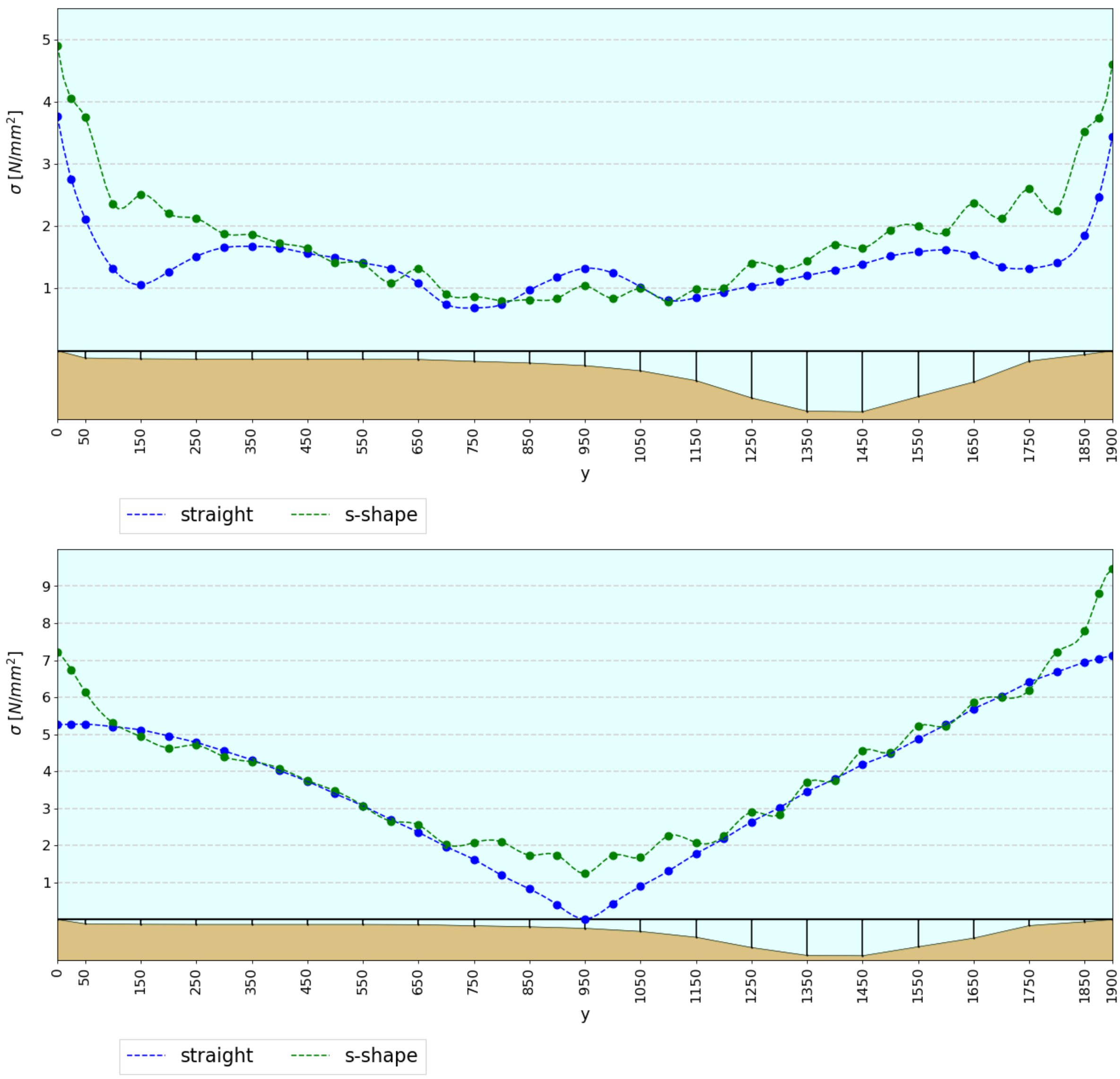

Figure 6.25: Results tunnel alignments for transverse (top) and longitudinal input motion (bot)

Stresses tethers

As the s-shape SFT has a slightly larger flexibility, the displacements of the top ends of the tethers are less restraint in there movements. This results in slightly smaller deviations from the initial tether stress is can be seen in the figure below.

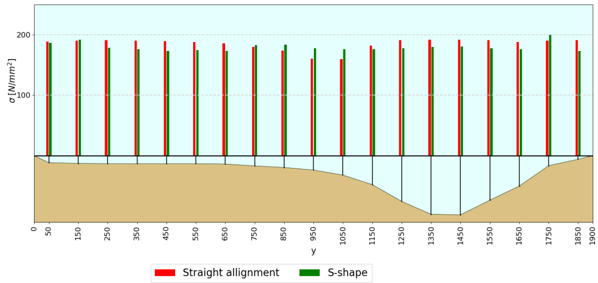

(a) Minimum tensile stresses transverse input motion

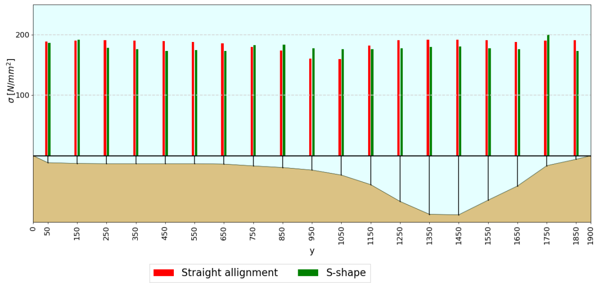

(b) Minimum tensile stresses longitudinal input motion

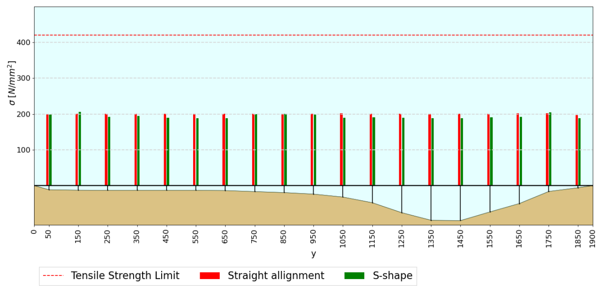

(c) Maximum tensile stresses transverse input motion

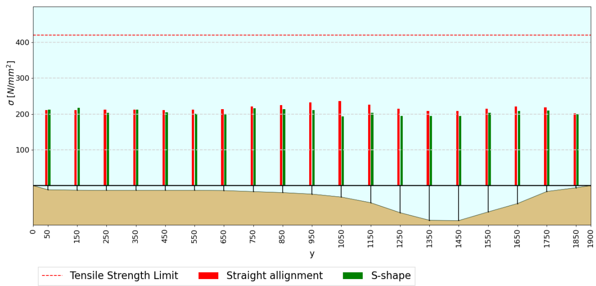

(d) Maximum tensile stresses longitudinal input motion

Figure 6.26: Tensile stresses tethers for different tunnel alignments

Displacements tunnel element

In all the previous configurations studied, the longitudinal displacement due to transverse input motion and the transverse displacement due to longitudinal displacement remain zero throughout the analysis. By applying a curved alignment, deflections orthogonal to the input direction do occur as the different sections of the tunnel are now orientated differently with respect to the input direction. Overall the displacements of the tunnel seem to have increased slightly. For the straight alignment, pure axial forces occur which led to large stresses as the axial freedom was limited. For the curved alignment, these pure axial forces do not occur due to the geometry and so larger displacements are obtainable.

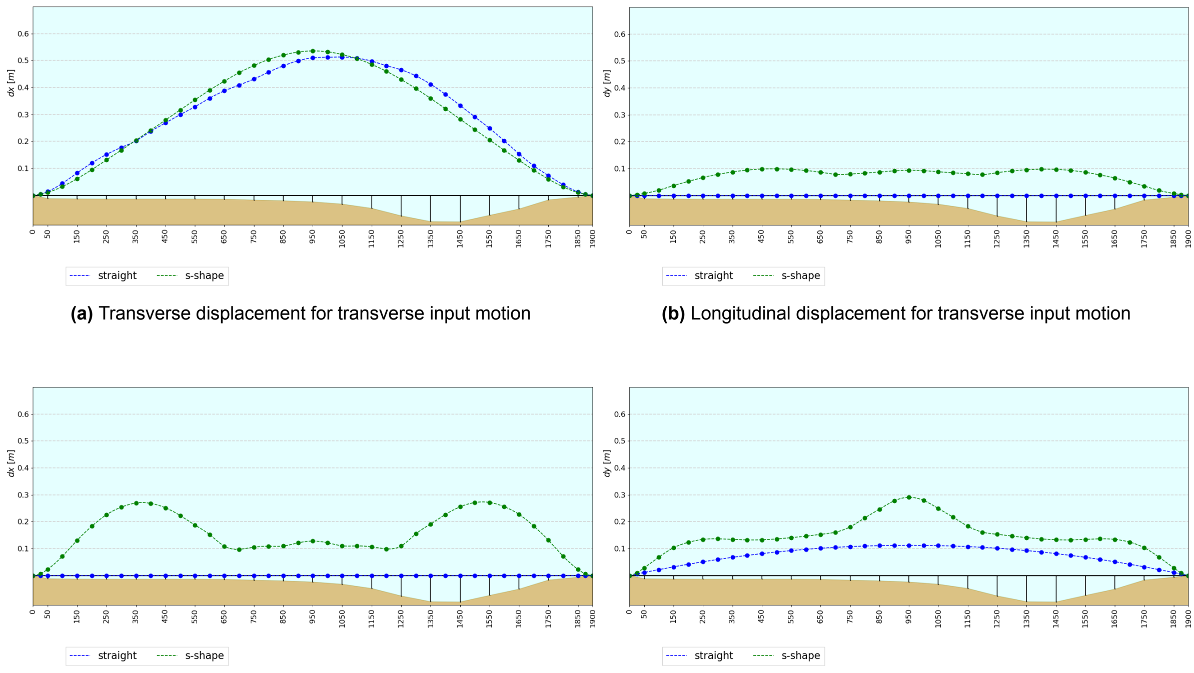

(a) Transverse displacement for transverse input motion

(b) Longitudinal displacement for transverse input motion

(c) Transverse displacement for longitudinal input motion

(d) Longitudinal displacement for longitudinal input motion

Figure 6.27: Displacements for different tunnel alignments

Conclusion

The s-shape alignment results in a slightly more flexible construction. Due to the bending capacity of the concrete, the tunnel can deform a bit more in the longitudinal direction than it can with a straight alignment. This larger flexibility is also traced back to the lowered effect on the tether stresses for the longitudinal input motion. The irregular geometry does result in an increase of tunnel stresses which is likely to occur due to in-plane rotations of certain elements compared with the rest of the tunnel.

6.6. Base isolation systems

Base isolation systems (BIS) are a commonly applied tool in seismic engineering. The main idea of these systems is to decouple the structure from the foundation. These elements are added to the foundations of the structure and are there to 'absorb' the seismic energy coming from the excited soil. A BIS may consist of a foundation block consisting of multiple layers of rubber which are reinforced with steel elements as figure 6.28 displays.

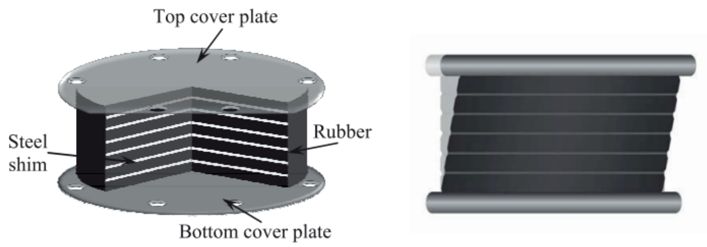

Figure 6.28: Example of a base isolation system [29]

The design of these systems is such that when a seismic excitation reaches the foundation of the structure, the energy first reaches the BIS. Here the energy is translated in a displacement of the BIS. The BIS dampens the motions such that when the energy of the seismic wave reaches the top cover plate (where the structure is located) most of the energy has been depleted and so a lot of seismic energy has been withheld from the structure.

Originally BIS are applied to short-period structures (e.g. low-rise buildings). The eigenperiods of these kinds of structures are much smaller than those of the long, flexible structures such as the SFT studied here. Looking at the response spectra of most seismic events, the higher values are found in short period regions (periods smaller than 0.5 s) and as the period increases smaller response values are found. At $T = 4$ s, already relatively low responses are found and so continuing to much higher eigenvalues only brings even lower responses. Therefore applying a BIS to a short period structure is much more effective as this may shift the fundamental eigenperiods from the peak response values to more intermediate values whereas for long-flexible structure, shifting the already high eigenperiods to even higher periods doesn't add much in lowering the seismic response.

Yet, the effect of applying a BIS does not only result in a period elongation but also a reduction of the axial stiffness. Studies were performed on the effect of BIS for long-period structures (Anajafi et al. (2020) [19]) where the effect of a BIS applied to a long-span bridge was tested. The results show that, even for these long-period structures, a BIS significantly reduce the seismic response but also resulted in larger displacements of the deck. As the tunnel tensile stresses found previously were mainly due to the axial stiffness of the structure, it is of interest to see how these systems affect the SFT.

To do so first, the supports of the tunnel ends in the longitudinal direction are removed. Subsequently, springs are added to the system which are applied at the tunnel ends in the same manner as the mooring lines were applied previously (but now orientated in the longitudinal direction). Figure 6.29 gives a schematization of how the BIS works for the SFT. As explained previously, the high normal forces were most likely due to lateral strength as the SFT was completely fixed. Adding the BIS as shown in figure 6.29 allows for damped translations in the normal direction which should release the structure from high stresses. For the stiffness of the BIS, the values as in Anajafi et al. (2020) [19] are adopted.

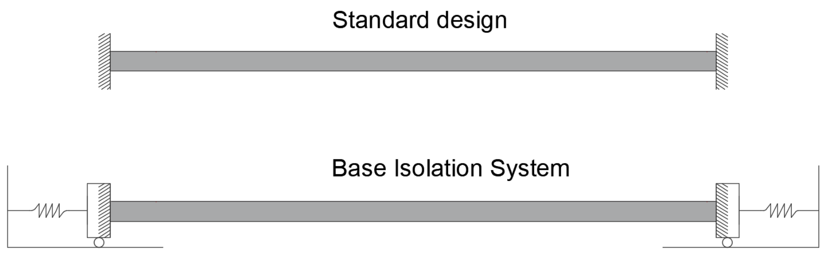

Figure 6.29: Schematization of base isolation system

6.6.1. Results Eigenvalue analysis

Figures 6.30 and 6.31 show the resulting eigenperiods of the tunnel elements and the tethers. The results of the tunnel elements show a large reduction of the axial stiffness as the eigenmodes in the normal direction of the isolated system has increased drastically. The eigenperiods of the other directions and those of the tethers remain unchanged.

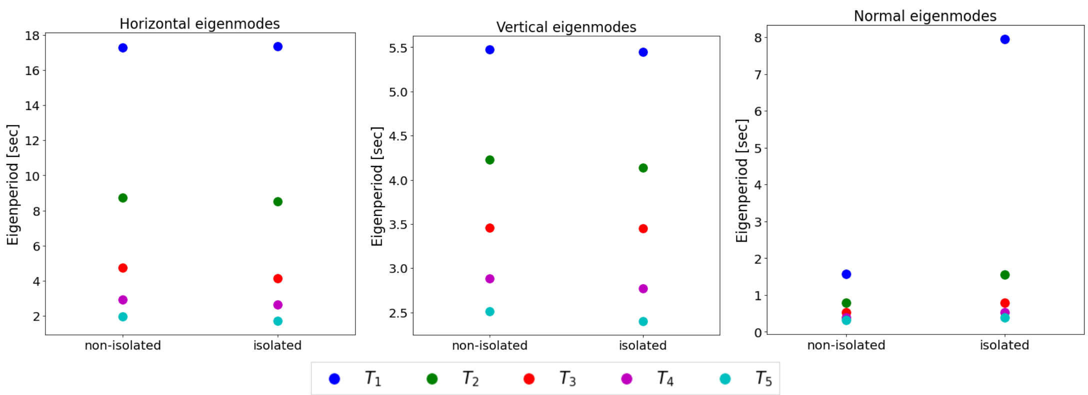

Figure 6.30: Resulting eigenperiods tunnel elements for for isolated and non-isolated

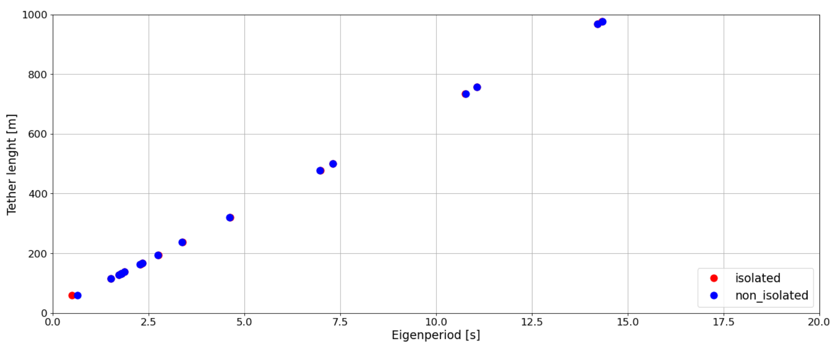

Figure 6.31: Eigenperiods tethers for isolated and non-isolated

6.6.2. Results Time-History analysis

Stresses tunnel elements

As has been done for all previous sections, again the effect of the input motion on the tunnel stresses is shown. For the transverse input motion, no significant differences are found. As the BIS only affects the stiffness of the structure in the longitudinal direction it is as expected these results remain mostly unchanged. The results of the longitudinal input motion do show a significant effect of the BIS as the tensile stresses are highly reduced. This is the result of the added flexibility in the normal direction provided by the BIS.

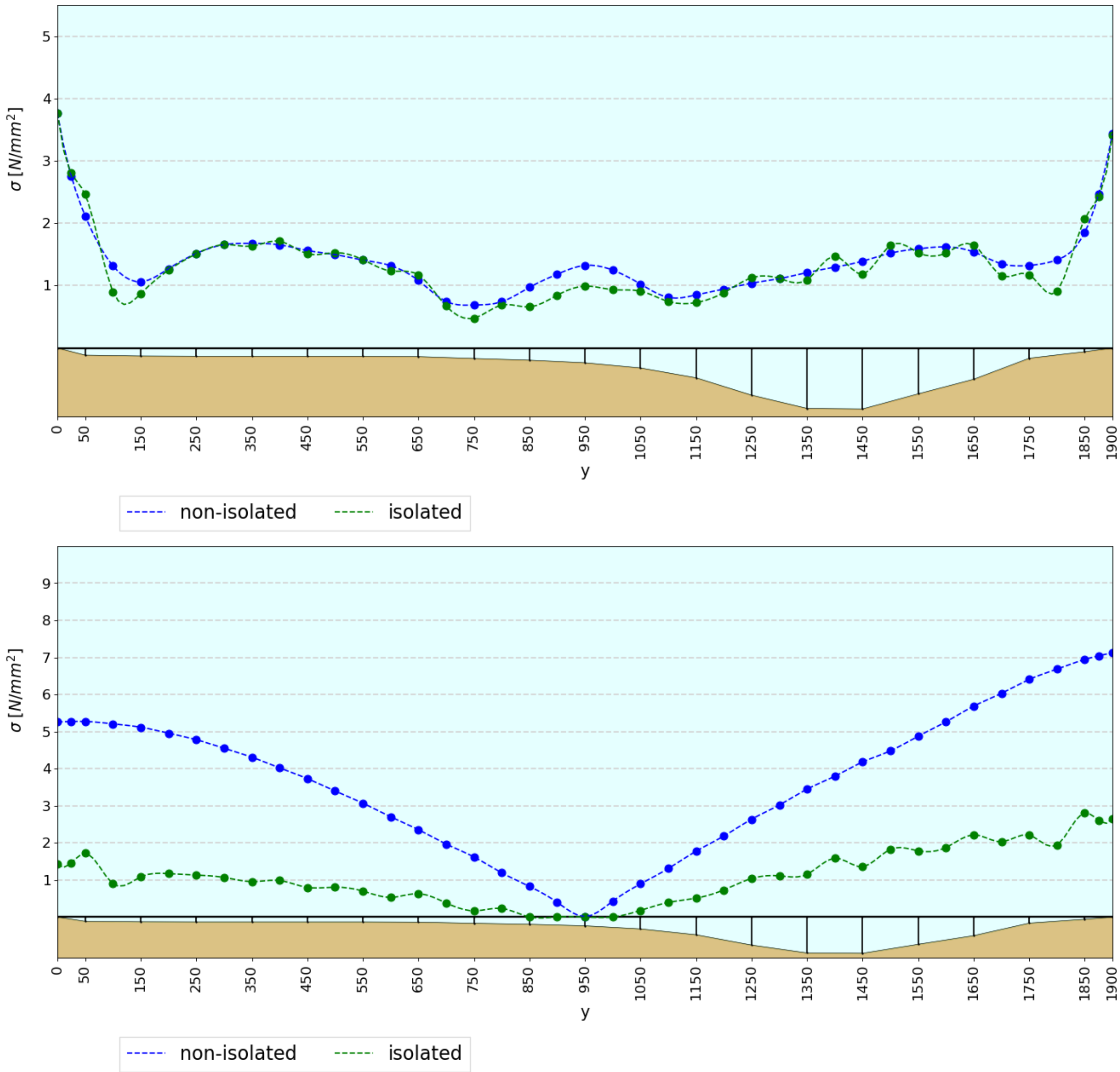

Figure 6.32: Results BIS for transverse (top) and longitudinal input motion (bot)

Stresses tethers

The tensile stresses of the tethers show that by gaining more flexibility in the normal direction, the effect on the tethers is slightly lowered. The same behaviour was found for the analysis made for the curved tunnel alignment. The result of the transverse input motions remains unchanged.

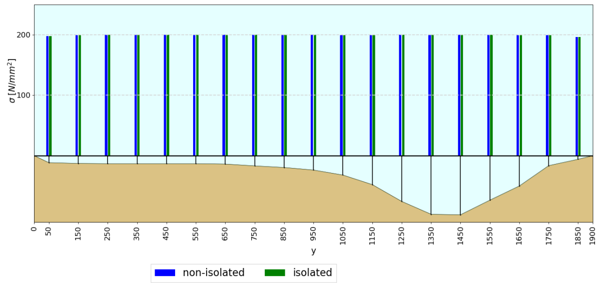

(a) Minimum tensile stresses transverse input motion

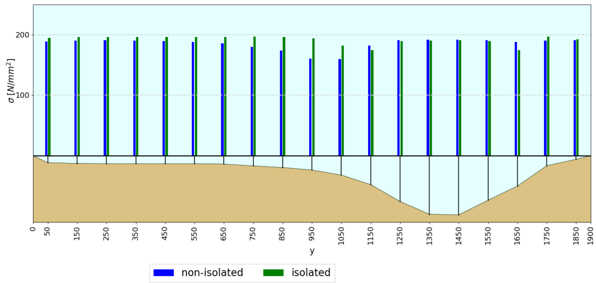

(b) Minimum tensile stresses longitudinal input motion

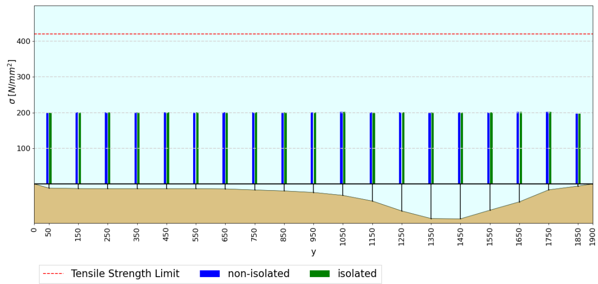

(c) Maximum tensile stresses transverse input motion

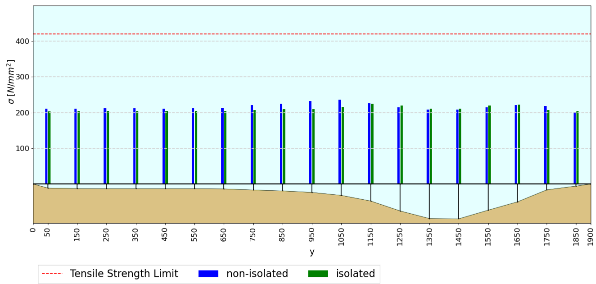

(d) Maximum tensile stresses longitudinal input motion

Figure 6.33: Tensile stresses tethers with and without BIS

Displacements tunnel elements
As applying a BIS may result in lowered stresses, it does come at the cost of higher displacements. Figure 6.34 provides the transverse and longitudinal displacements with and without the use of base isolation. Where the transverse displacements are not changed, the longitudinal displacements do show an increase over the total tunnel length. Overall the displacements remain limited and so applying base isolation seems to be highly efficient in lowering the seismic response of the SFT.

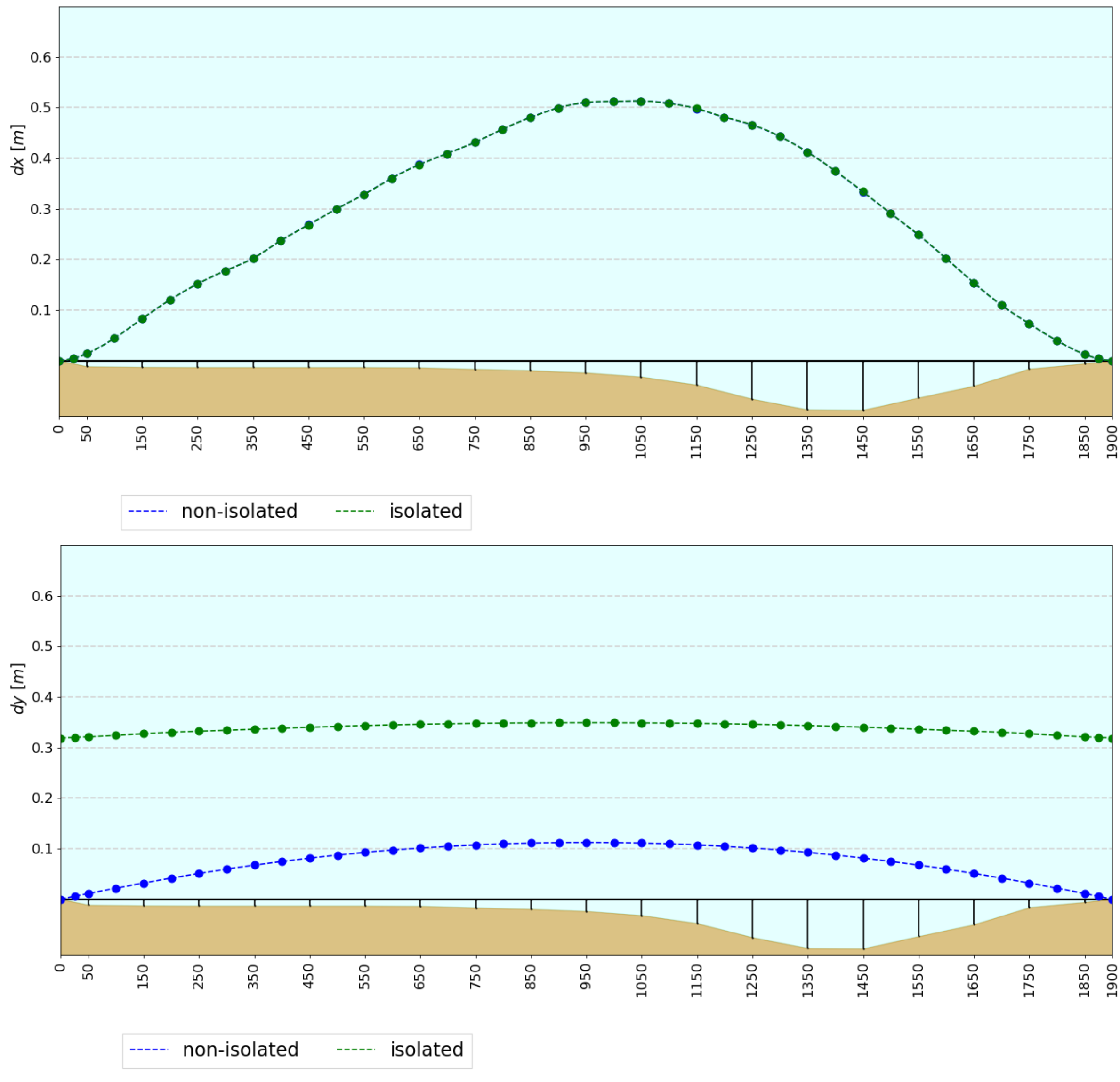

Figure 6.34: Resulting eigenperiods tunnel elements for for isolated and non-isolated

Conclusion
Applying BIS is shown to be largely effective in reducing the seismic forcing. As stated previously, the stress development in the tunnel is mostly due to the fully clamped fixations of the outer ends which results in stiff connections. Applying BIS reduces this stiffness and so lowers the resulting tunnel stresses. As the reduction of the stiffness (here only applied in the axial direction) results directly in an increased flexibility, the longitudinal deformations of the tunnel increase as well.

6.7. Conclusion

In this chapter multiple design changes were tested on the seismic performance and how they affect the eigenvalues of the system and the tensile stresses in the tunnel elements and tethers. It was found that:

1. The mooring lines and vertical tethers have little to no added value on the seismic response of the SFT for horizontal input motions. As the stiffness of the sagged mooring lines is not high enough to restrain the tunnel in the horizontal direction and the vertical tethers are too flexible in the transverse direction, altering the number of mooring lines or vertical tethers show no significant differences in the resulting tensile stresses;
2. Inclining the tethers does result in larger oscillations of the tensile stresses for transverse input motion. Lowering the inclination angle results in larger effects of the input motion. The already relatively low tunnel stresses for transverse input motions aren't altered much by these inclined tethers. The transverse displacement is of the tunnel is does decrease by lowering the inclination angle. Applying an angle of $70°$ lowers the maximum displacement by 32%, for an angle of $45°$ a decrease of 37% is found. For the response in the longitudinal direction, inclining the tethers (inclined in the transverse direction) have no effect;
3. A straight tunnel alignment is most beneficial for the seismic response. Having a curved alignment causes additional forces and bending moments due to the irregular geometry. Curved alignments also result in larger (longitudinal) displacements as the flexibility is slightly increased;
4. Applying base isolation to the tunnel is highly effective in reducing the seismic response for the longitudinal input motion where a lowering of 60% is found for the tunnel tensile stresses. Applying base isolation does result in larger deformations in the normal direction which were found to increase by 212%. For the transverse input motions, the BIS as applied in this study has no noticeable effect.

7

Conclusion, Discussion and Recommendations

This final chapter presents the conclusion which can be drawn from the findings of this study. This main- and sub-question as described in chapter 1 will be covered after which a discussion is presented in where the assumptions made in this study and the consequences of these are evaluated. Finally, a recommendation is given for further studies.

7.1. Conclusion

The aim of this study was to gain a better understanding of the dynamic behaviour of an SFT during a seismic attack. A finite element model was made to study this behaviour. The conclusions drawn from this study are presented here along with the main research questions. In these conclusions, the sub-questions are covered as well.

1) How can the dynamic response of an SFT due to earthquakes be modeled?

- An simplified Finite Element Model for the seismic analysis of the SFT has been created in a 3D environment which was found to be sufficiently accurate with the analytical model which was based on the frequency domain method of analysis and the application of the Euler-Bernoulli beam;
- With the use of the simplified model, the entire tunnel was modeled with which the eigenvalue analysis and the seismic analysis for the entire structure were performed;
- The effect of the surrounding water is implemented with the use of a modified Morison equation where the effect of the elements moving through the water is evaluated with a drag and an inertia force;
- Horizontal input motions were applied in both the transverse as the longitudinal direction after which the tensile stresses in both tunnel elements as in the tethers were evaluated along with the displacements of the tunnel

2) How does the SFT behave during an earthquake and how can the design be altered to reduce the dynamic response?

- The result of the eigenvalue analysis showed a linear relation between the tether length and the eigenperiods of these tethers. As the length increases so do the eigenperiods and so does a larger tether length result in a higher flexibility of these elements.
- For the tunnel, the resulting eigenperiods were subdivided per eigenmode. Eigenmodes with the deflection in transversal direction, vertical direction and normal direction. The eigenperiods

of those corresponding with the transversal direction were by far the highest. This tells that the tunnel has a large flexibility in the transverse direction. The second largest where those of the vertical eigenmodes as these deformations are more limited due to the vertical tethers. The lowest eigenperiods were those of the normal direction. For these, the flexibility is limited as the tunnel was fully clamped out both outer ends.

- Comparing the eigenperiods with the values of the response spectra of the input signals showed that most of the fundamental eigenperiods were far from the peak values of these spectra. This suggests that the seismic input has a limited effect on the SFT.
- For the time-history analyses, two types of analyses were performed. One with the input motions in the transversal direction and one in the longitudinal direction. The transversal input motions had a limited effect on the SFT. As the transversal flexibility of the SFT is relatively high, larger deformations of the tunnel and tethers were found (compared with the longitudinal results). The stresses in the tunnel remain limited and were mostly due to the input motions coming from the land tunnel connection.
- Longitudinal input motions were found to be slightly more critical than the transversal direction. The motions had a larger effect on the tunnel tensile stresses due to the higher axial stiffness of the structure. Due to this axial stiffness, longitudinal displacements are lower compared with the transversal results.
- For both input directions, the tethers have a limited effect on the tunnel stresses. The stresses in the tethers self were found to be more affected by the longitudinal input motions due to the limited flexibility of the tunnel in this direction. Yet, for both the seismic impact remain limited.
- Different configurations have been analyzed regarding the mooring lines and tethers. Applying more or less mooring lines to the system does not affect the tensile stresses in both the tunnel and in the tethers. Increasing the amount of mooring lines does result in smaller deformations. The vertical tethers have a negligible effect on the seismic behaviour for the horizontal input motions. Inclining the tethers results in larger tensile stresses in these elements but also reduces the displacements of the tunnel;
- Straight tunnel alignments are found to be more beneficial for the seismic response compared with curved alignment. Curved alignments introduce increased bending moments which results in larger tensile stresses;
- The application of base isolation was found to be highly effective in lowering the response for longitudinal input motions. The use of such a system does result in larger normal deformations.

7.2. Discussion

Throughout this study, some assumptions and simplifications have been made. This section discusses the effect of these and how they may have had an influence on the conclusion drawn previously.

- The effect that the water has on the SFT has been evaluated by applying a linearized Morison's equation. Appendix C provides a sensitivity study regarding this linearization of the damping part of this equation. Here, small deviations of the input value do result in significantly altering results. It is therefore presumable that this linearization has affected the results of this study. To gain insights into how much this effect is, a non-linear analysis could be performed for comparison.
- All analyses performed for the design options in chapter 6 were based on uniform excitations. Section 5.6 showed that applying the wave passage effect, and so a non-uniform excitation, largely increases the resulting tunnel stresses. Therefore it can be expected that the results shown for the longitudinal input motions are more conservative.
- When defining the lower boundary of the acceptable tension in the tethers, the criteria was only based on slack or not. Lowering the tension in the tethers may introduce a non-linear behaviour in these which may have a negative effect on the SFT as well which is not examined in this study.
- For the model made in DIANA, the tunnel elements are described as a singular beam element. In reality, the SFT would consist of multiple tunnel elements which are connected by joints (located

between the tunnel elements and between the tunnel elements and land tunnel at the outer ends). These joints are more flexible than the continuous beam and so the dynamic behaviour of such a system could differ from the model made here.

- For all seismic analyses made in this study, only one input direction was applied. For real seismic events, the input motion would consist of 3 components (north-south, east-west and vertical) which would all act simultaneously. Applying only one direction would therefore diminish the effect of the seismic attack.
- The input signals applied for the seismic wave were all the same with only a delay in the starting time. Normally, as the seismic wave propagated, the signal would lose its energy. Depending on the distance and the soil type(s) the signal applied would differ over space. By applying the same signal for all supports, an overestimation is made. On the other hand, as the spatial distance isn't that large and the soil uniform, this difference would not be that significant.

7.3. Recommendation

This section provides recommendations regarding future studies on seismic behaviour of SFT's

- Section 5.7.2 showed that the vertical input motions had a much larger effect on the tethers than the horizontal input motion had. It would there be of interest to examine the effect of these vertical motions in more detail and see how the different design alterations affect the response due to these. Furthermore, the vertical motions used in 5.7.2 were applied uniformly. Section 5.6 showed that applying a wave passage effect highly increases the resulting stresses and so it's recommended to apply this effect on the vertical input motions as well.
- As noted in the previous bullet point, applying the wave passage effect large increases the effect of the seismic input motions on the resulting tunnel stresses. In this study, the effect of the wave passage has only been evaluated as a subsection. Applying the effect for every longitudinal input motions analysis would result in a more realistic output. As for the propagation speed of these seismic waves, this study examined three different velocities (uniformly excitation as $v_s = \infty$). It was found that for lower propagation speeds, larger stresses are obtained in the SFT. It would be of interest to expand this study by applying more propagation speed and see if this conclusion still holds.
- The waterbody in where the SFT is situated highly affects the dynamic behaviour of the structure. In this study, the water was assumed fully stagnant and its effect on the dynamic behaviour was described by applying Morison's equation. In reality, during a seismic event, the water would not remain stagnant but, due to the (vertical) motion of the bed, compressive fluid waves would transmission from the bed which set the waterbody in motion, this phenomenon is known as a seaquake. Including this effect could alter the results of the SFT.
- The seismic response of the SFT was found to be most affected by the excitations at the land tunnel connections. This study has analyzed these connections as fully fixed and with the appliance of BIS. As the appliance of one of these connections highly affected the resulting stresses, analyzing these land tunnel connections in more detail would be of interest for future studies
- The force on the SFT may be expanded. In this study, only permanent loads and seismic loading were applied. Other loading's such as wave attack, service loads and or exceptional loads (explosions or collisions) should be studied as well.

References

[1] A. R. Abdulghany. “Generalization of parallel axis theorem for rotational inertia”. In: *American Journal of Physics* 85 (Oct. 2017), pp. 791–795. DOI: 10.1119/1.4994835.

[2] N. A. Abrahamson and R. R. Youngs. “A stable algorithm for regression analyses using the random effects model”. In: *Bulletin of the Seismological Society of America* 82.1 (Feb. 1992), pp. 505–510. ISSN: 0037-1106. DOI: 10.1785/BSSA0820010505. eprint: https://pubs.geoscienceworld.org/ssa/bssa/article-pdf/82/1/505/5340765/bssa0820010505.pdf. URL: https://doi.org/10.1785/BSSA0820010505.

[3] Ahmet Altunişik and Ebru Kalkan Okur. “Investigation of earthquake angle effect on the seismic performance of steel bridges”. In: 22 (Nov. 2016), pp. 855–874. DOI: 10.12989/scs.2016.22.4.855.

[4] Bengi Atak, Özgür Avşar, and Ahmet Yakut. “Directional Effect of the Strong Ground Motion on the Seismic Behavior of Skewed Bridges”. In: June 2014.

[5] Linda Al Atik and Norman Abrahamson. “An Improved Method for Nonstationary Spectral Matching”. In: *Earthquake Spectra* 26.3 (2010), pp. 601–617. DOI: 10.1193/1.3459159. eprint: https://doi.org/10.1193/1.3459159. URL: https://doi.org/10.1193/1.3459159.

[6] Arnab Banerjee, Avishek Chanda, and Raj Das. “Seismic analysis of a curved bridge considering deck-abutment pounding interaction: an analytical investigation on the post-impact response”. In: *Earthquake Engineering & Structural Dynamics* 46.2 (2017), pp. 267–290. DOI: https://doi.org/10.1002/eqe.2791. eprint: https://onlinelibrary.wiley.com/doi/pdf/10.1002/eqe.2791. URL: https://onlinelibrary.wiley.com/doi/abs/10.1002/eqe.2791.

[7] J. L. Bogdanoff, J. E. Goldberg, and A. J. Schiff. “The effect of ground transmission time on the response of long structures”. In: *Bulletin of the Seismological Society of America* 55.3 (June 1965), pp. 627–640. ISSN: 0037-1106. DOI: 10.1785/BSSA0550030627. eprint: https://pubs.geoscienceworld.org/ssa/bssa/article-pdf/55/3/627/5349024/bssa0550030627.pdf. URL: https://doi.org/10.1785/BSSA0550030627.

[8] *CESMD - Center for Engineering Strong Motion Data*. URL: https://www.strongmotioncenter.org/. (accessed: 04.08.2021).

[9] Wenjun Chen and Guojun Huang. “Seismic wave passage effect on dynamic response of submerged floating tunnels”. In: *Procedia Engineering* 4 (Dec. 2010), pp. 217–224. DOI: 10.1016/j.proeng.2010.08.025.

[10] DIANA FEA BV. *DIANA Documentation release 10.4*. Version 2019. Delft, 2020. URL: https://dianafea.com/.

[11] *Eurocode 8: Design provisions for earthquake resistance of structures : part. 1-3 : General rules, specific rules for various materials and element*. Merged with DD-ENV-1998-1-1 and DD-ENV-1998-1-2 into prEN-1998-1. London: BSI, 1996. URL: https://cds.cern.ch/record/848046.

[12] Guanghai Gao, Yunjing Cui, and Xingqi Qiu. “Prediction of Vortex-Induced Vibration Response of Deep Sea Top-Tensioned Riser in Sheared Flow Considering Parametric Excitations”. In: *Polish Maritime Research* 27.2 (2020), pp. 48–57. DOI: doi:10.2478/pomr-2020-0026. URL: https://doi.org/10.2478/pomr-2020-0026.

[13] S.J. Garrett. “Chapter 13 - Introductory Numerical Methods”. In: *Introduction to Actuarial and Financial Mathematical Methods*. Ed. by S.J. Garrett. San Diego: Academic Press, 2015, pp. 411–463. ISBN: 978-0-12-800156-1. DOI: https://doi.org/10.1016/B978-0-12-800156-1.00013-3. URL: https://www.sciencedirect.com/science/article/pii/B9780128001561000133.

[14] Wang Guobo et al. “Numerical Study on the Seismic Response of Structure with Consideration of the Behavior of Base Mat Uplift”. In: *Shock and Vibration* 2017 (Oct. 2017), pp. 1–19. DOI: 10.1155/2017/2030462.

[15] JONATHAN HANCOCK et al. “An Improved Method Of Matching Response Spectra of Recorded Earthquake Ground Motions Using Wavelets”. In: *Journal of Earthquake Engineering - J EARTHQU ENG* 10 (Jan. 2006), pp. 67–89. DOI: 10.1080/13632460609350629.

[16] Mart-Jan Hemel. “Submerged floating tunnel: The dynamic response due to fluid structure interaction”. In: (Oct. 2019). URL: http://resolver.tudelft.nl/uuid:49f508ae-20a3-4cf4-a99b-e609fa6e2c81.

[17] Maplesoft, a division of Waterloo Maple Inc.. *Maple*. Version 2019. Waterloo, Ontario, 2019. URL: https://hadoop.apache.org.

[18] A.V. Metrikine. *Lecture notes Dynamics, Slender Structures and an Introduction to Continuum Mechanics*. Technical University Delft, 2006.

[19] Mahmood Minavand and Mohsen Ghafory-Ashtiany. “Seismic Evaluation of Horizontally Curved Bridges Subjected to Near-Field Ground Motions”. In: *Latin American Journal of Solids and Structures* 16 (Mar. 2019). DOI: 10.1590/1679-78255438.

[20] Arvid Naess and Torgeir Moan. *Stochastic Dynamics of Marine Structures*. Cambridge University Press, 2012. DOI: 10.1017/CBO9781139021364.

[21] John Oluwafemi et al. “Review of world earthquakes”. In: *International Journal of Civil Engineering and Technology* 9 (Sept. 2018), pp. 440–464.

[22] Charaf Ouled Housseine, Charles Monroy, and Guillaume de Hauteclocque. “Stochastic Linearization of the Morison Equation Applied to an Offshore Wind Turbine”. In: June 2015. DOI: 10.1115/OMAE2015-41301.

[23] Peng Pan, Tao Wang, and Masayoshi Nakashima. “Chapter 3 - Time Integration Algorithms for the Online Hybrid Test”. In: *Development of Online Hybrid Testing*. Ed. by Peng Pan, Tao Wang, and Masayoshi Nakashima. Butterworth-Heinemann, 2016, pp. 27–55. ISBN: 978-0-12-803378-4. DOI: https://doi.org/10.1016/B978-0-12-803378-4.00003-0. URL: https://www.sciencedirect.com/science/article/pii/B9780128033784000030.

[24] D. Peters. *Tuiconstructies, constructief gedrag en optimalisering*. Rijswijk: TNO-Prins Maurits Laboratorium, 1993.

[25] Jerome M. Raphael. “Tensile Strength of Concrete”. In: 1984.

[26] *Seismosoft [2021] ”SeismoMatch 2021 – A computer program for spectrum matching of earthquake records,”*. URL: http://www.seismosoft.com.

[27] Bipin Shrestha. “Seismic response of long span cable-stayed bridge to near-fault vertical ground motions”. In: *KSCE Journal of Civil Engineering* 19 (June 2014). DOI: 10.1007/s12205-014-0214-y.

[28] *EN 1992-1-1 Eurocode 2: Design of concrete structures - Part 1-1: General ruels and rules for buildings*. EN. Brussels: CEN, 2005.

[29] A. Tsouvalas. *Lecture notes Structural Response to Earthquakes*. Technical University Delft, 2019.

[30] Deokhee Won et al. “Hydrodynamic Behavior of Submerged Floating Tunnels with Suspension Cables and Towers under Irregular Waves”. In: *Applied Sciences* 9.24 (2019). ISSN: 2076-3417. DOI: 10.3390/app9245494. URL: https://www.mdpi.com/2076-3417/9/24/5494.

[31] Zhiwen Wu, Pengpeng Ni, and Guoxiong Mei. “Vibration response of cable for submerged floating tunnel under simultaneous hydrodynamic force and earthquake excitations”. In: *Advances in Structural Engineering* 21.11 (2018), pp. 1761–1773. DOI: 10.1177/1369433218754545. eprint: https://doi.org/10.1177/1369433218754545. URL: https://doi.org/10.1177/1369433218754545.

[32] Youshi Hong Xu Long Fei Ge. “Feasibility study on buoyancy-weight ratios of a submerged floating tunnel prototype subjected to hydrodynamic loads”. In: *Acta Mechanica Sinica* 31.5, 750 (2015), p. 750. DOI: 10.1007/s10409-015-0428-3. URL: http://ams.cstam.org.cn/EN/abstract/article_145610.shtml.

[33] Davide la Zara. “Dynamic Fluid-Structure-Vehicle-Interaction Analysis for Submerged Floating Tunnels”. In: (July 2019). URL: http://resolver.tudelft.nl/uuid:a61e65c2-eeee-496e-b8fa-7ffbd15f1f38.

[34] W. Zhang. “Global Dynamic Fluid-Structure-Interaction Analysis for a Submerged Floating Tunnel”. In: (2019), p. 1. URL: http://resolver.tudelft.nl/uuid:00c0b7b2-7dc3-47ed-9002-b2468787a8c0.

A

Eigenvalue problem singular tether

This appendix shows the procedure of the eigenvalue problem for the solitary tether described in chapter 4. The start with, the homogeneous and undamped equation of motion for the tensioned beam is required which is given below.

$$(\rho A + M_w)\frac{\partial^2 w}{\partial t^2} + EI\frac{\partial^4 w}{\partial x^4} - T\frac{\partial^2 w}{\partial x^2} = 0 \tag{A.1}$$

Now the displacement $w(x,t)$ is given as the motion of the structure relative to the ground. Next, a solution is assumed in the form of Eq.A.2.

$$w(x,t) = \Phi(x)Q(t) \tag{A.2}$$

Substituting this function will allow to separate the variables x and t for which the procedure is shown below. In here spatial derivatives are given with primes and time derivatives with dots;

$$(\rho A + M_w)\frac{\partial^2}{\partial t^2}\left(\Phi(x)Q(t)\right) + EI\frac{\partial^4}{\partial x^4}\left(\Phi(x)Q(t)\right) - T\frac{\partial^2}{\partial x^2}\left(\Phi(x)Q(t)\right) = 0 \tag{A.3}$$

$$\Phi(x)\left(\rho A + M_w\right)\ddot{Q}(t) + Q(t)EI\Phi''''(x) - Q(t)T\Phi''(x) = 0 \tag{A.4}$$

Dividing this by $(\rho A + M_w)\,\Phi(x)Q(t)$ gives:

$$\frac{\ddot{Q}(t)}{Q(t)} + \frac{EI}{(\rho A + M_w)}\frac{\Phi''''(x)}{\Phi(x)} - \frac{T}{(\rho A + M_w)}\frac{\Phi''(x)}{\Phi(x)} = 0 \tag{A.5}$$

Which only satisfies if:

$$\frac{EI}{(\rho A + M_w)}\frac{\Phi''''(x)}{\Phi(x)} - \frac{T}{(\rho A + M_w)}\frac{\Phi''(x)}{\Phi(x)} = -\frac{\ddot{Q}(t)}{Q(t)} = \omega^2 \tag{A.6}$$

From which the following two equations can be obtained:

$$EI\Phi''''(x) - T\Phi''(x) - \omega^2\left(\rho A + M_w\right)\Phi(x) = 0 \tag{A.7}$$

$$\ddot{Q}(t) + \omega^2 Q(t) = 0 \tag{A.8}$$

In the functions A.7 and A.8, space and time have been separated. In order to gain the eigenfrequencies and eigenmodes, the spatial function A.7 need to be solved. This will be done by the use of the boundary conditions as described in 4.2 but now in terms of $\Phi(x)$

$$x = 0 \qquad \Phi(0) = 0 \tag{A.9}$$
$$\Phi'(0) = 0 \tag{A.10}$$

$$x = L \qquad \Phi''(L) = 0 \tag{A.11}$$
$$\omega_t^2\Phi(L) + EI\Phi'''(L) + T\Phi'(L) - k_m\Phi(L) = 0 \tag{A.12}$$

With the spatial equation of motion (A.7) and the boundary conditions as above the eigenvalue problem is formulated. Next a solution for $\Phi(x)$ is assumed in the following form;

$$\Phi(x) = C1e^{i\lambda_1 x} + C2e^{-i\lambda_2 x} + C3e^{\lambda_3 x} + C4e^{-\lambda_4 x} \tag{A.13}$$

with:

$$\lambda_1 = \beta; \quad \lambda_2 = -\beta; \quad \lambda_3 = i\beta; \quad \lambda_4 = -i\beta \tag{A.14}$$
$$\beta = \frac{T + \sqrt{T^2 + 4EI(\rho A + M_w)\omega^2}}{2EI} \tag{A.15}$$

The assumed solution contains four constants which are still unknown. By substituting the four boundary conditions in this solution gives a set of 4 algebraic equations. In matrix formulation this set reads as;

$$\begin{bmatrix} \text{coeff}(C1, BC1) & \text{coeff}(C2, BC1) & \text{coeff}(C3, BC1) & \text{coeff}(C4, BC1) \\ \text{coeff}(C1, BC2) & \text{coeff}(C2, BC2) & \text{coeff}(C3, BC2) & \text{coeff}(C4, BC2) \\ \text{coeff}(C1, BC3) & \text{coeff}(C2, BC3) & \text{coeff}(C3, BC3) & \text{coeff}(C4, BC3) \\ \text{coeff}(C1, BC4) & \text{coeff}(C2, BC4) & \text{coeff}(C3, BC4) & \text{coeff}(C4, BC4) \end{bmatrix} \begin{bmatrix} C1 \\ C2 \\ C3 \\ C4 \end{bmatrix} = \begin{bmatrix} 0 \\ 0 \\ 0 \\ 0 \end{bmatrix}$$

Where in the matrix coeff (C1,BC1) is what ever multiplier comes for $C1$ by substituting the solution for $\Phi(x)$ in the boundary conditions 1 (Eq.A.9). Now to solve for the eigenfrequencies the determinant of the matrix is taken. This gives a function depending on ω only. Solving this equation allows to find an infinite amount of eigenfrequencies. Subsequently, the eigenmodes or found be substituting the eigenfrequencies in the function of $\Phi(x)$.

This method has been executed by the use of Maple for which the script is shown on the next pages. By applying the values of each parameter as defined in chapter 3 The following first four eigenfrequencies were found

$$\omega_1 = 2.76 \text{ rad/s}$$
$$\omega_2 = 24.02 \text{ rad/s}$$
$$\omega_3 = 65.46 \text{ rad/s}$$
$$\omega_4 = 128.75 \text{ rad/s}$$

```
restart;
rho_c := 2500 : Aw := 513.7 : Ac := 167.78 : delta_l := 100 : number_tethers := 2 : E := 2·10^11 :
    i := Pi/64·(dia^4 − (dia − 2·th)^4) : dia := 0.75 : th := 0.1 : A := Pi·dia^2/4 − Pi/4·(dia − 2·th)^2 :
    rho := 7850 : l := 30 : EI := E·i : rho_w := 1000 :

km := 1414213 : Mass := 400000 : Tn := 39950000 : Cm := 2 : Cd := 1 : M := rho·A : Mw :=
    (Cm − 1)·Pi/4·rho_w·dia^2 : Cw := 0 : Ct := 0 :

EQM1 := diff(W(x), x$4) − Tn/EI·diff(W(x), x$2) − ω^2·(M + Mw)/EI·W(x) + I·omega·Cw/EI·W(x)
    = 0
```

$$EQM1 := \frac{d^4}{dx^4} W(x) - 0.01809370201 \frac{d^2}{dx^2} W(x) - 9.261004889 \times 10^{-7} \omega^2 W(x) = 0 \quad (1)$$

```
dsolve(EQM1) : W := evalf(subs(_C1 = C1, _C2 = C2, _C3 = C3, _C4 = C4, rhs(%)));
```

$$W := C1\, e^{-1.000000000 \times 10^{-6} \sqrt{9.046851005 \times 10^{9} - 5. \sqrt{3.704401956 \times 10^{16} \omega^2 + 3.273820524 \times 10^{18}}}\, x} \quad (2)$$
$$+ C2\, e^{1.000000000 \times 10^{-6} \sqrt{9.046851005 \times 10^{9} - 5. \sqrt{3.704401956 \times 10^{16} \omega^2 + 3.273820524 \times 10^{18}}}\, x}$$
$$+ C3\, e^{-1.000000000 \times 10^{-6} \sqrt{9.046851005 \times 10^{9} + 5. \sqrt{3.704401956 \times 10^{16} \omega^2 + 3.273820524 \times 10^{18}}}\, x}$$
$$+ C4\, e^{1.000000000 \times 10^{-6} \sqrt{9.046851005 \times 10^{9} + 5. \sqrt{3.704401956 \times 10^{16} \omega^2 + 3.273820524 \times 10^{18}}}\, x}$$

```
dW := -diff(W, x) : ddW := diff(W, x$2) : dddW := diff(W, x$3) :
dU := -diff(U, x) : ddU := diff(U, x$2) : dddU := diff(U, x$3) :
BC1 := simplify(subs(x = 0, W)) :
BC2 := simplify(subs(x = 0, dW)) :
BC3 := simplify(subs(x = l, ddW)) :
BC4 := simplify(subs(x = l, ω^2·Mass·W + EI·dddW + Tn·dW − km·W)) :


Mat := Matrix([
[coeff(BC1, C1), coeff(BC1, C2), coeff(BC1, C3), coeff(BC1, C4)],
[coeff(BC2, C1), coeff(BC2, C2), coeff(BC2, C3), coeff(BC2, C4)],
[coeff(BC3, C1), coeff(BC3, C2), coeff(BC3, C3), coeff(BC3, C4)],
[coeff(BC4, C1), coeff(BC4, C2), coeff(BC4, C3), coeff(BC4, C4)],
]) :
sol := solve({BC1, BC2, BC3}, {C1, C2, C3}) : assign(%) :
C4 := 1 :
with(linalg) :
Frequency_Equation := det(Mat) :
```

$plot(\mathrm{Im}(Frequency\_Equation), omega = 0..155, y = -0.0001..0.0001, axis[1] = [gridlines = [20, thickness = 1, subticks = false, color = grey]], title = \text{"Natural Frequencies"}, titlefont = [\text{"ROMAN"}, 15])$

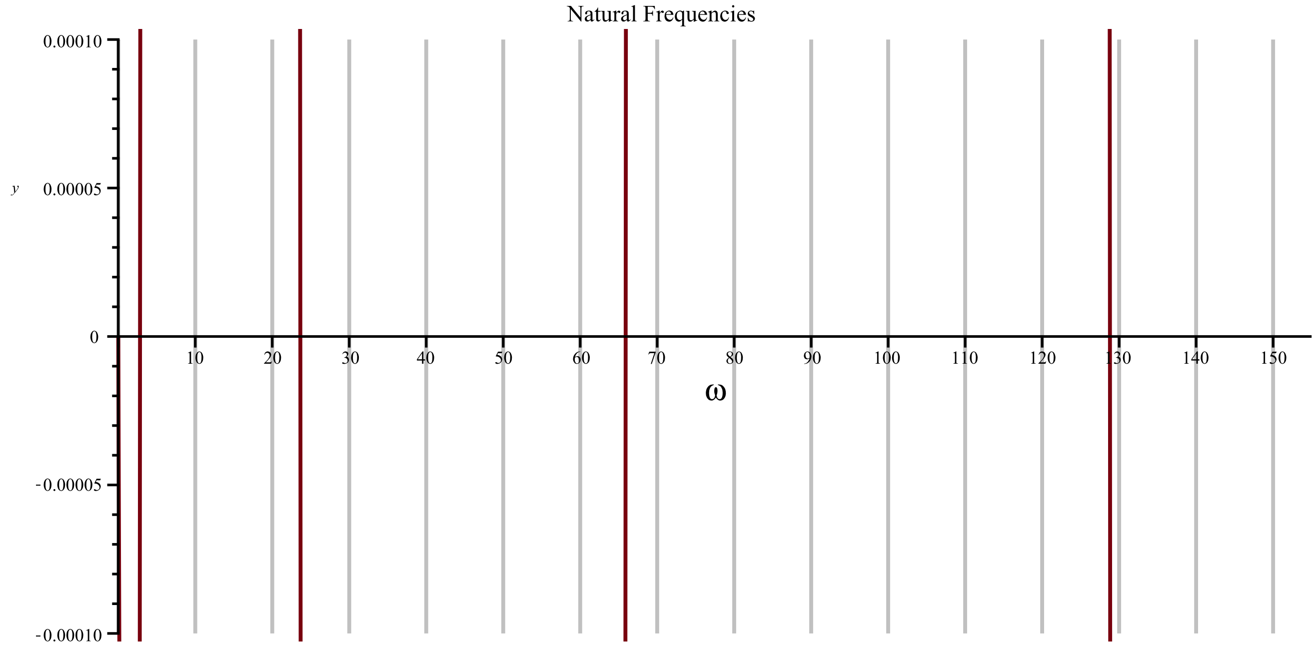

$\mathrm{omega}[1] := fsolve(\mathrm{Im}(Frequency\_Equation \cdot 10^{-110}), omega, 2..3); \mathrm{omega}[2] := fsolve(\mathrm{Im}(Frequency\_Equation \cdot 10^{-110}), omega, 20..35); \mathrm{omega}[3] := fsolve(\mathrm{Im}(Frequency\_Equation \cdot 10^{-110}), omega, 60..80); \mathrm{omega}[4] := fsolve(\mathrm{Im}(Frequency\_Equation \cdot 10^{-110}), omega, 120..140);$

$$\omega_1 := 2.764889637$$

$$\omega_2 := 24.01901838$$

$$\omega_3 := 65.46081361$$

$$\omega_4 := 128.7526601 \qquad (3)$$

for n **from** 1 **to** 4 **do** $Eigen\_period\_hertz[n] := \frac{\mathrm{omega}[n]}{2 \cdot \mathrm{Pi}}$ **end do**

$$Eigen\_period\_hertz_1 := 0.4400458528$$

$$Eigen\_period\_hertz_2 := 3.822745503$$

$$Eigen\_period\_hertz_3 := 10.41841206$$

$$Eigen\_period\_hertz_4 := 20.49162229 \qquad (4)$$

for n **from** 1 **to** 4 **do** $\Phi[n] := subs(\mathrm{omega} = omega[n], W)$ **end do**:

for n **from** 1 **to** 4 **do** $dphi[n] := diff(\Phi[n], x) : ddphi[n] := diff(\Phi[n], x\$2) : dddphi[n] := diff(\Phi[n], x\$3) : ddddphi[n] := diff(\Phi[n], x\$4)$ **end do**:

$\boldsymbol{p}[1] := plot(\mathrm{Re}(\Phi[1]), x = 0..l) : \boldsymbol{p}[2] := plot(\mathrm{Re}(\Phi[2]), x = 0..l) : \boldsymbol{p}[3] := plot(\mathrm{Re}(\Phi[3]), x$

$= 0\,..l)\,:\boldsymbol{p}[4] := plot(\mathrm{Re}(\Phi[4]), x = 0\,..l)\,:$
$plots[display](array([p[1], p[2], p[3], p[4]]))$

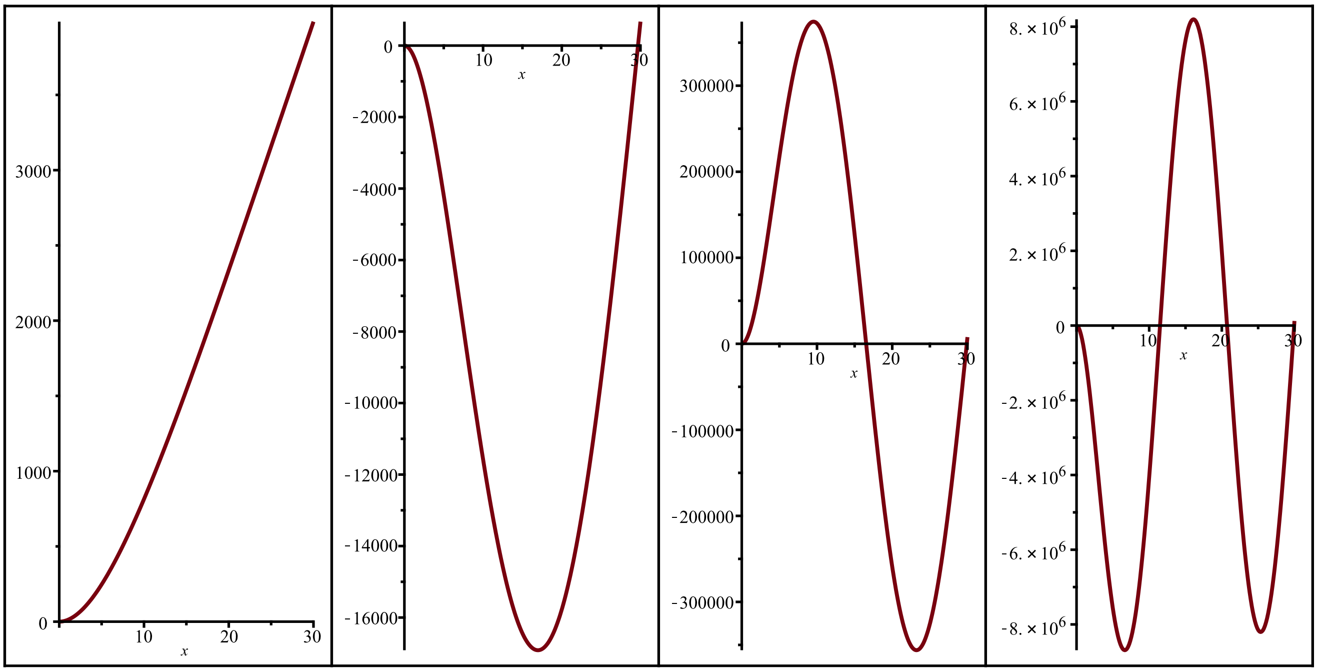

B
Frequency domain method of analysis singular tether

$restart:$

$Aw := 513.7 : delta\_l := 100 : number\_tethers := 2 : E := 2 \cdot 10^{11} : i := \frac{\mathrm{Pi}}{64} \cdot \left(dia^4 - (dia - 2 \cdot th)^4\right) :$

$dia := 0.75 : th := 0.1 : A := \frac{\mathrm{Pi} \cdot dia^2}{4} - \frac{\mathrm{Pi}}{4} \cdot (dia - 2 \cdot th)^2 : \mathrm{rho} := 7850 : L := 30 : EI := E \cdot i :$

$rho\_w := 1000 :$

$km := 1414213 : Mass := 400000 : Tn := 39950000 : Cm := 2 : Cd := 1 : M := \mathrm{rho} \cdot A : Mw := \frac{(Cm - 1) \cdot \mathrm{Pi}}{4} \cdot rho\_w \cdot dia^2 : Cw := 0.5 \cdot rho\_w \cdot dia \cdot Cd \cdot 0.09 : Ct := 0.5 \cdot rho\_w \cdot 17.50 \cdot Cd \cdot 0.09 :$

$Ug := piecewise\left(t > 1 \textbf{ and } t < 10, \frac{1}{100} \cdot \sin(10 \cdot t)\right);$

$$Ug := \begin{cases} \frac{\sin(10\,t)}{100} & 1 < t < 10 \\ 0 & otherwise \end{cases} \qquad \textbf{(1)}$$

$plot(Ug, t = 0 ..10, color = [blue]);$

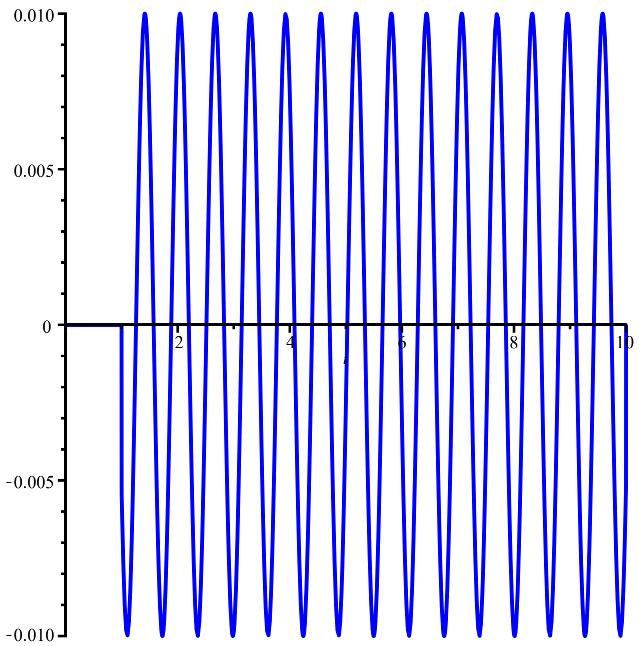

$with(inttrans):$

$Ug\_tilde := (int(Ug \cdot \exp(-I * \mathrm{omega} * t), t = -\mathrm{infinity} ..\mathrm{infinity}))$

$$Ug\_tilde := \frac{\mathrm{I}\, \mathrm{e}^{-10\,\mathrm{I}\,\omega}\, \omega \sin(100) - \mathrm{I}\, \mathrm{e}^{-\mathrm{I}\,\omega}\, \omega \sin(10) + 10\, \mathrm{e}^{-10\,\mathrm{I}\,\omega} \cos(100) - 10\, \mathrm{e}^{-\mathrm{I}\,\omega} \cos(10)}{100\left(\omega^2 - 100\right)} \qquad \textbf{(2)}$$

$plotA := plot(\mathrm{Re}(Ug\_tilde), \mathrm{omega} = 0 ..30, color = blue, legend = \text{"real"}) :$
$plotB := plot(\mathrm{Im}(Ug\_tilde), \mathrm{omega} = 0 ..30, color = red, legend = \text{"Img"}) :$
$plots[display]([plotA, plotB])$

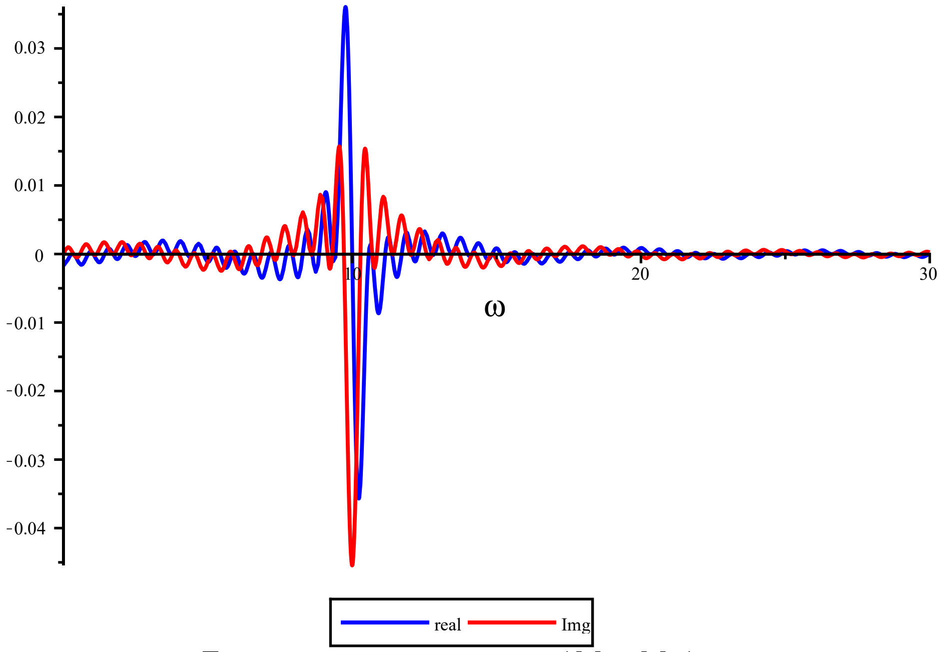

$$\#EQM1 := diff(W(x), x\$4) - \frac{Tn}{EI} \cdot diff(W(x), x\$2) - \omega^2 \cdot \frac{(M+Mw)}{EI} \cdot W(x) + I \cdot \mathrm{omega} \cdot \frac{Cw}{EI} \cdot W(x) = 0$$

$$EQM1 := diff(W(x), x\$4) - \frac{Tn}{EI} \cdot diff(W(x), x\$2) - \omega^2 \cdot \frac{(M+Mw)}{EI} \cdot W(x) = 0$$

$$EQM1 := \frac{d^4}{dx^4} W(x) - 0.01809370201 \frac{d^2}{dx^2} W(x) - 9.261004889 \times 10^{-7} \omega^2 W(x) = 0 \quad (3)$$

$dsolve(EQM1) : W\_tilde := evalf(subs(\_C1 = C1, \_C2 = C2, \_C3 = C3, \_C4 = C4, rhs(\%)));$
$dW\_tilde := diff(W\_tilde, x) : ddW\_tilde := diff(W\_tilde, x\$2) : dddW\_tilde := diff(W\_tilde, x\$3) :$

$$W\_tilde := C1\, e^{-1.000000000 \times 10^{-6} \sqrt{9.046851005 \times 10^{9} - 5. \sqrt{3.704401956 \times 10^{16} \omega^2 + 3.273820524 \times 10^{18}}}\, x} \quad (4)$$
$$+ C2\, e^{1.000000000 \times 10^{-6} \sqrt{9.046851005 \times 10^{9} - 5. \sqrt{3.704401956 \times 10^{16} \omega^2 + 3.273820524 \times 10^{18}}}\, x}$$
$$+ C3\, e^{-1.000000000 \times 10^{-6} \sqrt{9.046851005 \times 10^{9} + 5. \sqrt{3.704401956 \times 10^{16} \omega^2 + 3.273820524 \times 10^{18}}}\, x}$$
$$+ C4\, e^{1.000000000 \times 10^{-6} \sqrt{9.046851005 \times 10^{9} + 5. \sqrt{3.704401956 \times 10^{16} \omega^2 + 3.273820524 \times 10^{18}}}\, x}$$

$BC1 := simplify(subs(x = 0, W\_tilde - Ug\_tilde)) :$
$BC2 := simplify(subs(x = 0, dW\_tilde)) :$
$BC3 := simplify(subs(x = L, ddW\_tilde)) :$
$BC4 := simplify\left(subs\left(x = L, \omega^2 \cdot Mass \cdot W\_tilde + EI \cdot dddW\_tilde - Tn \cdot dW\_tilde - km \cdot W\_tilde - Ct \cdot I \cdot omega \cdot W\_tilde\right)\right) :$

$sol := solve(\{BC1, BC2, BC3, BC4\}, \{C1, C2, C3, C4\}) : assign(\%) :$

$plotA := plot(\mathrm{Re}(subs(x = L, W\_tilde)), \mathrm{omega} = 1..30, color = blue, legend = \text{"real"})\ :$
$plotB := plot(\mathrm{Im}(subs(x = L, W\_tilde)), \mathrm{omega} = 1..30, color = red, legend = \text{"Img"})\ :$
$plots[display]([plotA, plotB])$

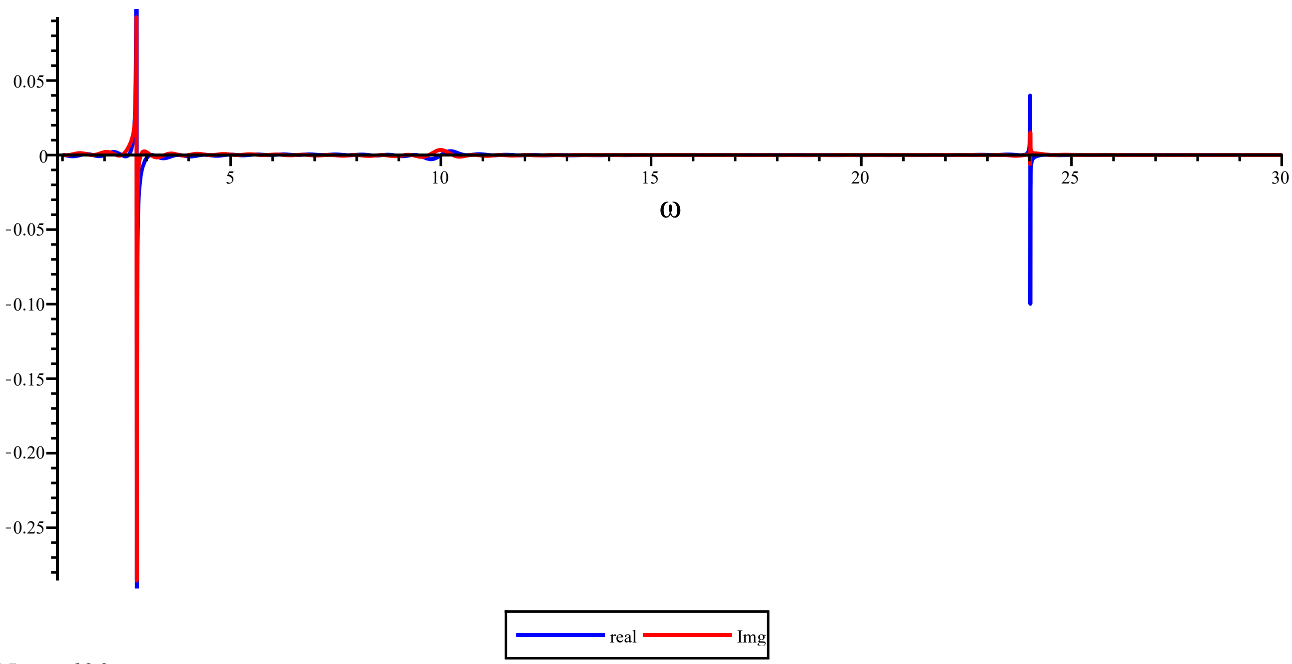

$N := 600 :$
$omegan := 30 :$

$$W\_t := \frac{N}{2\cdot 3.1415\cdot omegan}\cdot sum\left(subs\left(\mathrm{omega} = \frac{num\cdot omegan}{N}, W\_tilde\cdot \exp\left(I\cdot t \cdot\left(\frac{num\cdot omegan}{N}\right)\right)\right), num = 0..N-1\right) :$$

$W\_t\_top := \mathrm{Re}(subs(x = L, W\_t)) : M\_t\_bot := \mathrm{Re}(subs(x = 0, diff(W\_t, x\$2)\cdot -EI)) : V\_t\_bot := \mathrm{Re}(subs(x = 0, diff(W\_t, x\$3)\cdot -EI)) :$

$plot(\mathrm{Re}(W\_t\_top), t = 0..40, labels = [\text{"t/sec"}, \text{"m"}], title = typeset(\text{"Displacement top"}), titlefont = [\text{"ROMAN"}, 15])$

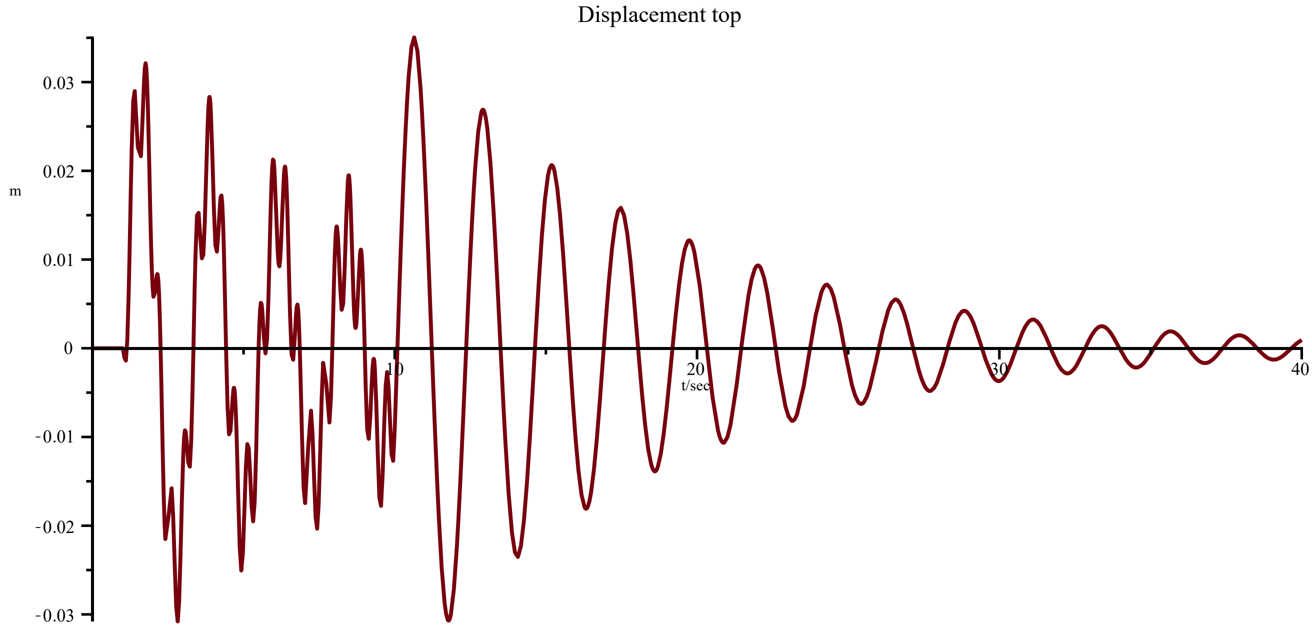

$plot(\mathrm{Re}(M\_t\_bot), t = 0..40, labels = [\text{"t/sec"}, \text{"Nm"}], title = typeset(\text{"Bending Moment bed"}), titlefont = [\text{"ROMAN"}, 15])$

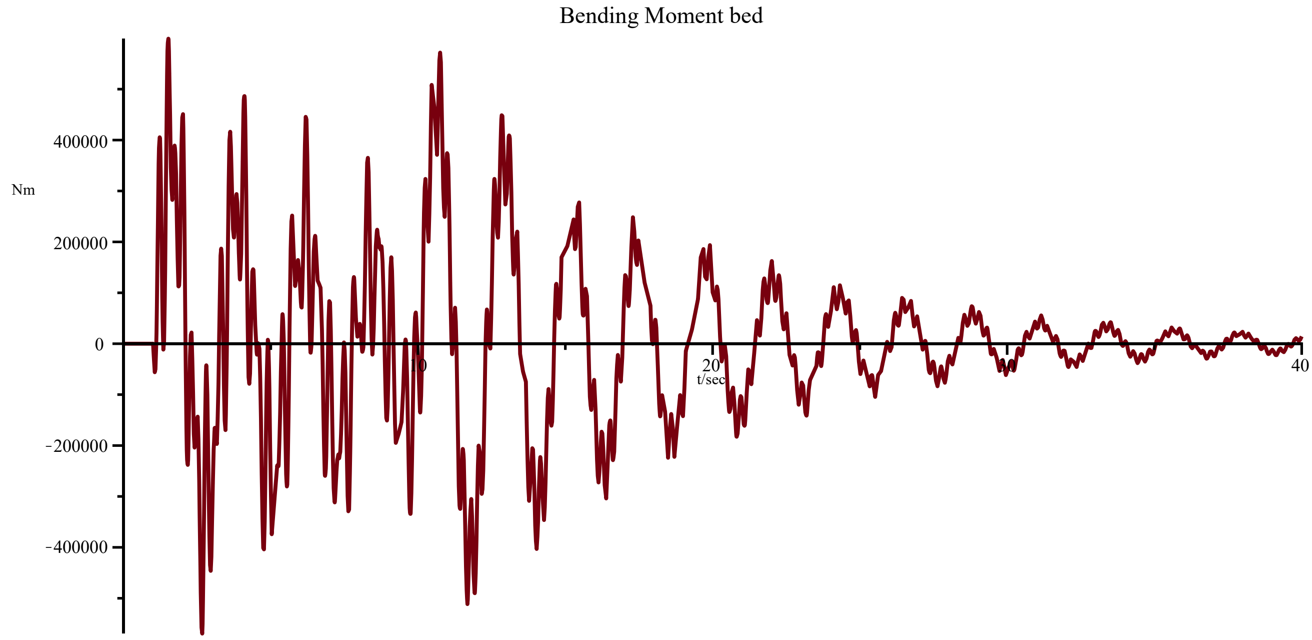

$plot(\mathrm{Re}(\ V\_t\_bot\ ), t = 0..40, labels = [\text{"t/sec"}, \text{"N"}], title = typeset(\text{"Shear Force bed"}), titlefont = [\text{"ROMAN"}, 15])$

Shear Force bed

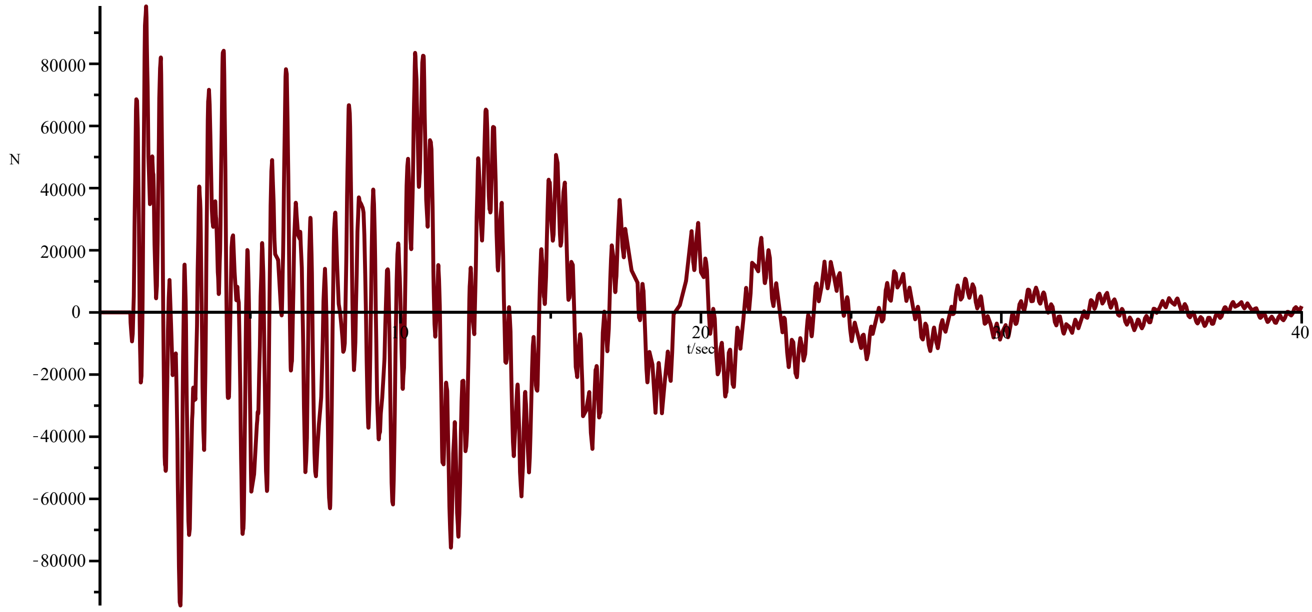

C

Sensitivity Test - Damping coefficients

Most of the parameters defined in this study are completely deterministic. Whereas for parameters such as material properties, this seems valid as these are mostly known, some parameters are less certain as the mechanisms behind these are complex and/or simplification were applied to make the calculations more feasible.

The damping due to the hydrodynamic forcing is one of these uncertain parameters. This damping was derived from the Morison Equation in where already an estimation was made in the form of the coefficients C_M and C_D. Next, a linearization was applied to make the expression applicable for the analysis. As this linearization was based on a stochastic process, again some uncertainties are involved. All this makes it likely that the values for the damping applied in this study may not correspond completely with reality. For that reason, a sensitivity test will be performed to analyze how different input values for this damping affect the results of the analysis.

For this test, only the damping for irregular waves will be analyzed as this was the damping applied for the total tunnel study. Eq.C.1 gives the expression for this damping as it was previously defined in Eq.2.9 in chapter 2.

$$C = \frac{1}{2}\rho_w D C_D \left(\sqrt{\frac{8}{\pi}}\sigma_v\right) \tag{C.1}$$

The highest uncertainly is in the parameter σ_v, which is defined as the standard deviation of the velocity of the input signal, as this is the term used to linearize the drag component. To test the sensitivity of this parameter, multiple analyses of the total tunnel will be performed in where for each analysis a different value of σ_v is applied. The values of σ_v for the different input signals used previously in the study lay in the range of $0.3 - 0.5$. To cover a slightly larger range, the analyses will be performed with the values $0.2, 0.3, 0.4, 0.5, 0.6$ for σ_v. To perform the time-history analysis, the scaled El Centro input signal is used. Figure C.1 shows the resulting displacements of the tunnel element with the different values for the standard deviation.

The figure shows that for larger values of σ_v, lower displacements are found which is as expected since larger values for σ_v directly result in larger damping values. Table C.1 shows the percentile differences of the maximum obtained displacements for two different values for σ_v. It shows that an increase of 0.1 for the standard deviations results in an $6\% - 7\%$ difference in maximum displacement. An increase for σ_v of 0.4 gives a decrease of 30% for the maximum displacement. Hence, it seems that the input value for this parameter σ_v does have a significant effect on the results of the analysis. Whereas an uncertainly for this value in the range of 0.1 may still result in reliable outcomes, any larger

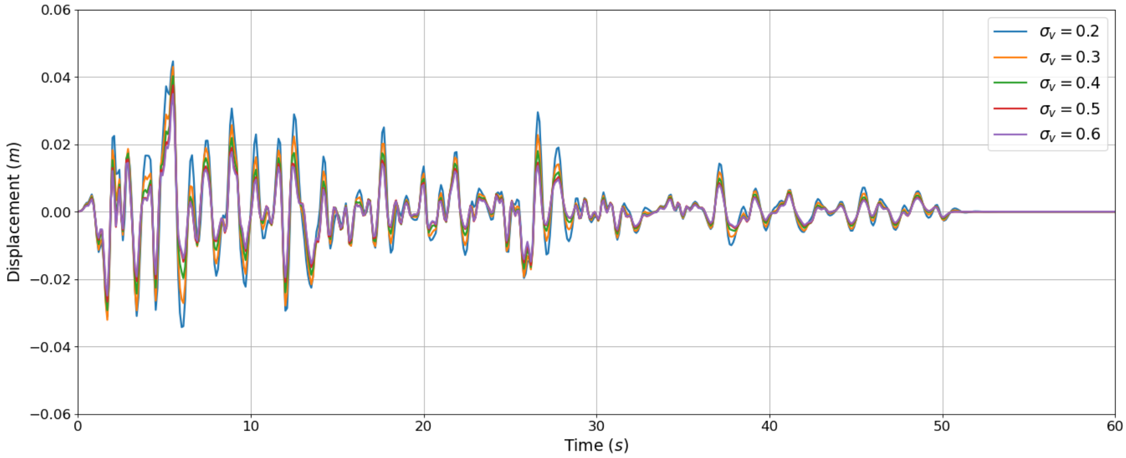

Figure C.1: resulting displacement for different values σ_v

uncertainties rapidly result in outcomes differing too much. So to obtain reliable outcomes, one should keep the uncertainty for the standard deviation of the input signal at a maximum of 0.1.

Table C.1: Percentile differences per increasing σ_v

Increase of $\sigma_\mathbf{v}$	**0.2 $\rightarrow$ 0.3**	**0.3 $\rightarrow$ 0.4**	**0.4 $\rightarrow$ 0.5**	**0.5 $\rightarrow$ 0.6**	**0.2 $\rightarrow$ 0.6**
Percentile difference displacement	-5.92%	-6.88%	-7.26%	-7.26%	-30.25%